MOLECULAR ELECTRONIC CONTROL OVER TUNNELING CHARGE TRANSFER PLASMONS MODES

TAN SHU FEN

(B. Appl. Sc. in Applied Chemistry (Hons.), NUS)

A THESIS SUBMITTED

FOR THE DEGREE OF DOCTOR OF PHILOSOPHY

DEPARTMENT OF CHEMISTRY
NATIONAL UNIVERSITY OF SINGAPORE

2015

Thesis Declaration

I hereby declare that this thesis is my original work and it has been written by me in its entirety, under the supervision of Assistant Professor Christian A. Nijhuis, Department of Chemistry, National University of Singapore. I have duly acknowledged all the sources of information which have been used in the thesis.

This thesis has not been submitted for any degree in any university previously.

The content of the thesis has been partly published in:

Tan, S. F.; Wu, L.; Yang, J. K.W.; Bai, P.; Bosman, M.; Nijhuis, C. A. "Quantum Plasmon Resonances Controlled by Molecular Tunnel Junctions" *Science* **2014**, *343*, 1496.

Tan Shu Fen		17.02.2016
Name	Signature	Date

Acknowledgements

I would like to express my sincere appreciation to all the people who help and support me during the research and their contributions to the work presented here.

First of all, I would like to thank Assistant Professor Christian, A. Nijhuis, my supervisor who gave me the opportunity to join his group as a Ph.D. student. Thank you so much for his guidance, stimulation in research, and dedication throughout my entire graduate study. Without his support, this thesis would not have been possible. I would like to thank my co-supervisor Dr. Michel Bosman in A*STAR's Institute of Materials Research and Engineering, Singapore. I am very grateful for his support in electron microscopy and his constructive inputs in writing process.

This work would have not been completed without the help and collaboration of difference people. I would like to thank Dr. Wu Lin and Dr. Bai Ping from A*STAR's Institute of High Performance and Computing, Singapore, who have contributed in modeling and simulations. I would also like to thank Dr. Joel Yang from Singapore University of Technology and Design, Singapore, for his contribution in plasmonics electronics study. Also, I would like to offer special thanks to Asst. Prof. Utkur M. Mirsaidov from Department of Physics who offers me his time, all the advice and knowledge about *in-situ* liquids cells electron microscopy. Thank you See Wee, Guanhua, and Zainul for their contribution to this work in liquids cells electron microscopy study. Thanks all of you for the time you have invested for your help, and guidance in Cryo Electron Microscopy Centre.

I wish to express sincere appreciation to all my colleagues and friends, and I own many thanks to Jiang Li, Li Yuan, Wang Dandan, Gan Lu, Du Wei, Calvin Wong Pei Yu, Harshini Venkata Annadata, for being such good colleagues and friends over the years during the good and bad moments. Thank you for your help, willing to discuss all kind of issues, and making such a nice atmosphere in a lab.

Finally, I wish to thank my family and friends in Malaysia and Singapore. Without their encouragement and support, I would not have made it this far.

Table of Contents

Summary

This thesis describes the controlled immobilization of molecules between two cuboidal metal nanoparticles by self-assembly method to control the over the quantum plasmon resonances. Unlike top-down nanofabrication, the molecules between the closely-spaced metal nanoparticles could control the gap sizes down to sub-nanometer scales and act as the frequency controllers in the terahertz regime, providing a new control parameter in the fabrication of electrical circuits facilitated by quantum plasmon tunneling.

The first part of the thesis (Chapters 3 to 5) describes on the fabrication of high aspect ratio, sub-nanometer gaps between two cuboidal metal nanostructures, their application in quantum plasmonics and the stability study of these nanostructures under the electron beam irradiation. We studied quantum mechanical effects of the metal-molecules-metal junctions by a combination of complimentary characterization techniques, e.g., electron microscopy, spectroscopy, and theoretically confirmed by quantum-corrected finite-element-model (FEM) simulations. The second part of the thesis (Chapters 6 to 7) deals with the real-time imaging of chemical reactions of cuboidal metal nanoparticles in solution.

Chapter 1 gives an introduction to this thesis and Chapter 2 provides a literature overview of the self-assembly of nanoparticles with sub-nanometer

separations for application in plasmonics and stability study of the metal nanoparticles.

Chapter 3 describes the fabrication of the high aspect ratio gaps between metal nanoparticles with different mixed self-assembled monolayers (SAMs) of thiolates and dithiolates. We study the metal-molecules-metal nanostructures with various characterization techniques (TEM, 3D STEM Tomography, XPS, UPS, UV/Vis spectroscopy). Chapter 4 demonstrates the realization of quantum plasmon tunneling by using the metal-molecules-metal junctions as a platform and electron microscopy as characterization techniques. We demonstrate how the molecules in the gaps control the gap sizes and the opto-electronic properties of the tunnel junctions, thereby providing a control over the tunneling charge transfer plasmon mode. In chapter 5, we give a stability study of the cuboidal metal nanoparticles under electron beam and discuss the strategies could be taken for avoiding radiation damage. The synthesis of high-quality cuboidal metal nanoparticles we use for quantum plasmonics requires deeper understanding of the reaction chemistry and kinetics at nanoscale. Chapters 6 and 7 describe the real-time visualization of chemical reactions of cuboidal metal nanoparticles in solution by using liquid-cell electron microscopy techniques.

The result presented in this thesis show that self-assembly in bottom-up nanofabrication is a promising strategy to obtain high aspect ratios gap between nanoparticles. Additionally, the molecules could act as the frequency controllers in terahertz regime, leading to the realization of molecular electronics at optical frequencies.

List of Tables

List of Figures

List of Abbreviations

AA	L-ascorbic acid
BDT	1,4-benzenedithiol
BDP	Bonding dipole plasmon
BPDT	1,4-biphenyldithiol
CPK	Corey-Pauling-Koltun model
CTAB	Cetyltrimethylammonium bromide
CTP	Charge transfer plasmon
DIET	Desorption-induced electronic transitions
EBID	Electron beam induced deposition
EBL	Electron beam lithography
EDT	1,2-ethanedithiol
EDTA	Ethylenediaminetetraacetic acid
EDX	Energy-dispersive X-ray spectroscopy
EELS	Electron energy-loss spectroscopy
EG	Ethylene glycol
FCC	Face-centered cubic
FEM	Finite-element-model
GLC	Graphene liquids cell
HAADF	High angle annular dark field
HDT	1,6-hexanedithiol
HRTEM	High resolution transmission electron microscopy
HOMO	Highest occupied molecular orbital
LCEM	Liquid-cell electron microscopy
LUMO	Lowest unoccupied molecular orbital
LSPR	Localized surface plasmon
NDT	1,5-dimercaptonapthalene
NP	Nanoparticle
ODT	1,8-octanedithiol

OPV	4,4-dimercaptostilbene
PT	1-propanethiol
PVP	Poly (vinyl) pyrrolidone
QCM	Quantum-corrected model
SAMs	Self-assembled monolayers
SEM	Scanning electron microscopy
SERS	Surface-enhanced Raman spectroscopy
STEM	Scanning transmission electron microscopy
tCTP	Tunneling charge transfer plasmon
TEM	Transmission electron microscopy
THF	Tetrahydrofuran
TXM	Transmission X-ray microscopy
UPS	Ultraviolet photoelectron spectroscopy
UV-Vis	Ultraviolet-Visible light spectroscopy
XPS	X-ray photoelectron spectroscopy

List of Symbols

D_c	Critical electron dose
d_l	Molecular length
d_g	Gap size
E_res	Plasmon resonance energy
E_s	Sputtering threshold energy
E_d	Displacement threshold energy
E_0	Incident energy
E_HL	HOMO-LUMO energy gap
E_gap	Gap field
E_plasmon	Plasmon energy stored in capacitor
$\hbar$	Planck constant
G_0	Quantum conductance
J_0	Hypothetical current when tunneling width equals to 0
m	Mass of charge carrier
$V_{deposition}$	Atom deposition rate
$V_{diffusion}$	Surface diffusion rate
ε_r	Relative static permittivity (dielectric constant)
ε_0	Vacuum permittivity
σ	Electron scattering cross section
β	Tunneling decay coefficient
φ	Barrier height
α	Energy level alignment of molecular frontier orbitals with respect to the Fermi levels of Ag electrode
λ	Absorption peak

Chapter 1

General Introduction

1.1. Introduction

Light can be used as an information carrier and transmitted in fibre optic cables or in on-chip optical interconnects. Photonic circuit elements are large but they operate at frequencies close to 1 terahertz, several orders of magnitude higher than typical switching speeds in microchip transistors. As current state-of-the-art nano-electronic devices operate at length scales that are much smaller than the wavelength of visible or infrared light, the diffraction limit makes it very difficult to combine the ultra-fast properties of photonic elements with nano-scale electronics.

Metal nanostructures have drawn much attention in the research fields of physics and chemistry in the past decades due to their unique capability to interact with light so as to constitute surface plasmons, which are collective, ultra-fast oscillations of electrons at the metal-dielectric interface. Due to this high-frequency oscillatory nature of surface plasmons, they are seen as a potential candidate to bridge the gap between optics and electronics. By combining the small scale of microelectronics and the fast operating speed of optics, surface plasmons promise to hold the key to great improvements in device efficiency and speed.

Plasmonic behavior of metals can be described by classical physics based on Maxwell's equations. However, these descriptions ignore quantum effects and fail for plasmonic systems with confined dimensions or interparticle gaps smaller than 1 nm. In the latter case, quantum mechanical tunneling between plasmonic structures becomes non-negligible when two plasmonic resonators are placed so closely in space that the plasmon-induced fields induce significant numbers of electrons to tunnel across the gap.[1-11] Direct experimental access to the resulting tunneling charge transfer plasmon mode is expected to open up new opportunities in, for instance, nano-scale opto-electronics, single molecule sensing, and non-linear optics.[1]

Hints of such a quantum mechanical plasmon mode have been measured indirectly,[6, 10] and were theoretically shown to become important at length scales <0.3 nm, inaccessible by present-day nanofabrication techniques. Top-down nanofabrication techniques such as electron-beam lithography (EBL) and photolithography do not provide the accuracy to fabricate such small gaps between two metal nanostructures accurately and reproducibly.[12-14] Due to this lack of resolution in device fabrication, quantum-plasmon effects have been difficult to investigate experimentally.

Despite the lack of control over the device layout design, wet chemical synthesis techniques and self-assembly in bottom-up nanofabrication provide a promising alternative strategy to achieve such narrow, high aspect ratio gaps at a large scale. Moreover, the molecules between the closely-spaced metal particles may act as frequency controllers in the terahertz regime, providing a new control parameter in the fabrication of electrical circuits that may show quantum plasmon tunneling effects. One of the key practical issues in this approach is the controlled immobilization of the molecules linking two metal nanoparticles leading to well-characterized and stable nanostructures.

The research presented in this thesis focuses on the fabrication of high aspect ratio, sub-nanometer gaps between two cuboidal metal nanostructures and how these gaps are useful in quantum plasmonics. In Chapter 2, a literature overview is given on the self-assembly of nanoparticles with sub-nanometer separations for application in plasmonics. Of particular interest is the stability study of the metal nanostructures.

Chapter 3 deals with the formation of sub-nanometer gaps (metal/molecules/metal junctions) by functionalizing the cuboidal metal nanoparticle with different mixed self-assembled molecular monolayers (SAMs) of thiolates and dithiolates.

Chapter 4 demonstrates the application of such high aspect ratio gaps to realize quantum plasmon tunnelling. Using electron microscopy characterization techniques, we demonstrate how the molecules in the gap control the gap sizes and the electronics properties of the junctions, providing a way to control the tunnelling charge transfer plasmon mode.

In Chapter 5, we do a step back and give a more detailed stability study on the cuboidal metal nanoparticles under electron beam irradiation. This chapter discusses the sample degradation effects and the preventive approaches that could be taken against radiation damage during experiments involving high energy electron beams encountered in transmission electron microscopes (TEMs) for instance.

The synthesis of the high-quality cuboidal metal nanoparticles that we produce for quantum plasmonics is not trivial, and its success directly depends on the reaction chemistry and kinetics during synthesis. A key issue in the field of wet-synthetic nanoparticle synthesis is the real-time visualization of the chemical reaction to track the reaction kinetics and dynamics at nanoscale. The mechanisms of the formation of nanoparticles during chemical synthesis in solution have been widely studied using *ex-situ* methods. A popular method is to stop the reaction at various stages and image the intermediate reaction products by various techniques based on TEM. Chapters 6 and 7 describe the mechanisms of the galvanic replacement reaction between silver nanocubes and chloroauric acid, and the overgrowth of silver on gold nanocubes in aqueous medium, respectively, followed in real-time with *in-situ* TEM using liquid reaction-cells.

The last Chapter gives a summary and the conclusions, as well as an outlook to further extend the work presented in this thesis.

1.2. Reference

1. Tame, M. S.; McEnery, K. R.; Ozdemir, S. K.; Lee, J.; Maier, S. A.; Kim, M. S., Quantum plasmonics. *Nature Physics* **2013,** *9* (6), 329-340.
2. Brongersma, M. L.; Shalaev, V. M., The Case for Plasmonics. *Science* **2010,** *328* (5977), 440-441.
3. Romero, I.; Aizpurua, J.; Bryant, G. W.; García De Abajo, F. J., Plasmons in nearly touching metallic nanoparticles: singular response in the limit of touching dimers. *Optics Express* **2006,** *14* (21), 9988-9999.
4. Zuloaga, J.; Prodan, E.; Nordlander, P., Quantum Description of the Plasmon Resonances of a Nanoparticle Dimer. *Nano Letters* **2009,** *9* (2), 887-891.
5. Marinica, D. C.; Kazansky, A. K.; Nordlander, P.; Aizpurua, J.; Borisov, A. G., Quantum Plasmonics: Nonlinear Effects in the Field Enhancement of a Plasmonic Nanoparticle Dimer. *Nano Letters* **2012,** *12* (3), 1333-1339.

6. Savage, K. J.; Hawkeye, M. M.; Esteban, R.; Borisov, A. G.; Aizpurua, J.; Baumberg, J. J., Revealing the quantum regime in tunnelling plasmonics. *Nature* **2012,** *491* (7425), 574-577.

7. Song, P.; Nordlander, P.; Gao, S., Quantum mechanical study of the coupling of plasmon excitations to atomic-scale electron transport. *The Journal of Chemical Physics* **2011,** *134* (7), 074701.

8. Kern, J.; Großmann, S.; Tarakina, N. V.; Häckel, T.; Emmerling, M.; Kamp, M.; Huang, J.-S.; Biagioni, P.; Prangsma, J. C.; Hecht, B., Atomic-Scale Confinement of Resonant Optical Fields. *Nano Letters* **2012,** *12* (11), 5504-5509.

9. Esteban, R.; Borisov, A. G.; Nordlander, P.; Aizpurua, J., Bridging quantum and classical plasmonics with a quantum-corrected model. *Nature Communications* **2012,** *3*, 825.

10. Scholl, J. A.; García-Etxarri, A.; Koh, A. L.; Dionne, J. A., Observation of Quantum Tunneling between Two Plasmonic Nanoparticles. *Nano Letters* **2012,** *13* (2), 564-569.

11. Duan, H.; Fernández-Domínguez, A. I.; Bosman, M.; Maier, S. A.; Yang, J. K. W., Nanoplasmonics: Classical down to the Nanometer Scale. *Nano Letters* **2012,** *12* (3), 1683-1689.

12. Broers, A. N.; Molzen, W. W.; Cuomo, J. J.; Wittels, N. D., Electron‐beam fabrication of 80‐Å metal structures. *Applied Physics Letters* **1976,** *29* (9), 596-598.

13. Cord, B.; Yang, J.; Duan, H.; Joy, D. C.; Klingfus, J.; Berggren, K. K., Limiting factors in sub-10nm scanning-electron-beam lithography. *Journal of Vacuum Science & Technology B* **2009,** *27* (6), 2616-2621.

14. Ou, F. S.; Hu, M.; Naumov, I.; Kim, A.; Wu, W.; Bratkovsky, A. M.; Li, X.; Williams, R. S.; Li, Z., Hot-Spot Engineering in Polygonal Nanofinger Assemblies for Surface Enhanced Raman Spectroscopy. *Nano Letters* **2011,** *11* (6), 2538-2542.

Chapter 2

Plasmonic Properties, Stability and Chemical Reactivity of Metal Nanoparticles – A Literature Review

2.1. Introduction

Noble metal nanostructures are widely studied for applications in optics,[1] meta-materials,[2-3] superlenses,[4-6] photovoltaics,[7-9] plasmonics,[10] and sensing,[11] due to their ability to interact with light to constitute surface plasmons[12] which are collective electron oscillations at optical frequencies (Figure 2.1 a) that can be manipulated at dimensions far below the diffraction limit.[13] Their high oscillation frequencies can potentially enable high speed transport of information (>100 THz) to bypass the inherently limited operating speed of microelectronics. Another technological advantage is the potential to scale plasmonic resonators far below the diffraction limit, which provides a route to miniaturize photonic elements[14] (Figure 2.1 b), thereby improving the efficiency and speed of future electro-optical devices.

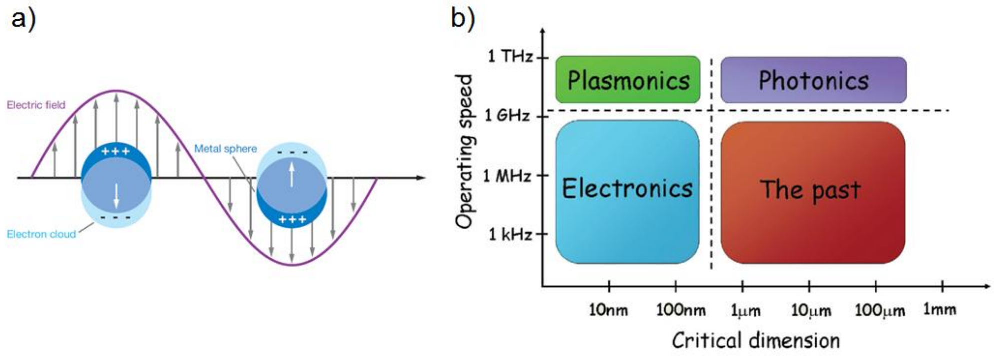

Figure 2.1 (a) Surface plasmons are charge oscillations in noble metal nanostructures.[12] (b) Operating speed and critical dimension of various chip-scale device technologies.[14] Figure (a) reprinted from ref. 12, with permission from Annual Reviews, Copyright 2007.

In this work, we aim to generate tunnel currents between plasmon resonators. This is challenging on an experimental level as discussed in Chapter 1, but also requires new simulation approaches that include quantum-mechanical effects beyond the commonly-used numerical methods that solve Maxwell's equations. In order to model the electron tunnelling, Esteban *et al.*[15] and Wu *et al.*[16] adopted a quantum-corrected model (QCM). The former shows that the observation of charge transfer plasmon mode (CTP) is expected only when the distance down to 0.3 nm[15] (indicated as by a red circle in Figure 2.2 a). Alternatively, an extremely high field (10^{10} V/m) is required to enable sufficient electrons to tunnel through a vacuum gap.[16] For this work, we collaborated with the latter group of Wu Lin and Bai Ping at IHPC (A*STAR) Singapore to support our experimental work with quantum-corrected simulations.

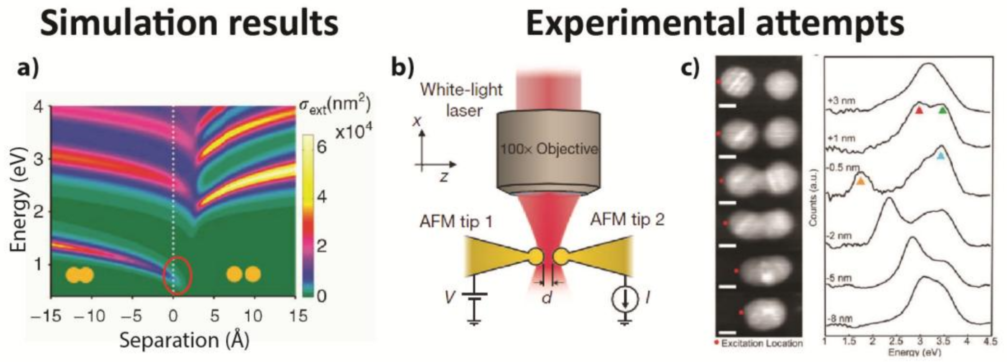

Figure 2.2 (a) Simulation result[15] and (b) (c) experimental attempts[17-18] for observing the charge transfer plasmon mode (tCTP). Figure (a) reprinted from ref. 14, with permission from Nature Publishing Group, Copyright 2012, (b) reprinted from ref. 17, with permission from Nature Publishing Group, Copyright 2012, and (c) reprinted from ref. 18, with permission from American Chemical Society, Copyright 2013.

After the theoretical predictions were published, a few experimental attempts[17-19] have been carried out to investigate the plasmon-induced electron tunnelling phenomena. However, overinterpretation of the results often leads to too strong claims. For instance, Savage *et al.*[17] has no correlated distance measurements as shown in Figure 2.2 (b) while Scholl *et al.*[18] did not investigate tunneling effect directly but indirectly in the form of a shift of the high-energy peak as shown by the red triangle in Figure 2.2 (c) which could also have causes unrelated to tunneling phenomena. For example, such a shift indicates the presence of electrostatic coupling, but it is not experimental evidence of tunneling. To prove the occurrence of tunneling, we need to observe the low-energy peak below 1 eV, while the resonators are not in contact with each other, according to theory: one needs to carry out optical measurements with spatial resolution far below the diffraction limit.

As mentioned in Chapter 1, the theoretically predicted small gaps (<0.3 nm) that are necessary for tunneling to occur are inaccessible by state-of-the-art nanofabrication techniques. However, self-assembled monolayers of molecules serve as a potential method to bring the two nanostructures to close proximity. In addition, from routine experimental tunnel junctions in molecular electronics, molecules with their own characteristic highest occupied molecular orbital-lowest unoccupied molecular orbital (HOMO-LUMO) gaps are known to participate in energy level tuning of the studied plasmonic system. To investigate the quantum tunneling effect at this length scales (<0.3 nm) and at these frequencies conclusively, atomic resolution imaging and single particle nano-optical spectroscopy is required, involving the utilization of transmission electron microscopy (TEM) and monochromated electron energy-loss spectroscopy (EELS). Thus, the stability of the nanostructures against electron beam damage becomes an important issue. In future, bimetallic or core-shell plasmon resonators may become important in the study of plasmon-induced tunneling, as they allow more flexibility in plasmon frequency-tuning. This thesis therefore also contains a section where galvanic replacement in solution is observed to form bimetallic and core-shell gold-silver nanoparticles.

To conduct this study, several questions must be answered: (i) How to precisely control the gap sizes between two nanostructures down to the quantum regime (<1 nm)? (ii) What is the role of the self-assembled monolayer of molecules and how to correlate the molecular properties to the charge transfer plasmon mode? (iii) How does the stability of the metal nanostructures impact on the quantum plasmonics study? (iv) How does the chemical composition of the metal nanostructures change in the presence of other metal ions? Therefore, well-defined chemical and structural plasmonic nanostructures are needed to study quantum plasmonics in practice.

Here, we review recent progress of noble metal nanostructures in engineering sub-nm separations, characterization techniques to study the charge transfer plasmon mode, stability of the nanoparticles against electron beam irradiation, and also their chemical reactivity with other metal ions in solution.

2.2. Engineering Sub-nm Gaps in Nanostructures for Applications in Plasmonics

A textbook system for study the quantum mechanical tunneling is a nanoparticle dimer with a small gap. Engineering sub-10 nm gaps in nanostructure dimers or larger assemblies of nanostructures have been readily achieved by top-down and bottom-up approaches. Here, we briefly review these two general approaches, and discuss the pros and cons for each approach.

2.2.1. Top-down Approach

Top-down fabrication techniques such as electron beam lithography (EBL) provide several advantages. (i) Tailorable metal patterns and arrays can be fabricated. For instance, particles of any geometries and sizes, can be arranged in any array including dimers, trimmers, oligomers, chains, etc. (ii) It gives high yield and reproducibility over other techniques. Mirkin *et al.*[20-29] introduced a new method which is called on-wire lithography (Figure 2.3 a).

This novel, high-throughput method is useful to synthesize one-dimensional arrays of metal nanostructures (Figure 2.3 b) that could control the separation between adjacent structures down to 1-2 nm. The drawbacks of EBL are: (i) it requires relatively complicated and expensive equipment, (ii) it can only generate metal patterns over small areas, iii) it is difficult to up-scale without running into time restraints, and iv) the metal patterns generated are polycrystalline, which can cause significant plasmon damping at grain boundaries.

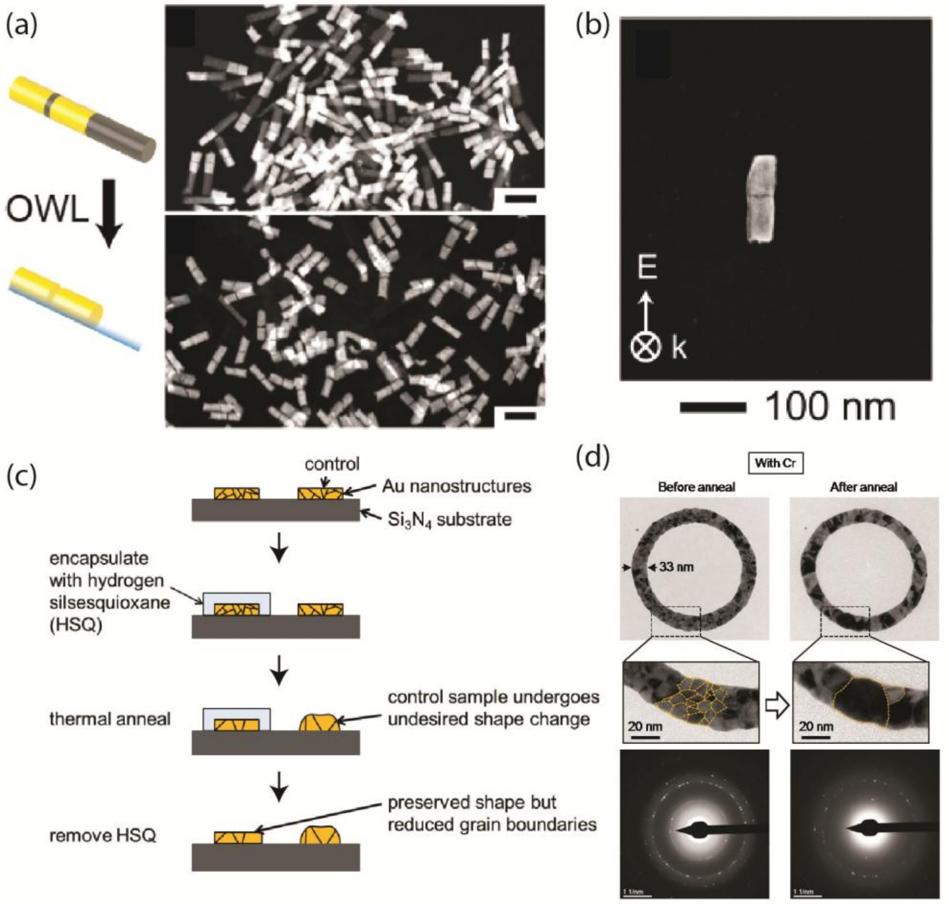

Figure 2.3 (a) On-wire lithography (OWL) introduced by Mirkin's group and (b) the resulting gold nanorods dimers.[20] (c) Encapsulating annealing method reported by Bosman *et al.* and (d) the TEM image and electron diffraction pattern of the same ring structure before and after annealing.[30] Figure (a) and (b) reprinted from ref. 20, with permission from American Chemical Society, Copyright 2012.

Moreover, surface roughness, adhesion layers and substrate effects have also been reported as causes of plasmon damping in EBL-fabricated samples. Bosman *et. al.*[30] reported a method of encapsulated annealing (Figure 2.3 c) that could preserve the shape of polycrystalline gold nanostructures, i.e. reducing the grain boundaries density (Figure 2.3 d) so as to reduce the plasmon damping in lithographically-defined structures. (v) It is unlikely to achieve routine sub-nanometer gap fabrication any time soon, which makes this top-down technique less useful for exploring plasmon-induced electron tunneling phenomena.[31-33]

2.2.2. Bottom-up Approach

On the other hand, aligning nanostructures with a small separation is relatively easily-achievable by wet-chemical solution processing methods. There are two common interactions used to assemble the nanoparticles. (i) Supramolecular assembly where molecules act as the linkers for guiding the nanoparticle assembly. This can be done via covalent forces[34-41] (Figure 2.4 a and b) such as metal-thiolate covalent bonding or non-covalent (Figure 2.4 c) interactions[42-44] such as Van der Waals interaction, electrostatic forces, etc. (ii) Solvent interactions[45-49] (Figure 2.4 d) where the assembly is driven by solvent-mediated interactions among hydrophobic ligands such as alkanethiols selectively bound to one side of the nanoparticles and hydrophilic surfactants such as cetyltrimethylammonium bromide (CTAB) on the other side of the nanoparticles.

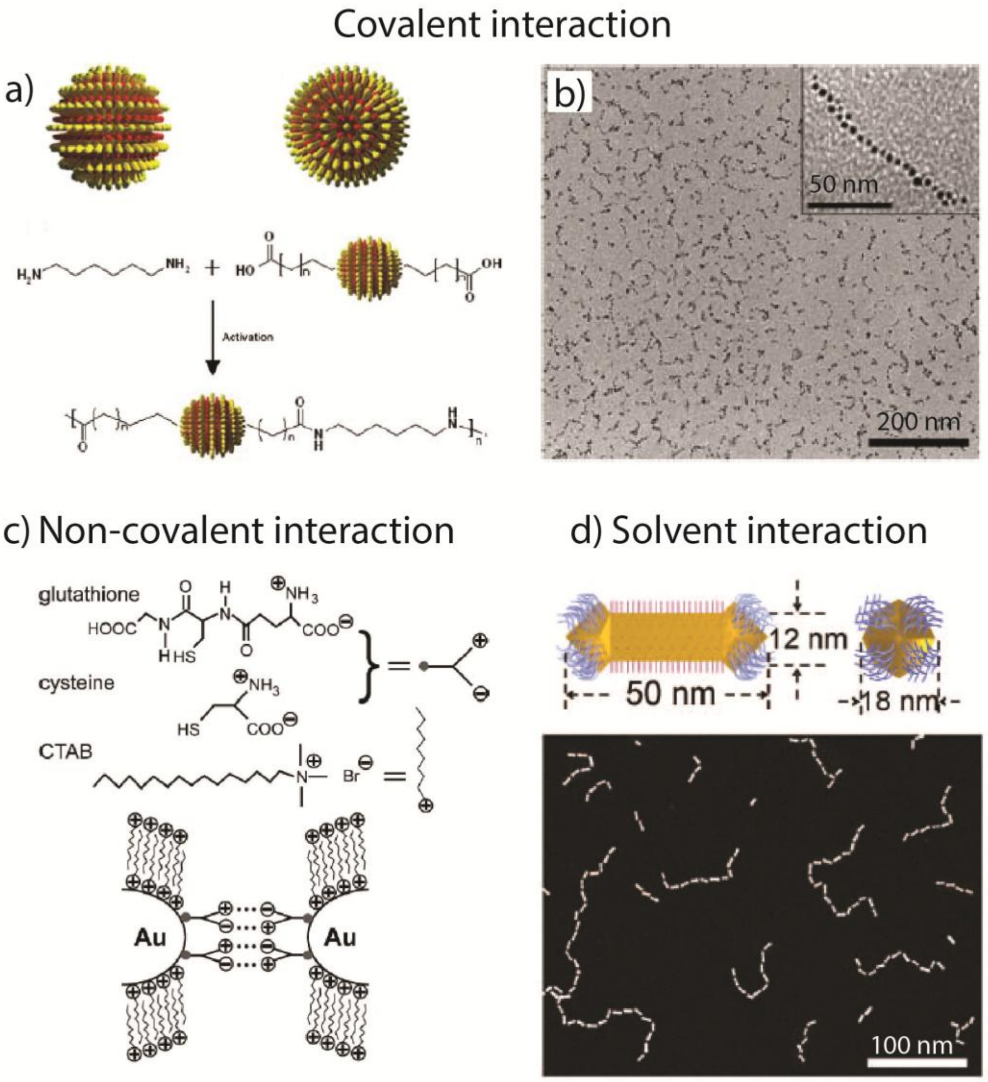

Figure 2.4 (a) Scheme and (b) TEM images of linear chain of Au nanocrystals formation through covalent interaction (amide bond).[41] (c) Schematic assembly mechanism using glutathione, cysteine and CTAB via non-covalent interaction (electrostatic forces).[44] (d) The growth of colloidal polymer chains where the nanorods carrying CTAB (hydrophilic) on the long side and thiol-terminated polystyrene (hydrophobic) molecules on the ends.[45] Figure (a) and (b) reprinted from ref. 41, with permission from The American Association for the Advancement of Science, Copyright 2007, (c) reprinted from ref. 44, with permission from Royal Society of Chemistry, Copyright 2007, (d) reprinted from ref. 45, with permission from The American Association for the Advancement of Science, Copyright 2010.

Wet-chemical or bottom-up approaches have been widely used for synthesizing silver nanoparticles of different sizes[50-51] and shapes[52-55] with high monodispersity. Chemically-synthesized nanoparticles are single-crystalline and experience less plasmon damping than those lithographically-defined nanostructures. In particular, the atomically smooth surfaces of silver nanocubes would enable the formation of high-quality interparticle gaps with distinct and flat interfaces. In addition, wet-chemical methods facilitate large-scale production of nanostructures without escalating time restrictions. Unlike top-down lithography, in wet-chemical synthesis, it is possible to control the inter-particle distance with the surface molecules.

However, large scale solution-phase method encounters reproducibility problems because of a lack of control over the assembly process, so the yield of—say—particle dimers is typically much lower for wet-chemical synthesis than for top-down methods.

2.3. Characterization Techniques for the Charge Transfer Plasmon Mode

A number of methods have been developed to characterize and study the plasmon-induced quantum tunneling phenomenon between closely-spaced metal nanostructures. The ultimate goal of plasmonics is to manipulate surface plasmons at the nanoscale, and complicated technologies have been used to characterize plasmons in detail. Here, we review the recent characterization techniques that have been in attempts to demonstrate quantum tunneling in plasmonics. Generally, they can be classified into two categories: (i) far-field spectroscopy (ii) near-field spectroscopy.

2.3.1. Far-field Optical Characterization

The most traditional and economic way to measure the plasmonic response of metal nanostructures is collecting the absorption or extinction spectrum by using the UV-Vis NIR spectrometer[53, 56]. Metal nanostructures exhibit a strong signal at their localized surface plasmon resonance frequencies. This can be done for nanostructures in suspension to examine the shapes, sizes, uniformity, etc. of the nanostructure morphologies. However, to study the quantum tunneling effect, dried nanostructures on well-dispersed substrates are much more practical study objects than nanoparticle suspensions. Thus, dark-field scattering microscopy coupled with UV-Vis spectrometry has been used. The scattering spectrum changes as a function of incident light polarization, wavelength, and dielectric environment.

Kern *et al.*[57] studied the white-light scattering spectra of side-by-side aligned nanorod dimers followed by the gap characterization in scanning electron microscopy (SEM). They reported that a peak at 800 meV corresponds to the symmetric and antisymmetric dimer modes due to the presence of atomically confined and resonantly enhanced optical fields in the gap. The energy splitting of each mode is a measure of coupling strength which depends on the gap width and refractive index of the material inside the gap. Without any means of controlling the gap width (simply drop-casting as shown in Figure 2.5 a and b), various geometries of the assembly products can be expected.

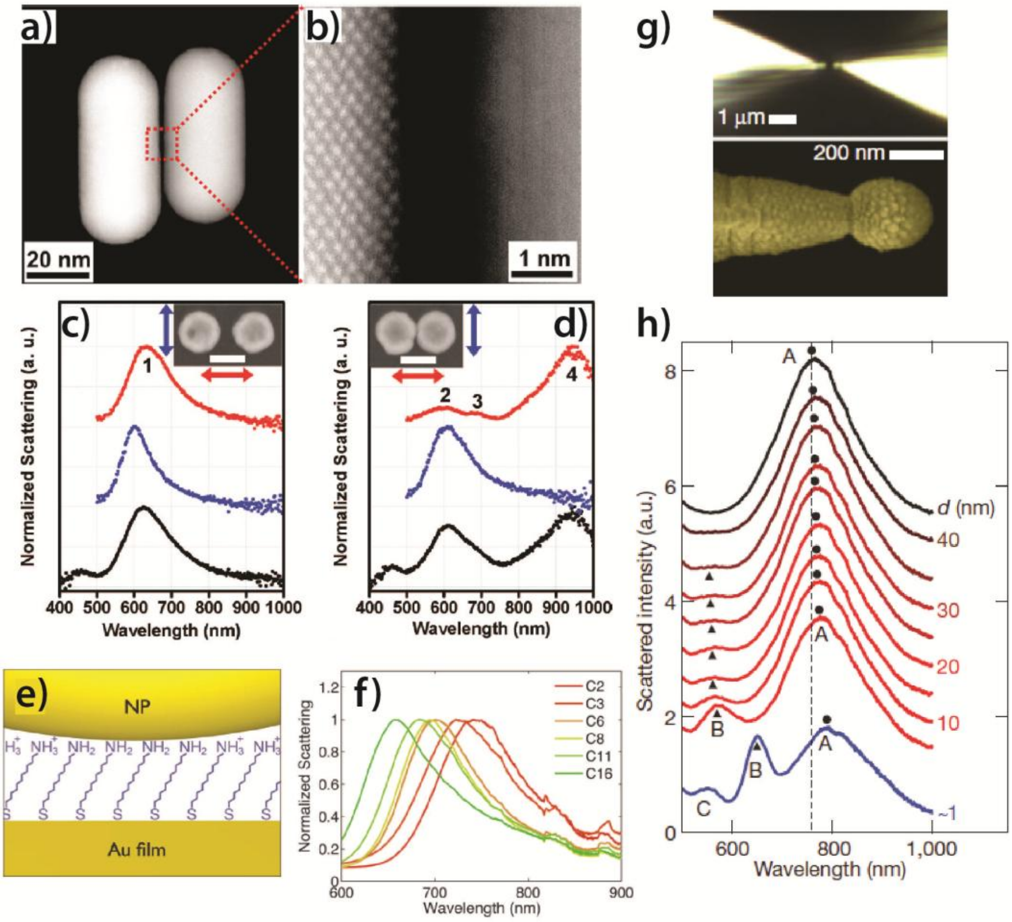

Figure 2.5 (a) STEM image and (b) zoom in gap region of a nanorod dimer.[57] Normalized scattering spectra of a nanoshell dimer (c) from non-touching to (d) touching region. (black spectra: unpolarised illumination; blue and red: polarization arrows of the same colours in the insets).[58] (e) Schematic of nanoparticle-film separated by an amine-terminated alkanethiolates SAM. (f) The corresponding normalized dark-field measured spectra for films with SAM spacer layers of different carbon numbers.[59] (g) Dark-field microscopy image of the gap consisted of two AFM-tips, SEM image of the ball-type tip and (h) measured scattering spectra at different distances between two tips.[17] Figure (a) and (b) reprinted from ref. 57, with permission from American Chemical Society, Copyright 2012, (c) and (d) reprinted from ref. 58, with permission from American Chemical Society, Copyright 2008, (e) and (f) reprinted from ref. 59, with permission from The American Association for the Advancement of Science, Copyright 2012, (g) and (h) reprinted from ref. 17, with permission from Nature Publishing Group, Copyright 2012,

Lassiter *et al.*[58] reported an optical study of 1,9-nonanedithiolates SAMs functionalized gold nanoshell dimers (Figure 2.5 c) and fused dimers (coined as “nanopeanuts” in Figure 2.5 d) with dark-field micro-spectroscopy. At close distances (1.0 - 1.5 nm), hybridized plasmon modes appear whose energies are extremely sensitively to the presence of a small number of molecules in the interparticle junction. When touching, a new plasmon mode arises from charge transfer via conduction, as the particles are in electrical contact and charge oscillates over the whole length of the fused double-particle system.

Yang *et al.*[60] studied the Rayleigh scattering spectra of silver nanospheres dimers with diameters of 41.0 ± 4.6 nm, self-assembled with a rational DNA programmed procedure to form gaps ranging from 1 to 25 nm. For larger gaps, the plasmon resonance energy (E_{res}) red-shifts continuously with decreasing center-to-center distance (L) until the L-to-diameter (D) ratio reaches a value of $L/D \approx 1.05$. For small gaps, E_{res} does not further red-shift; but the measured resonance energies become broadly distributed. Overall, they concluded that the spectral response of nearly touching dimers does not continue to intensify with decreasing gap sizes. This is not conclusive evidence for the occurrence of tunneling, as these gap sizes are still not considered small enough to observe significant quantum tunneling.

Ciracì and co-workers[59] demonstrated the use of SAMs of amine-terminated alkanethiolates to control the gap between the Au nanoparticle (NP) and gold film in order to study the field enhancements of this metal support surface plasmons (Figure 2.5 e). The optical scattering of the Au NPs spaced a few angstroms from a gold film is studied. The plasmon resonant scattering spectra for each sample, corresponds to different gap sizes as determined by the chain length of SAMs. Ellipsometry results further support the statement that the gap could be precisely controlled by the spacers of SAMs. When the NPs were brought closer to the film, coupling between NP and film induced a red-shift in the plasmon resonance wavelength (Figure 2.5 f). They compared the experimental results with a hydrodynamic theoretical model, and concluded that non-local effects are dominant where the electric permittivity of the spacer layer must be taken into account.

Savage *et al.*[17] also reported observing the quantum tunneling effect by placing two AFM tips at sub-nm distances (~0.3 nm) by piezoelectric actuation stages as shown in Figure 2.5 (g), followed by plasmon excitation with a laser, while the scattered light was collected and filtered to suppress background signal. They investigated three interaction regimes: capacitive near-field coupling (50 nm > d > 1 nm), the quantum regime (1 nm > d > 0 nm), and physical contact with conductive coupling (d < 0 nm). They found that when the separation between two nanostructures reduces below a critical size, the plasmon interactions enter the quantum regime, thereby showing a blue shift of the resonances (Figure 2.5 h). They attribute this observation to the screening of localized surface charges by quantum tunneling and a consequent reduction in plasmonic coupling. However, their imaging technique could not confirm the proposed gap sizes and therefore the conclusive evidence of plasmon-induced quantum tunneling remains incomplete.

2.3.2. Near-Field Spectroscopy of Plasmons

Near-field techniques such as scanning near-field optical spectroscopy (SNOM) can offer better spatial resolution than traditional optical microscopy. Unlike far-field techniques, SNOM scans the surface with a metal-coated optical probe that can detect evanescent waves, i.e., plasmons. However, the resolution is limited by the size of the probe that could offer the best resolution of ~20 nm. Other near-field techniques are provided by TEM-based spectroscopy, especially EELS and cathodoluminescence. The probe in these techniques is a converged beam of electrons, typically a nanometer or so in diameter, which can be placed with sub-nanometer accuracy at any location to excite surface plasmons. The advantage of all near-field techniques is the ease of probing single particles or single dimers, which is more difficult to achieve with far-field techniques that typically measure the response of large assemblies of nanostructures.

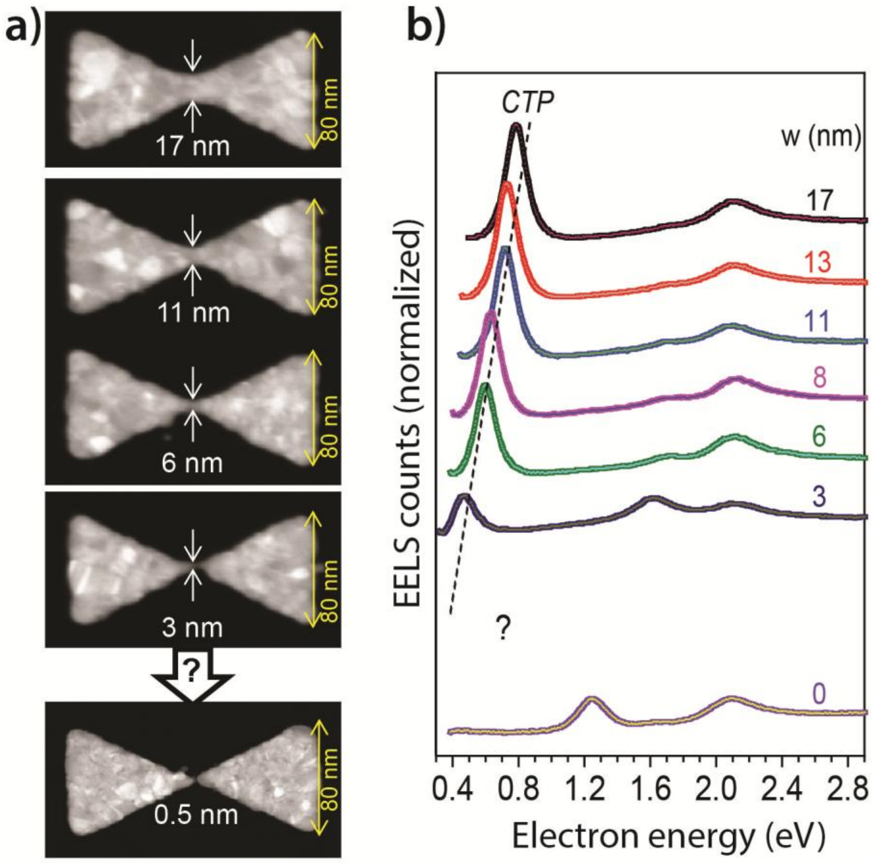

Figure 2.6 (a) STEM images and (b) corresponding EELS spectra of gold nanoprisms pairs with different bridge and gap sizes.[19] Figure (a) and (b) reprinted from ref. 19, with permission from American Chemical Society, Copyright 2012.

To conclusively study the gap sizes and the quantum tunneling effect, electron beam imaging and spectroscopy are a step forward, as they will provide much better resolution than photon-based probes. Besides the ability to perform local spectroscopy, it is also possible to perform direct sub-nanometer imaging at the same location. Using a scanning transmission electron microscope (STEM) and simultaneous EELS, Duan *et al.*[19] observed the gradual evolution of the bonding dipole plasmon (BDP) between pairs of nanoprisms separated by gaps down to 0.5 nm and also pairs connected by conductive bridges of >3 nm in width, as shown in Figure 2.6 (c) and (d).

Scholl *et al.*[18] reported the observation of unusual quantum phenomena for the BDP mode for silver nanosphere dimers from 3 nm separation to 8 nm wide bridges by using a STEM probe and simultaneous EELS measurements (Figure 2.2 c). For both studies, the tunneling cross sections (the surface areas that define the gap in the case of spheres and prisms) are not large enough, so the tunneling charge transfer plasmon mode still remains elusive, as manifested by the absence of the low-energy resonance (tunneling charge transfer mode) around 0.4-1.0 eV in these experiments for structures separated by a gap.

2.4. Stability of the Metal Nanoparticles against Electron Beam Irradiation

The characterization of nanoparticles often involves the utilization of TEM or SEM based techniques, but these techniques are based on high-energy electron beams which may cause (un)wanted changes to the specimen such as structural degradation, radiolysis of surface molecules, contamination build-up, electron-induced atomic displacements, or heating. Here, we review the mechanisms of electron beam-induced damage on functionalized metal nanoparticles and dimers.

2.4.1. Electron Beam-Induced Damage

Electron beam-induced damage comes in many forms, such as electron-nucleus scattering, which has been identified to produce electrostatic charging. Atomic displacement (“knock-on” effect) and electron beam sputtering of the TEM specimen are examples of such electron-nucleus interactions. On the other hand, inelastic scattering of the electron can cause specimen heating, ionization damage (radiolysis), hydrocarbon contamination, and electrostatic charging effect as well.[61]

1. Knock-on effect (Atomic displacement):

If the incident electron energy, E (in eV) exceeds some displacement energy, E_d (dependent on bond strength, crystal lattice and atomic weight of the constituent atoms), atomic nuclei can be displaced to interstitial positions and thereby degrade the crystalline order. This damage is predominant in conducting specimens such as metals. The degree of damage is dependent on the TEM accelerating voltage.[62] The E_d values are very much lower than the TEM accelerating voltages, so knock-on damage will always occur to certain degree.

Table 2.1 Displacement energy (E_d); and the corresponding threshold value of incident energy (E_0), for some common materials. Adapted from Hobbs *et al.*[63]

Materials	E_d (eV)	E_0 (keV)
Graphite	30	140
Diamond	80	330
Aluminium	17	180
Copper	20	420
Gold	34	1320

2. Electrostatic charging:

The net charge added to the specimen per second depends on backscattering coefficient and the yield for the emission of secondary electrons. The charge repulsion between the beam and the charged sample can cause a mechanical force[61] that the specimen is unable to withstand, e.g. tearing of polymer films, dislodging of particles, and sample vibrations.

3. Electron beam sputtering:

If high-angle scattering occurs at an atom which lies at the surface of a specimen, the energy, E_s required for displacement is relatively low; surface atoms do not have to be squeezed into an interstitial site, they are free to leave the specimen and enter the vacuum of the microscope. In addition, they are bound less tightly as the number of bonds to neighbouring atoms is low (i.e., low coordination number) at the surface. This is dependent on incident direction in a high angle collision and only happens at the beam-exit surface. Light and medium-Z atoms appear to be vulnerable to sputtering by 200 keV electrons.[61]

4. Electron beam heating:

Energy transferred during inelastic scattering can turn into X-rays, UV or visible radiation; it may also end up as heat within the specimen. Heat loss occurs through thermal conduction and radiation. It is found that the heating is independent of specimen thickness and also insensitive to beam diameter.[61] Li *et al.*[64] reported that the temperature rise in an organic specimen can reach a few hundred degrees for a stationary probe. However, the temperature could easily go down by a factor of ten if the beam is scanned at video rate.

5. Ionization Damage (Radiolysis):

Electron beam degradation occurs when the specimen undergoes loss of crystallinity or mass loss. This damage arises from the inelastic scattering of the incident electrons and is predominant for insulating specimens.[62] Examples of known beam-sensitive materials are alkali halides, oxides, and transition metal oxides. Chemical bonds of organic materials are broken, molecule changes in shape, shift in position and loss of crystallinity. This damage can be distinguished from knock-on damage in terms of incident energy, E and temperature dependence, T. The electron dose required to create damage, D_c for radiolysis increases with E and decreases with T while for knock-on effect, D_c decreases with E and varies little with T.[62]

6. Hydrocarbon Contamination:

This leads to mass gain as hydrocarbon molecules on the sample surface are polymerized by electrons, this polymer has low vapour pressure and surface mobility so thickness is increased during irradiation. Diffusion of hydrocarbons along the specimen surface is the main source of most hydrocarbon contamination. The specimen itself is the local source of hydrocarbons; to minimize this effect, organic residues on the samples should therefore be minimized. This can be done by plasma cleaning, heating to desorb hydrocarbons, cooling the specimen to reduce their mobility, or for samples made from particle suspensions by washing the suspension well.

Among the effects mentioned above, the knock-on damage and the ionization damage are critical for organic monolayer-coated inorganic nanoparticles. Knock-on effects usually occur in conducting inorganic specimen[62] where the accelerating voltage of the incident electron beam is higher than the displacement energy of the material or the electron dose exceeds about 1000 C cm^{-2}. On the other hand, the ionization damage is predominant for insulators such as organic monolayer molecules at all commonly used SEM and TEM beam energies (5-300 keV).

2.4.2. Sintering Mechanisms for Dimers or Clusters of Nanoparticles

When two nanoparticles are separated by a narrow gap of 1-2 nm, sintering is dominant when the nanoparticle atoms diffuse across the boundaries of the particles, fusing the particles together resulting in one solid piece. Chen *et al.*[65] reported two kinds of sintering mechanisms (Figure 2.7 a and b). (1) Ostwald ripening, where the metal atoms leave a metal particle, diffuse over the sample support and attach to another metal particle. (2) Surface diffusion, where the particles diffuse across the metal surface and collide with other particles, leading to the formation of neck like structures bridging adjacent particles, driven by the large surface tension resulting from the small particle size. Moreover, the sintering behaviour of bare metal particles is dependent on size while for passivated particles it is dependent on the stability of ligands to the electron beam. Larger passivated particles will have a larger electron scattering cross section (σ) which could enhance electron-material interaction, much more efficient for ligands removal, therefore lower dose is needed to produce sintering than small non-passivated particles.

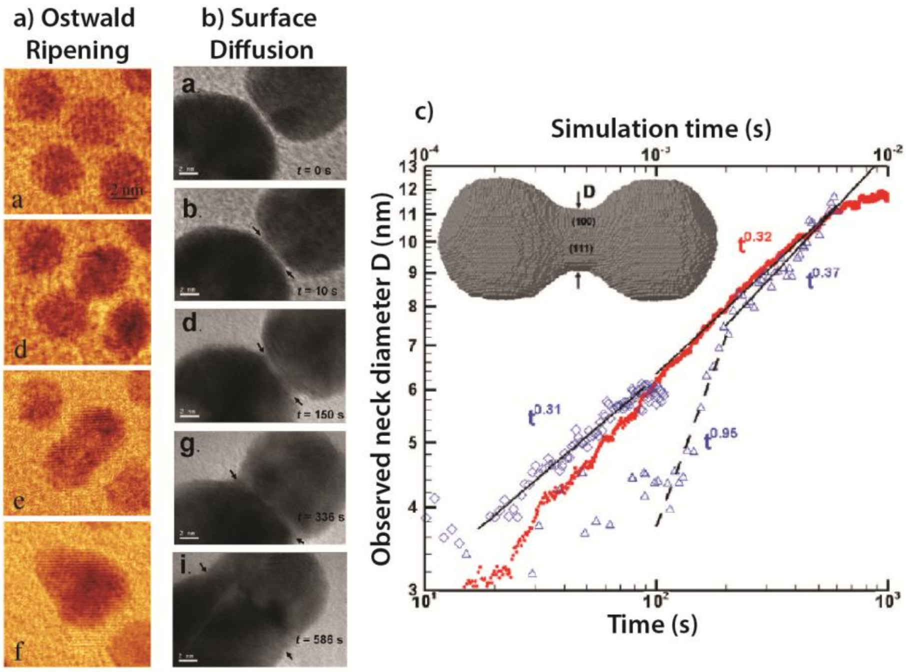

Figure 2.7 Two sintering processes: (a) Ostwald ripening[65] (b) Surface diffusion induced neck formation and (c) the evolution of size as a function of time.[66] Figure (a) reprinted from ref. 65, with permission from American Chemical Society, Copyright 2006, (b) and (c) reprinted from ref. 66, with permission from American Chemical Society, Copyright 2009.

In addition, surface diffusion between two metal nanoparticles with narrow gaps of 1-2 nm has also been reported.[18, 66-68] Flüeli and co-workers[68] reported that the intense incident electron beam (20 A cm^{-2} at 300 kV) would favour the coalescence of the particles. The presence of stacking faults and other structural defects in the newly formed crystal were first observed and subsequently a neck was formed between particles. The sintering process was further enhanced by the migration of surface atoms which partly took place via the carbon substrate. The initial relative orientation of the particles was also a determining factor for the rapid sintering process.

Lim *et al.*[66] reported a real-time TEM study of the coalescence of individual pairs of decahedral gold nanoparticles. They observed the rate of growth of the neck that joins two particles during coalescence and compare this to classical continuum theory and to atomistic kinetic Monte Carlo simulations as shown in Figure 2.7 (c). The authors attributed the disagreement between the observed results and classical continuum model to the faceted nature of the particles. Observations of spatially isolated pairs of nanoparticles have revealed a late-stage neck growth process with characteristic power law of $D \sim t^{0.31\text{-}0.37}$, which differs substantially from the relationship $D \sim t^{0.16}$ predicted by the classical continuum theory.

Surrey *et al.*[67] reported quantitative measurements of surface self-diffusion. They indicated that the observed motion is due to the diffusion of the gold atoms at steps and edges of the particle surface. Impressively, they recorded the whole self-diffusion process at the atomic scale using aberration-corrected high resolution transmission electron microscopy (HRTEM). They also estimated the diffusion coefficient by measuring the fluctuation of the atom column occupation at the surface of a gold nanoparticle. The estimated diffusion coefficient was found to be $D = 10^{-17}$ to 10^{-16} cm^2/s for both gold icosahedra and truncated octahedra.

Scholl *et al.*[18] demonstrated the use of the electron beam to induce motion of the particles along a substrate, following earlier work by Batson *et al.*[69], which allowed the controlled convergence and coalescence of particles. They attributed the cause of the movement to (1) the electron beam-facilitated surface diffusion of the nanoparticles’ atoms and (2) nanoparticle polarization due to the passing electron’s electric field. If the polarizations of the individual particles of a dimer become aligned, an attractive Coulombic force can be generated between them.

2.4.3. Strategies to Control Damage Caused by Electron Beam

To minimize the radiation damage caused by the electron beam, many strategies have been proposed. For instance, low-energy or low-dose imaging techniques,[70] specimen cooling with liquid nitrogen[71] or specimen coating[72-73] have been adopted to reduce the radiation damage. Specifically, ionization damage could be reduced by lowering the specimen temperature by reducing the atomic mobility[71, 74-75] while lowering the incident beam energy and electron dose could minimize the knock-on effect.[76-77]

In addition, specimen coating with carbon[72-73, 78] has also been demonstrated to show the protective effect where the coating acts as a diffusion barrier, reducing the escape rate for light gaseous elements. For inorganic materials, the coating not only reduces the rate of desorption-induced electronic transitions (DIET)[79] but also reduces the electrostatic charging effect.[72] Although this method is able to reduce the radiation damage, it also causes another problem of hydrocarbon contamination[61] where the hydrocarbon molecules on the specimen surface for a coating that gets thicker while irradiation proceeds. This makes the characterization of nanoparticles by the electron beam much more difficult as much of the transmitted electron signal is absorbed or elastically scattered.

2.5. Chemical Reactivity with Other Metal Ions in Solution

Real-time visualization of chemical reactions at the nanoscale is a key challenge in the field of wet synthetic nanoparticle synthesis. A popular method to investigate the reaction kinetics is to stop the reaction at various stages and image the intermediate reaction products by TEM. This approach yields detailed information about the structure of the (intermediate) reaction products, but early stages of the reaction, or fast reactions (on the order minutes or less), cannot be investigated. In addition, the effects of sample preparation—treating the suspension with other solvents followed by centrifugation and drop casting of a small volume of the reaction mixture on the TEM grid following by removal of the solvents and associated changes in the concentrations (and the reaction kinetics) during evaporation—are not known.

2.5.1. Introduction to Liquid Cells Electron Microscopy (LC-EM)

In-situ electron microscopy with liquid cells is an emerging technique for elucidating the mechanisms of nanostructure formation.[80-82] The first electrochemical LC as shown in Figure 2.8 (a) was introduced by Williamson *et al.*[83] in the year of 2003. However, the resolution was limited by the large total sample thickness (100 nm of each SiN membrane, 50 nm gold electrode and liquid thickness >1 µm), the best resolution achieved was 5 nm. Zheng *et al.*[81] pushed the membrane thickness to 25 nm (Figure 2.8 b) in the year of 2009 so as to study the Pt NP growth with sub-nm resolution in LC TEM.

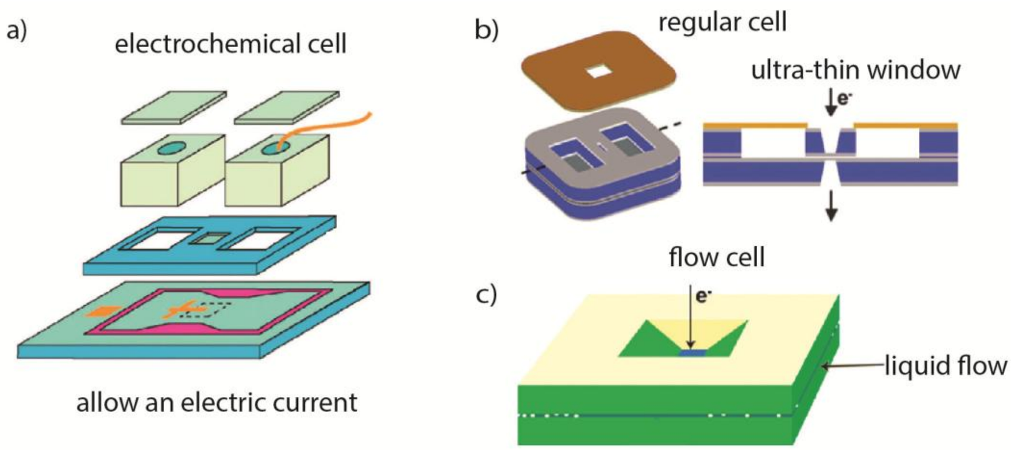

Figure 2.8 Schematic of an assembled liquid cell. (a) Electrochemical cell,[83] (b) regular cell[81] and (c) flow cell.[84] Figure (a) reprinted from ref. 83, with permission from Nature Publishing Group, Copyright 2003, (b) reprinted from ref. 81, with permission from The American Association for the Advancement of Science, Copyright 2009, (c) reprinted from ref. 84, with permission from PNAS, Copyright 2009.

In the same year, de Jonge *et al.*[84] described the use of the flow cell (Figure 2.8 c) to image whole biological cells in liquids with a constant flow of a buffer solution. This capability made it possible to study the reactions involving mixing of solvents or injecting reactants. Nonetheless, critical issues still need to be addressed, such as sample drift introduced by the liquid flow, membrane rupture, contamination, etc.

With the development of *in-situ* liquid cell electron microscopy and microfluidic devices, real-time high-resolution TEM/STEM imaging of processes in liquids was made possible. Many dynamic processes have been reported so far, such as the synthesis of colloidal nanoparticles of different shapes, e.g., nanospheres,[81, 85-86] nanocubes,[87] and nanorods[88] , electrochemical deposition,[83] self-assembly of nanoparticles,[89-90] biological processes,[84, 91] and nanoparticle dynamics[92]. Here, we summarize the recent progress in metal nanoparticles synthesis using liquids cells (LC) TEM.

1. Growth mechanisms

Zheng *et al*.[81] compared growth by nanoparticle coalescence with that by monomer attachment side-by-side within the same field of view (Figure 2.9 a). It is very interesting that two types of growth mechanisms reached the same particle size of the final product (Figure 2.9 b). It showed that the coalesced nanoparticle experienced recrystallization and shape re-arrangement, which prevented additional platinum atoms from attaching to the nanoparticle. So, a pause during growth was observed after a coalescence event, which allowed the nanoparticle by monomer attachment to catch up. Kraus *et al.*[93] reported that the dendritic nucleation was induced by the electron beam which led to an initial burst of growth as shown in Figure 2.9 (c). They studied the growth rate of the tip and concluded that the dendritic growth at this scale is limited by diffusion.

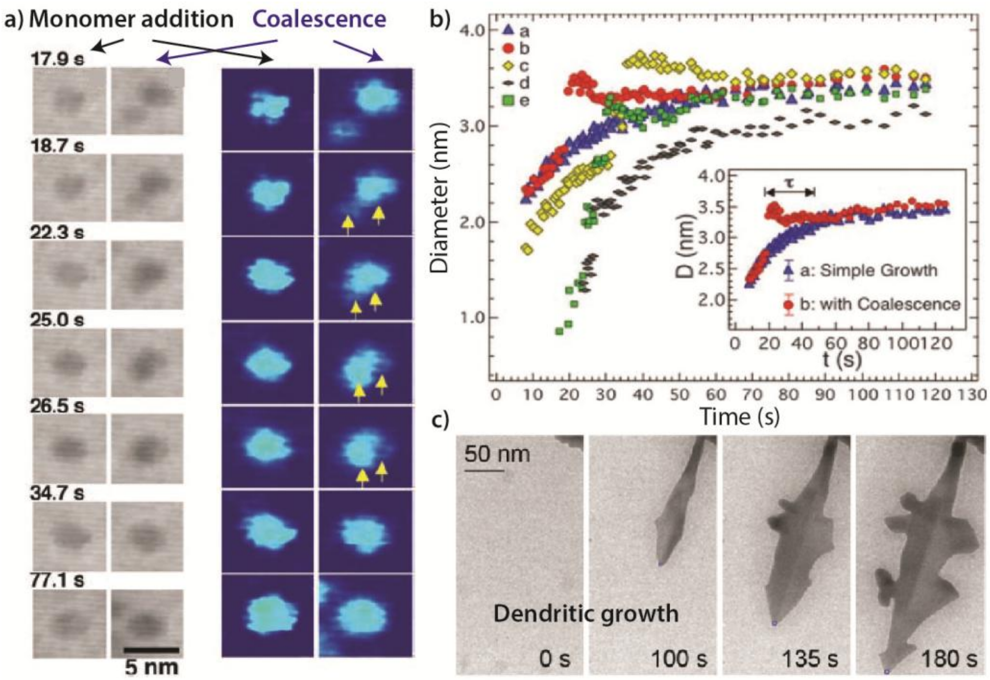

Figure 2.9 (a) Time-lapsed TEM images (left column) and false colour enlarged (1.5 times) images (right column) for Pt nanoparticles growth by means of monomer addition and coalescence. (b) Evolution of particle size as a function of time for two types of growth means.[81] (c) Time-lapsed TEM images indicating the growth of Au dendrites.[93] Figure (a) and (b) reprinted from ref. 81, with permission from The American Association for the Advancement of Science, Copyright 2009, (c) reprinted from ref. 93, with permission from American Chemical Society, Copyright 2013.

2. Shape control mechanisms and the role of surfactants

Many factors such as the concentration of the precursors, temperature, surfactants, etc. would affect the chemical potential of crystallization, thereby determining the final shape of the particles formed. Liao *et al.*[94] reported the role of the surfactant (oleylamine) on the shape evolution of platinum iron NPs (Figure 2.10 a). They claimed the prominence of the dipolar interactions between NPs where the NPs are stabilized without breaking down. They also attributed this to the steric hindrance effect. Jungjohann *et al.*[95] showed Pd growth in dilute Pd salt solution on Au seeds resulting in the formation of core-shell NPs as demonstrated in Figure 2.10 (b-g). They showed that the size and shape of the Au seeds determine the morphology of the Pd shells via preferential Pd incorporation in low-coordination sites and avoidance of extended facets. The growth was limited by the ion diffusion in the solution. Recently, Liao *et al*.[87] further reported the growth of platinum nanocubes in a liquid cell using TEM with high spatial and temporal resolution. Time-lapsed images are shown in Figure 2.10 (h). They studied the growth rate of all facets and found that for all low index facets the growth rates are similar until the {100} facets stop growing while the other facets continue to grow to finally lead to the formation of a nanocube. This study is supported by calculations which show that the much lower ligand mobility on the {100} facets is responsible for arresting the growth of the {100} facets.

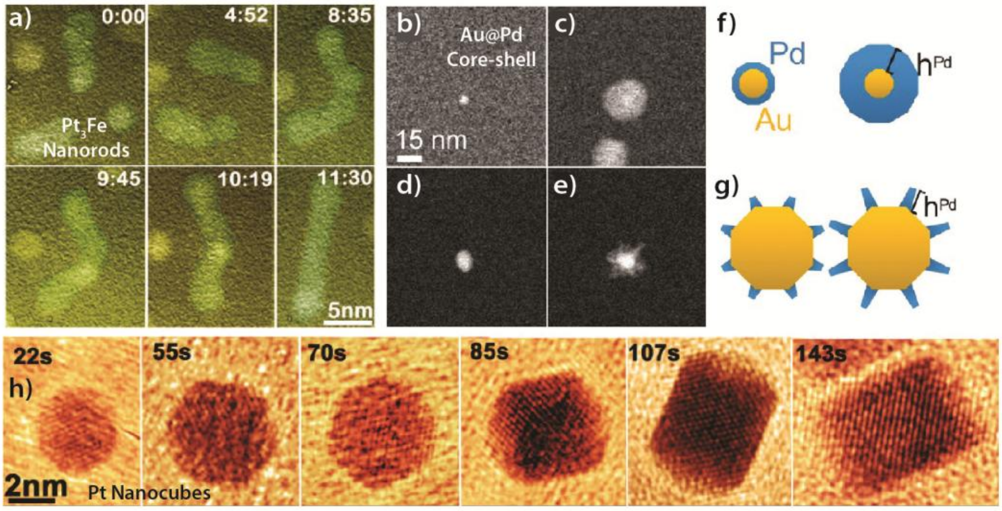

Figure 2.10 (a) The formation of twisted Pt_3Fe nanorods and the subsequent straightening process.[88] (b-g) Comparison of Pd growth on (b) 5 and (d) 15 nm Au seeds and (c) and (e) their corresponding Au@Pd core-shell nanostructures. The schematic in (f) and (g) illustrate the final morphologies of the two sizes Au seeds.[95] (h) Sequential high-resolution TEM images showing the growth of a single Pt nanocube.[87] Figure (a) reprinted from ref. 88, with permission from the American Association for the Advancement of Science, Copyright 2012,

(b-g) reprinted from ref. 95, with permission from American Chemical Society, Copyright 2013, (h) reprinted from ref. 87 with permission from The American Association for the Advancement of Science, Copyright 2014.

3. High resolution imaging using graphene liquid cells

The graphene liquid cell as shown in Figure 2.11 (a) and (b) has enabled the study of colloidal nanocrystal growth with excellent high resolution imaging. This is because electron scattering due to the thin membrane window can be minimized. Yuk *et al.*[96] used this new type of LC to explore the mechanism of platinum nanocrystal growth and discovered site-selective coalescence (Figure 2.11 c), structural reshaping after coalescence, and surface faceting along the growth trajectories. A disadvantage of graphene liquid cells is their limited size; they are typically less than 100 nm in diameter.

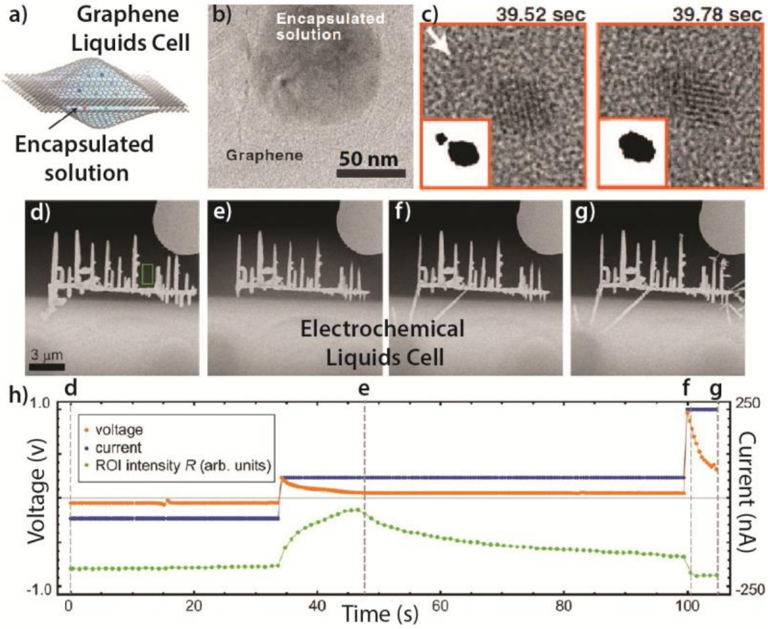

Figure 2.11 (a) A schematic illustration of a graphene liquids cell (GLC), encapsulating a solution. (b) TEM image of a GLC. (c) Atomic –resolution TEM imaging indicates the Pt nanocrystal growth via coalescence.[96] (d-g) Time evolution of the dendritic structure and (h) its corresponding applied electrical potential and measured electrical current. The intensity R

from the ROI indicated by the green box demonstrates the sensitivity of the Pb^{2+} ions concentration to the STEM beam's sensitivity.[97] Figure (a-c) reprinted from ref. 96 with permission from the American Association for the Advancement of Science, Copyright 2012, (d-h) reprinted from ref. 97 with permission from American Chemical Society, Copyright 2012.

4. Electrochemical liquid cells

The electrochemical deposition of metal clusters or dendritic structures has attracted a lot of attention due to its relevance to batteries and fuel cells[98]. White *et al.*[97] reported the electrochemical deposition of lead from an aqueous solution of lead (II) nitrate (Figure 2.11 d-g). Both the lead deposits and the local Pb^{2+} concentration were monitored. They used quantitative image analysis to extract the rate of Pb deposition and found that the current passed through the sample correlated well as shown in Figure 2.11 (h).

5. Nanoparticle motion

Motion of nanoparticles in growth solutions may dominated by Brownian motion, chemical reaction-induced local concentration gradient, liquid flow, electron beam effects during TEM observation, etc. Zheng *et al.*[99] studied the diffusion of spherical and rod-shaped gold nanoparticles in water with 15% glycerol. It was observed that nanoparticles show random Brownian motion plus jumps. Long distance motion due to liquid drag was also recorded. de Jonge *et al.*[100] used STEM to image gold nanoparticles in several micrometer thicken films of water. White *et al.*[101] studied the charged Pt nanoparticle dynamics in water and Mueller *et al.*[102] captured the motion of gold nanorods in a flow cell. Liu *et al.*[90] studied the self-assembly of charged gold nanoparticles in liquid. Park *et al.*[89] directly observed nanoparticle super lattice formation. Lu *et al.*[92] studied the dynamics of NPs in a single nanodroplet and they reported the motion is heavily damped by the strong particle-surface interactions mediated by the few atomic layers of liquids between them (Figure 2.12 a). Aabdin *et al.*[103] reported that the critical misalignment angle for nanocrystals (Figure 2.12 b) to merge would result in two distinct bonding pathways for two gold nanoparticles undergoing merging process involving defect-free and defect-mediated attachment of the NPs.

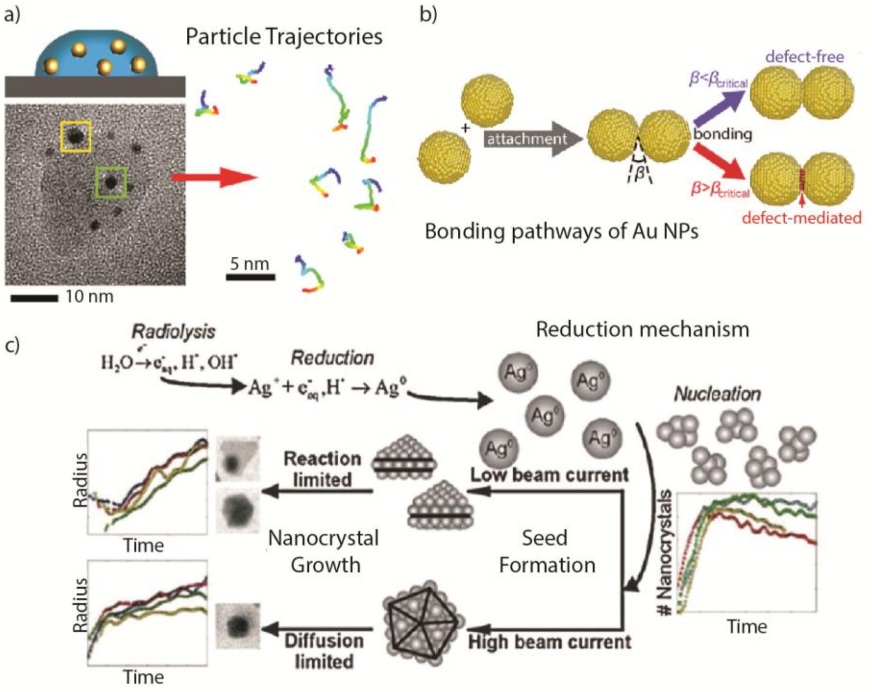

Figure 2.12 (a) Schematic diagram and TEM image showing the motion of nanoparticles in a nanodroplet.[92] (b) Schematic illustrates the bonding pathways of two Au nanoparticles in term of critical misalignment angle.[103] (c) Schematic of beam induce growth of Ag nanoparticles.[104] Figure (a) reprinted from ref. 92 with permission from American Chemical Society, Copyright 2014, (b) reprinted from ref. 103 with permission from American Chemical Society, Copyright 2014, (c) reprinted from ref. 104 with permission from American Chemical Society, Copyright 2012.

6. Reduction mechanisms and electron beam effects

An electron beam not only reduces dissolved metal salt ions, but also produces bubbles in liquids, generates solvated ions/electrons and may flatten and move the studied liquid film. Thus, the reactions under electron beam irradiation can be complex and the efforts to elucidate nanoparticle growth mechanisms under electron beam irradiation are highly valuable for the understanding of nanocrystal growth in general. Woehl *et al.*[104] studied silver particle growth by using a flow cell and found that electron beam current played a major role in controlling the morphology of silver nanocrystals (Figure 2.12 c). It was demonstrated that under a low beam current, reaction-limited growth was preferred and nanocrystals with faceted structures were obtained. Under a higher beam current, diffusion limited growth was dominant and nanocrystals with more complex shapes were formed. Isolation of these two growth regimes showed a new level of control over nanocrystal growth under electron beam irradiation.

2.5.2. Engineering the Gold and Silver Nanostructures via Control of Elemental Composition

Galvanic replacement reactions and core-shell nanoparticle formation have attracted much attention due to their versatility to generate novel metal nanostructures with tuneable and well-controlled properties. For instance, the localized surface plasmon resonances (LSPR) of Ag-Au alloy nanocages formed via a galvanic replacement reaction can be tuned across the visible regime and into the NIR.[105] The Ag@Au core-shell nanostructure exhibits one strong peak at ~500 nm wavelength together with a broad shoulder at ~400 nm[106] which is different from the Au and Ag individual particles (Au at 520 nm, Ag at 400 nm).[107]

2.5.2.1. Galvanic Replacement

Galvanic replacement reactions are used to prepare bimetallic/alloy nanostructures based in which the metal ions with higher oxidation potentials undergo reduction by oxidizing the metal present on the nanoparticle.[108-109] Silver nanocubes are often used as sacrificial templates for galvanic replacement reactions with different oxidizing agents such as aurate ($HAuCl_4$),[109-110] platinum (II) ions (Na_2PtCl_4),[111] palladium (II) ions (Na_2PdCl_4).[112] In this study, we focus on the replacement of Ag with Au resulting in the formation of nanobox/hollow nanostructures composed of Au-Ag alloy single crystals. More complex structures could be generated by coupling galvanic reactions with other chemical/physical processes. For instance, Sun *et al.* has fabricated hollow metal nanostructures with multiple walls by coupling galvanic replacement with sequentially deposited templates where specifically single-walled Au-Ag nanoshells were first prepared via galvanic replacement, subsequently followed by reduction and another round of galvanic replacement to generate double-walled nanoshells, by repeating the cycle to produce multi-walled nanostructures.[113] While González *et al.* has fabricated Au-Ag double-walled nanoboxes preparation through simultaneous galvanic replacement and Kirkendall effect.[114]

For galvanic replacement between Ag nanocubes and aurate, Sun *et al.*[115] identified three distinct steps in the reaction of silver nanostructures with chloroauric acid by *ex-situ* TEM imaging (Figure 2.13 a and b): (i) pinholes form in the silver nanocubes via etching of the Ag by the aurate, (ii) the dissolution of silver nanocubes which also an Au-Ag alloy forms on cubes walls, and (iii) de-alloying, followed by growth of the Au layer at the expense of the Ag until finally the Au structures form.

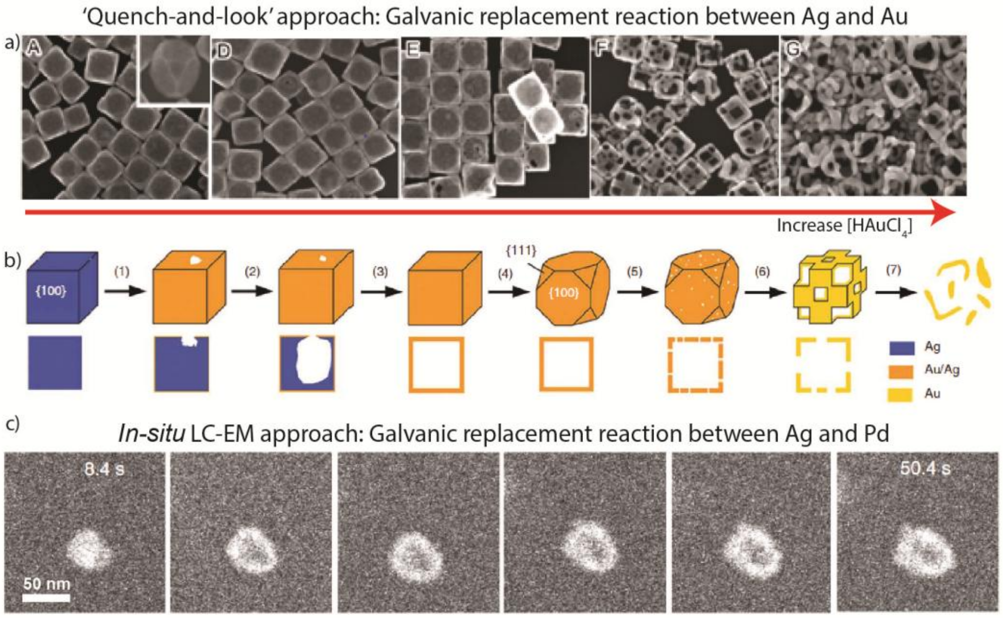
'Quench-and-look' approach: Galvanic replacement reaction between Ag and Au

In-situ LC-EM approach: Galvanic replacement reaction between Ag and Pd

Figure 2.13 (a) Mechanism proposed and (b) schematic based on the *ex-situ* SEM observation, the so-called 'quench-and-look' approach for galvanic replacement reaction between Ag and Au.[115] (c) *In-situ* liquid cell-electron microscopy (LC-EM) used for observing the galvanic replacement reaction between Ag and Pd.[116] Figure (a) and (b) reprinted from ref. 115 with permission from American Chemical Society, Copyright 2004, (c) reprinted from ref. 116 with permission from Nature Publishing Group, Copyright 2014.

Sun *et al.*[117] have also proposed that the galvanic replacement between silver nanowires and $HAuCl_4$ involves multiple steps, based on the images recorded by using *in-situ* transmission X-ray microscopy (TXM) in combination with a flow cell reactor: (i) local initiation of the pitting process (ii) anisotropic etching of the silver nanowires and uniform coating of gold and (iii) reconstruction of the nanotube walls via the Ostwald ripening process.

However, the spatial resolution of the TXM is rather low, 10-25 nm, relative to conventional TEM imaging which routinely achieves sub-nanometer resolution.

Sutter *et al.*[116] have performed *in-situ* liquid-cell imaging of galvanic replacement reactions between silver nanoparticles and $PdCl_2$ (Figure 2.13 c). They captured the transformation of solid silver nanoparticles into hollow silver-palladium nanostructures and compared the results of *in-situ* and *ex-situ* preparation on the reaction rates. For *in-situ* reactions, it takes 8 seconds to observe significant changes while the same reaction *ex-situ* requires ~2 hours. They attribute this to the presence of hydrated electrons, which are generated when the electron beam interacts with the specimen, and significantly accelerate the reaction. However, a quantification on the reaction rate is still lacking.

2.5.2.2. Core-Shell Nanostructures

Core-shell nanoparticles are highly functionalized nanoparticles with distinctive properties that originate from their different constituent materials. The properties of core-shell nanoparticles can be tuned by either changing the constituting materials or the core to shell ratio.[118] This tunability makes it possible to manipulate the surface properties so as to meet the requirements for diverse applications.

The fabrication of core-shell nanoparticles with different morphologies and compositions can be accomplished by various chemical/physical methods.[119-121] The synthesis parameters are derived empirically and the final nanoparticle morphology is confirmed with *ex-situ* imaging. However, early stages of the reaction and intermediate structures cannot be investigated this way.

It is also well-known that the electron beam itself can act as a reducing agent and reduce metal ions into atoms through the action of solvated electrons (from radiolysis of water). This effect has been exploited for dynamical studies of silver[104, 122] nanoparticle nucleation directly from solution. Recently, Jungjohann *et al.*[95] and Wu *et al.*[50] demonstrated the use of *in-situ* liquid cell microscopy to study the solution growth of Au@Pd (Figure 2.14 a and b) and Pt@Au (Figure 2.14 c, d and e) core-shell nanoparticles respectively. In both studies, the electron beam replaces the reducing agent, leading to metal deposition.

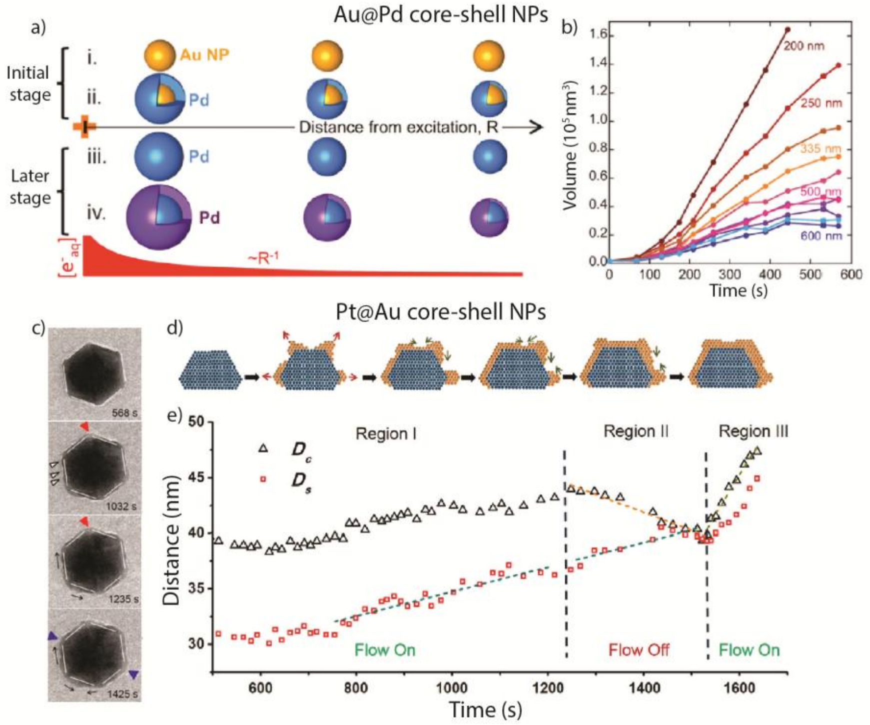

Figure 2.14 (a) Schematic showing the growth of Pd on Au core nanoparticles in two stages. (b) The particle volume evolution as a function of time for particles at different distances from the excitation spot as indicated in (a).[123] (c) Time-lapsed TEM images, (d) schematic and (e) quantitative analysis of the growth of Au on Pt icosahedron core nanoparticles.[50] Figure (a)

and (b) reprinted from ref. 123 with permission from American Chemical Society, Copyright 2014, (c) and (d) reprinted from ref. 50 with permission from American Chemical Society, Copyright 2015.

Sutter *et al.*[123] further demonstrated the use of *in-situ* TEM to quantify the palladium deposition rate on Au nanoparticles as a function of distance and beam currents. They reported a first-order reaction rate with respect to the concentration of hydrated electrons. The quantitative data acquisition is excellent but this study only focuses on electron beam effects and reduction mechanisms.

Fine-tuning of the structure, i.e., the dominant crystalline facets and surface composition is important for applications such as plasmonics and can be accomplished with the addition of different chemicals.[119] As such, the interplay of different chemical additives, such as surfactants and reducing agents, etc., remains largely unresolved.

2.6. Conclusions and Outlook

The ability to precisely control the structural and opto-electronic properties between two closely-spaced nanoparticles and the understanding of the stability of the nanostructures are the keys to study quantum-plasmonic effects at sub-nanometer length scales. The level of control requires a deeper understanding of gap engineering in nanoparticle dimers and controlling their composition. Although many experimental and theoretical studies have been proposed to observe indirectly the quantum tunnelling effects, direct experimental access to the resulting tunneling charge transfer plasmon mode is still lacking. In order to achieve this, self-assembly of nanoparticles with sub-nanometer separations by well-controlled characterization techniques is required to study plasmon-induced electron tunneling conclusively. In addition, experiments involving *in-situ* liquid cell microscopy would also provide a way to study the reaction chemistry and kinetics during the nanoparticle synthesis so as to engineer the composition of the nanostructures which is expected to open up more opportunities for application in plasmonics.

2.7. References

1. Zentgraf, T.; Liu, Y.; Mikkelsen, M. H.; Valentine, J.; Zhang, X., Plasmonic Luneburg and Eaton lenses. *Nature Nanotechnology* **2011,** *6* (3), 151-155.
2. Liu, Y.; Zhang, X., Metamaterials: a new frontier of science and technology. *Chemical Society Reviews* **2011,** *40* (5), 2494-2507.
3. Wang, X. F.; Liu, R. H.; Gui, Z.; Xie, Y. L.; Yan, Y. J.; Ying, J. J.; Luo, X. G.; Chen, X. H., Superconductivity at 5 K in alkali-metal-doped phenanthrene. *Nature Communications* **2011,** *2*, 507.
4. Fang, N.; Lee, H.; Sun, C.; Zhang, X., Sub–Diffraction-Limited Optical Imaging with a Silver Superlens. *Science* **2005,** *308* (5721), 534-537.
5. Kawata, S.; Ono, A.; Verma, P., Subwavelength colour imaging with a metallic nanolens. *Nature Photonics* **2008,** *2* (7), 438-442.
6. Hsiao-Kuan Yuan, U. K. C., Wenshan Cai, Alexander V. Kildishev, Alexandra Boltasseva, Vladimir P. Drachev, and Vladimir M. Shalaev, A negative permeability material at red light. *Optics Express* **2007,** *15* (3), 1076-1083.
7. Shen, H.; Bienstman, P.; Maes, B., Plasmonic absorption enhancement in organic solar cells with thin active layers. *Journal of Applied Physics* **2009,** *106* (7), 073109.
8. MacDonald, K. F.; Samson, Z. L.; Stockman, M. I.; Zheludev, N. I., Ultrafast active plasmonics. *Nature Photonics* **2009,** *3* (1), 55-58.

9. Atwater, H. A.; Polman, A., Plasmonics for improved photovoltaic devices. *Nature Materials* **2010,** *9* (3), 205-213.

10. Ozbay, E., Plasmonics: Merging Photonics and Electronics at Nanoscale Dimensions. *Science* **2006,** *311* (5758), 189-193.

11. Mayer, K. M.; Hafner, J. H., Localized Surface Plasmon Resonance Sensors. *Chemical Reviews* **2011,** *111* (6), 3828-3857.

12. Willets, K. A.; Van Duyne, R. P., Localized Surface Plasmon Resonance Spectroscopy and Sensing. *Annual Review of Physical Chemistry* **2007,** *58* (1), 267-297.

13. Barnes, W. L.; Dereux, A.; Ebbesen, T. W., Surface plasmon subwavelength optics. *Nature* **2003,** *424* (6950), 824-830.

14. Zia, R.; Schuller, J. A.; Chandran, A.; Brongersma, M. L., Plasmonics: the next chip-scale technology. *Materials Today* **2006,** *9* (7–8), 20-27.

15. Esteban, R.; Borisov, A. G.; Nordlander, P.; Aizpurua, J., Bridging quantum and classical plasmonics with a quantum-corrected model. *Nature Communications* **2012,** *3,* 825.

16. Wu, L.; Duan, H.; Bai, P.; Bosman, M.; Yang, J. K. W.; Li, E., Fowler–Nordheim Tunneling Induced Charge Transfer Plasmons between Nearly Touching Nanoparticles. *ACS Nano* **2012,** *7* (1), 707-716.

17. Savage, K. J.; Hawkeye, M. M.; Esteban, R.; Borisov, A. G.; Aizpurua, J.; Baumberg, J. J., Revealing the quantum regime in tunnelling plasmonics. *Nature* **2012,** *491* (7425), 574-577.

18. Scholl, J. A.; García-Etxarri, A.; Koh, A. L.; Dionne, J. A., Observation of Quantum Tunneling between Two Plasmonic Nanoparticles. *Nano Letters* **2012,** *13* (2), 564-569.

19. Duan, H.; Fernández-Domínguez, A. I.; Bosman, M.; Maier, S. A.; Yang, J. K. W., Nanoplasmonics: Classical down to the Nanometer Scale. *Nano Letters* **2012,** *12* (3), 1683-1689.

20. Osberg, K. D.; Rycenga, M.; Harris, N.; Schmucker, A. L.; Langille, M. R.; Schatz, G. C.; Mirkin, C. A., Dispersible Gold Nanorod Dimers with Sub-5 nm Gaps as Local Amplifiers for Surface-Enhanced Raman Scattering. *Nano Letters* **2012,** *12* (7), 3828-3832.

21. Chen, X.; Jeon, Y.-M.; Jang, J.-W.; Qin, L.; Huo, F.; Wei, W.; Mirkin, C. A., On-Wire Lithography-Generated Molecule-Based Transport Junctions:

A New Testbed for Molecular Electronics. *Journal of the American Chemical Society* **2008,** *130* (26), 8166-8168.

22. Chen, X.; Braunschweig, A. B.; Wiester, M. J.; Yeganeh, S.; Ratner, M. A.; Mirkin, C. A., Spectroscopic Tracking of Molecular Transport Junctions Generated by Using Click Chemistry. *Angewandte Chemie International Edition* **2009,** *48* (28), 5178-5181.

23. Chen, X.; Yeganeh, S.; Qin, L.; Li, S.; Xue, C.; Braunschweig, A. B.; Schatz, G. C.; Ratner, M. A.; Mirkin, C. A., Chemical Fabrication of Heterometallic Nanogaps for Molecular Transport Junctions. *Nano Letters* **2009,** *9* (12), 3974-3979.

24. Banholzer, M. J.; Qin, L.; Millstone, J. E.; Osberg, K. D.; Mirkin, C. A., On-wire lithography: synthesis, encoding and biological applications. *Nature Protocols* **2009,** *4* (6), 838-848.

25. Braunschweig, A. B.; Schmucker, A. L.; Wei, W. D.; Mirkin, C. A., Nanostructures enabled by On-Wire Lithography (OWL). *Chemical Physics Letters* **2010,** *486* (4–6), 89-98.

26. Osberg, K. D.; Schmucker, A. L.; Senesi, A. J.; Mirkin, C. A., One-Dimensional Nanorod Arrays: Independent Control of Composition, Length, and Interparticle Spacing with Nanometer Precision. *Nano Letters* **2011,** *11* (2), 820-824.

27. Qin, L.; Jang, J.-W.; Huang, L.; Mirkin, C. A., Sub-5-nm Gaps Prepared by On-Wire Lithography: Correlating Gap Size with Electrical Transport. *Small* **2007,** *3* (1), 86-90.

28. Qin, L.; Park, S.; Huang, L.; Mirkin, C. A., On-Wire Lithography. *Science* **2005,** *309* (5731), 113-115.

29. Qin, L.; Zou, S.; Xue, C.; Atkinson, A.; Schatz, G. C.; Mirkin, C. A., Designing, fabricating, and imaging Raman hot spots. *Proceedings of the National Academy of Sciences* **2006,** *103* (36), 13300-13303.

30. Bosman, M.; Zhang, L.; Duan, H.; Tan, S. F.; Nijhuis, C. A.; Qiu, C. W.; Yang, J. K. W., Encapsulated Annealing: Enhancing the Plasmon Quality Factor in Lithographically–Defined Nanostructures. *Sci. Rep.* **2014,** *4*.

31. Broers, A. N.; Molzen, W. W.; Cuomo, J. J.; Wittels, N. D., Electron-beam fabrication of 80-Å metal structures. *Applied Physics Letters* **1976,** *29* (9), 596-598.

32. Cord, B.; Yang, J.; Duan, H.; Joy, D. C.; Klingfus, J.; Berggren, K. K., Limiting factors in sub-10nm scanning-electron-beam lithography. *Journal of Vacuum Science & Technology B* **2009,** *27* (6), 2616-2621.

33. Ou, F. S.; Hu, M.; Naumov, I.; Kim, A.; Wu, W.; Bratkovsky, A. M.; Li, X.; Williams, R. S.; Li, Z., Hot-Spot Engineering in Polygonal Nanofinger Assemblies for Surface Enhanced Raman Spectroscopy. *Nano Letters* **2011,** *11* (6), 2538-2542.

34. Caswell, K. K.; Wilson, J. N.; Bunz, U. H. F.; Murphy, C. J., Preferential End-to-End Assembly of Gold Nanorods by Biotin−Streptavidin Connectors. *Journal of the American Chemical Society* **2003,** *125* (46), 13914-13915.

35. Henzie, J.; Andrews, S. C.; Ling, X. Y.; Li, Z.; Yang, P., Oriented assembly of polyhedral plasmonic nanoparticle clusters. *Proceedings of the National Academy of Sciences* **2013,** *110* (17), 6640-6645.

36. Baranov, D.; Manna, L.; Kanaras, A. G., Chemically induced self-assembly of spherical and anisotropic inorganic nanocrystals. *Journal of Materials Chemistry* **2011,** *21* (42), 16694-16703.

37. Jones, S. T.; Taylor, R. W.; Esteban, R.; Abo-Hamed, E. K.; Bomans, P. H. H.; Sommerdijk, N. A. J. M.; Aizpurua, J.; Baumberg, J. J.; Scherman, O. A., Gold Nanorods with Sub-Nanometer Separation using Cucurbit[n]uril for SERS Applications. *Small* **2014,** *10* (21), 4298-4303.

38. Wang, L.; Zhu, Y.; Xu, L.; Chen, W.; Kuang, H.; Liu, L.; Agarwal, A.; Xu, C.; Kotov, N. A., Side-by-Side and End-to-End Gold Nanorod Assemblies for Environmental Toxin Sensing. *Angewandte Chemie International Edition* **2010,** *49* (32), 5472-5475.

39. Gao, B.; Arya, G.; Tao, A. R., Self-orienting nanocubes for the assembly of plasmonic nanojunctions. *Nature Nanotechnology* **2012,** *7* (7), 433-437.

40. Kasera, S.; Biedermann, F.; Baumberg, J. J.; Scherman, O. A.; Mahajan, S., Quantitative SERS Using the Sequestration of Small Molecules Inside Precise Plasmonic Nanoconstructs. *Nano Letters* **2012,** *12* (11), 5924-5928.

41. DeVries, G. A.; Brunnbauer, M.; Hu, Y.; Jackson, A. M.; Long, B.; Neltner, B. T.; Uzun, O.; Wunsch, B. H.; Stellacci, F., Divalent Metal Nanoparticles. *Science* **2007,** *315* (5810), 358-361.

42. Shevchenko, E. V.; Talapin, D. V.; Kotov, N. A.; O'Brien, S.; Murray, C. B., Structural diversity in binary nanoparticle superlattices. *Nature* **2006,** *439* (7072), 55-59.

43. Sun, Z.; Luo, Z.; Fang, J., Assembling Nonspherical 2D Binary Nanoparticle Superlattices by Opposite Electrical Charges: The Role of Coulomb Forces. *ACS Nano* **2010,** *4* (4), 1821-1828.

44. Zhang, S.; Kou, X.; Yang, Z.; Shi, Q.; Stucky, G. D.; Sun, L.; Wang, J.; Yan, C., Nanonecklaces assembled from gold rods, spheres, and bipyramids. *Chemical Communications* **2007,** (18), 1816-1818.

45. Liu, K.; Nie, Z.; Zhao, N.; Li, W.; Rubinstein, M.; Kumacheva, E., Step-Growth Polymerization of Inorganic Nanoparticles. *Science* **2010,** *329* (5988), 197-200.

46. Liu, K.; Lukach, A.; Sugikawa, K.; Chung, S.; Vickery, J.; Therien-Aubin, H.; Yang, B.; Rubinstein, M.; Kumacheva, E., Copolymerization of Metal Nanoparticles: A Route to Colloidal Plasmonic Copolymers. *Angewandte Chemie* **2014,** *126* (10), 2686-2691.

47. Rycenga, M.; McLellan, J. M.; Xia, Y., Controlling the Assembly of Silver Nanocubes through Selective Functionalization of Their Faces. *Advanced Materials* **2008,** *20* (12), 2416-2420.

48. Wang, Y.; DePrince, A. E.; K. Gray, S.; Lin, X.-M.; Pelton, M., Solvent-Mediated End-to-End Assembly of Gold Nanorods. *The Journal of Physical Chemistry Letters* **2010,** *1* (18), 2692-2698.

49. Fava, D.; Nie, Z.; Winnik, M. A.; Kumacheva, E., Evolution of Self-Assembled Structures of Polymer-Terminated Gold Nanorods in Selective Solvents. *Advanced Materials* **2008,** *20* (22), 4318-4322.

50. Wu, J.; Gao, W.; Wen, J.; Miller, D. J.; Lu, P.; Zuo, J.-M.; Yang, H., Growth of Au on Pt Icosahedral Nanoparticles Revealed by Low-Dose In Situ TEM. *Nano Letters* **2015,** *15* (4), 2711-2715.

51. Zhang, Q.; Li, W.; Moran, C.; Zeng, J.; Chen, J.; Wen, L.-P.; Xia, Y., Seed-Mediated Synthesis of Ag Nanocubes with Controllable Edge Lengths in

the Range of 30−200 nm and Comparison of Their Optical Properties. *Journal of the American Chemical Society* **2010,** *132* (32), 11372-11378.

52. Zeng, J.; Zheng, Y.; Rycenga, M.; Tao, J.; Li, Z.-Y.; Zhang, Q.; Zhu, Y.; Xia, Y., Controlling the Shapes of Silver Nanocrystals with Different Capping Agents. *Journal of the American Chemical Society* **2010,** *132* (25), 8552-8553.

53. Link, S.; El-Sayed, M. A., Spectral Properties and Relaxation Dynamics of Surface Plasmon Electronic Oscillations in Gold and Silver Nanodots and Nanorods. *The Journal of Physical Chemistry B* **1999,** *103* (40), 8410-8426.

54. Wiley, B. J.; Im, S. H.; Li, Z.-Y.; McLellan, J.; Siekkinen, A.; Xia, Y., Maneuvering the Surface Plasmon Resonance of Silver Nanostructures through Shape-Controlled Synthesis. *The Journal of Physical Chemistry B* **2006,** *110* (32), 15666-15675.

55. Zeng, J.; Roberts, S.; Xia, Y., Nanocrystal-Based Time–Temperature Indicators. *Chemistry – A European Journal* **2010,** *16* (42), 12559-12563.

56. Schnell, M.; Garcia-Etxarri, A.; Huber, A. J.; Crozier, K. B.; Borisov, A.; Aizpurua, J.; Hillenbrand, R., Amplitude- and Phase-Resolved Near-Field Mapping of Infrared Antenna Modes by Transmission-Mode Scattering-Type Near-Field Microscopy. *The Journal of Physical Chemistry C* **2010,** *114* (16), 7341-7345.

57. Kern, J.; Großmann, S.; Tarakina, N. V.; Häckel, T.; Emmerling, M.; Kamp, M.; Huang, J.-S.; Biagioni, P.; Prangsma, J. C.; Hecht, B., Atomic-Scale Confinement of Resonant Optical Fields. *Nano Letters* **2012,** *12* (11), 5504-5509.

58. Lassiter, J. B.; Aizpurua, J.; Hernandez, L. I.; Brandl, D. W.; Romero, I.; Lal, S.; Hafner, J. H.; Nordlander, P.; Halas, N. J., Close Encounters between Two Nanoshells. *Nano Letters* **2008,** *8* (4), 1212-1218.

59. Ciracì, C.; Hill, R. T.; Mock, J. J.; Urzhumov, Y.; Fernández-Domínguez, A. I.; Maier, S. A.; Pendry, J. B.; Chilkoti, A.; Smith, D. R., Probing the Ultimate Limits of Plasmonic Enhancement. *Science* **2012,** *337* (6098), 1072-1074.

60. Yang, L.; Wang, H.; Yan, B.; Reinhard, B. M., Calibration of Silver Plasmon Rulers in the 1−25 nm Separation Range: Experimental Indications

of Distinct Plasmon Coupling Regimes. *The Journal of Physical Chemistry C* **2010,** *114* (11), 4901-4908.

61. Egerton, R. F.; Li, P.; Malac, M., Radiation damage in the TEM and SEM. *Micron* **2004,** *35* (6), 399-409.

62. Egerton, R. F., Mechanisms of radiation damage in beam-sensitive specimens, for TEM accelerating voltages between 10 and 300 kV. *Microscopy Research and Technique* **2012,** *75* (11), 1550-1556.

63. Hobbs, L. W., *Introduction to Analytical Electron Microscopy*. Plenum Press: New York, 1987.

64. Li, P. Electron Irradiation Damage to Organic Light-Emitting Materials. University of Alberta, Canada, 2003.

65. Chen, Y.; Palmer, R. E.; Wilcoxon, J. P., Sintering of Passivated Gold Nanoparticles under the Electron Beam. *Langmuir* **2006,** *22* (6), 2851-2855.

66. Lim, T. H.; McCarthy, D.; Hendy, S. C.; Stevens, K. J.; Brown, S. A.; Tilley, R. D., Real-Time TEM and Kinetic Monte Carlo Studies of the Coalescence of Decahedral Gold Nanoparticles. *ACS Nano* **2009,** *3* (11), 3809-3813.

67. Surrey, A.; Pohl, D.; Schultz, L.; Rellinghaus, B., Quantitative Measurement of the Surface Self-Diffusion on Au Nanoparticles by Aberration-Corrected Transmission Electron Microscopy. *Nano Letters* **2012,** *12* (12), 6071-6077.

68. Flüeli, M.; Buffat, P. A.; Borel, J. P., Real time observation by high resolution electron microscopy (HREM) of the coalescence of small gold particles in the electron beam. *Surface Science* **1988,** *202* (1–2), 343-353.

69. Batson, P. E.; Reyes-Coronado, A.; Barrera, R. G.; Rivacoba, A.; Echenique, P. M.; Aizpurua, J., Plasmonic Nanobilliards: Controlling Nanoparticle Movement Using Forces Induced by Swift Electrons. *Nano Letters* **2011,** *11* (8), 3388-3393.

70. David B. Carlson, J. E. E., *Low-Dose Imaging Techniques for Transmission Electron Microscopy, The Transmission Electron Microscope*. InTech: 2012.

71. Egerton, R. F., Chemical measurements of radiation damage in organic samples at and below room temperature. *Ultramicroscopy* **1980,** *5* (1–3), 521-523.

72. Salih, S. M.; Cosslett, V. E., Reduction in electron irradiation damage to organic compounds by conducting coatings. *Philosophical Magazine* **1974,** *30* (1), 225-228.

73. Fryer, J. R.; Holland, F., The reduction of radiation damage in the electron microscope. *Ultramicroscopy* **1983,** *11* (1), 67-70.

74. Egerton, R. F., Control of radiation damage in the TEM. *Ultramicroscopy* **2013,** *127* (0), 100-108.

75. Cryoprotection in electron microscopy. *Journal of Microscopy* **1986,** *141* (3), 385-391.

76. Egerton, R. F.; McLeod, R.; Wang, F.; Malac, M., Basic questions related to electron-induced sputtering in the TEM. *Ultramicroscopy* **2010,** *110* (8), 991-997.

77. Isaacson, M. S., *Principles and Techniques of Electron Microscopy*. 7th ed.; Van Nostrand: New York, 1973.

78. Egerton, R. F.; Crozier, P. A.; Rice, P., Electron energy-loss spectroscopy and chemical change. *Ultramicroscopy* **1987,** *23* (3–4), 305-312.

79. Strane, J.; Marks, L. D.; Luzzi, D. E.; Buckett, M. I.; Zhang, J. P.; Wessels, B. W., Encapsulation, diffusion and diet in the electron microscope. *Ultramicroscopy* **1988,** *25* (3), 253-257.

80. Mirsaidov, U. M.; Zheng, H.; Bhattacharya, D.; Casana, Y.; Matsudaira, P., Direct observation of stick-slip movements of water nanodroplets induced by an electron beam. *Proceedings of the National Academy of Sciences* **2012,** *109* (19), 7187-7190.

81. Zheng, H.; Smith, R. K.; Jun, Y.-w.; Kisielowski, C.; Dahmen, U.; Alivisatos, A. P., Observation of Single Colloidal Platinum Nanocrystal Growth Trajectories. *Science* **2009,** *324* (5932), 1309-1312.

82. Liao, H.-G.; Niu, K.; Zheng, H., Observation of growth of metal nanoparticles. *Chemical Communications* **2013,** *49* (100), 11720-11727.

83. Williamson, M. J.; Tromp, R. M.; Vereecken, P. M.; Hull, R.; Ross, F. M., Dynamic microscopy of nanoscale cluster growth at the solid-liquid interface. *Nature Materials* **2003,** *2* (8), 532-536.

84. Jonge, N. d.; Peckys, D. B.; Kremers, G. J.; Piston, D. W., Electron microscopy of whole cells in liquid with nanometer resolution. *Proceedings of the National Academy of Sciences* **2009,** *106* (7), 2159-2164.

85. Parent, L. R.; Robinson, D. B.; Woehl, T. J.; Ristenpart, W. D.; Evans, J. E.; Browning, N. D.; Arslan, I., Direct in Situ Observation of Nanoparticle Synthesis in a Liquid Crystal Surfactant Template. *ACS Nano* **2012,** *6* (4), 3589-3596.

86. Evans, J. E.; Jungjohann, K. L.; Browning, N. D.; Arslan, I., Controlled Growth of Nanoparticles from Solution with In Situ Liquid Transmission Electron Microscopy. *Nano Letters* **2011,** *11* (7), 2809-2813.

87. Liao, H.-G.; Zherebetskyy, D.; Xin, H.; Czarnik, C.; Ercius, P.; Elmlund, H.; Pan, M.; Wang, L.-W.; Zheng, H., Facet development during platinum nanocube growth. *Science* **2014,** *345* (6199), 916-919.

88. Liao, H.-G.; Cui, L.; Whitelam, S.; Zheng, H., Real-Time Imaging of Pt3Fe Nanorod Growth in Solution. *Science* **2012,** *336* (6084), 1011-1014.

89. Park, J.; Zheng, H.; Lee, W. C.; Geissler, P. L.; Rabani, E.; Alivisatos, A. P., Direct Observation of Nanoparticle Superlattice Formation by Using Liquid Cell Transmission Electron Microscopy. *ACS Nano* **2012,** *6* (3), 2078-2085.

90. Liu, Y.; Lin, X.-M.; Sun, Y.; Rajh, T., In Situ Visualization of Self-Assembly of Charged Gold Nanoparticles. *Journal of the American Chemical Society* **2013,** *135* (10), 3764-3767.

91. Jonge, N. d.; Dukes, M.; Kremers, G.; Northan, B.; Peckys, D.; Ring, E.; Piston, D.; Sougrat, R., Liquid and Three-Dimensional Scanning Transmission Electron Microscopy for Biological Specimen. *Microscopy and Microanalysis* **2009,** *15* (SupplementS2), 686-687.

92. Lu, J.; Aabdin, Z.; Loh, N. D.; Bhattacharya, D.; Mirsaidov, U., Nanoparticle Dynamics in a Nanodroplet. *Nano Letters* **2014,** *14* (4), 2111-2115.

93. Kraus, T.; de Jonge, N., Dendritic Gold Nanowire Growth Observed in Liquid with Transmission Electron Microscopy. *Langmuir* **2013,** *29* (26), 8427-8432.

94. Liao, H.-G.; Zheng, H., Liquid Cell Transmission Electron Microscopy Study of Platinum Iron Nanocrystal Growth and Shape Evolution. *Journal of the American Chemical Society* **2013,** *135* (13), 5038-5043.

95. Jungjohann, K. L.; Bliznakov, S.; Sutter, P. W.; Stach, E. A.; Sutter, E. A., In Situ Liquid Cell Electron Microscopy of the Solution Growth of Au–Pd Core–Shell Nanostructures. *Nano Letters* **2013,** *13* (6), 2964-2970.

96. Yuk, J. M.; Park, J.; Ercius, P.; Kim, K.; Hellebusch, D. J.; Crommie, M. F.; Lee, J. Y.; Zettl, A.; Alivisatos, A. P., High-Resolution EM of Colloidal Nanocrystal Growth Using Graphene Liquid Cells. *Science* **2012,** *336* (6077), 61-64.

97. White, E. R.; Singer, S. B.; Augustyn, V.; Hubbard, W. A.; Mecklenburg, M.; Dunn, B.; Regan, B. C., In Situ Transmission Electron Microscopy of Lead Dendrites and Lead Ions in Aqueous Solution. *ACS Nano* **2012,** *6* (7), 6308-6317.

98. Leenheer, A. J.; Jungjohann, K. L.; Zavadil, K. R.; Sullivan, J. P.; Harris, C. T., Lithium Electrodeposition Dynamics in Aprotic Electrolyte Observed in Situ via Transmission Electron Microscopy. *ACS Nano* **2015,** *9* (4), 4379-4389.

99. Zheng, H.; Claridge, S. A.; Minor, A. M.; Alivisatos, A. P.; Dahmen, U., Nanocrystal Diffusion in a Liquid Thin Film Observed by in Situ Transmission Electron Microscopy. *Nano Letters* **2009,** *9* (6), 2460-2465.

100. de Jonge, N.; Poirier-Demers, N.; Demers, H.; Peckys, D. B.; Drouin, D., Nanometer-resolution electron microscopy through micrometers-thick water layers. *Ultramicroscopy* **2010,** *110* (9), 1114-1119.

101. White, E. R.; Mecklenburg, M.; Shevitski, B.; Singer, S. B.; Regan, B. C., Charged Nanoparticle Dynamics in Water Induced by Scanning Transmission Electron Microscopy. *Langmuir* **2012,** *28* (8), 3695-3698.

102. Mueller, C.; Harb, M.; Dwyer, J. R.; Miller, R. J. D., Nanofluidic Cells with Controlled Pathlength and Liquid Flow for Rapid, High-Resolution In Situ Imaging with Electrons. *The Journal of Physical Chemistry Letters* **2013,** *4* (14), 2339-2347.

103. Aabdin, Z.; Lu, J.; Zhu, X.; Anand, U.; Loh, N. D.; Su, H.; Mirsaidov, U., Bonding Pathways of Gold Nanocrystals in Solution. *Nano Letters* **2014,** *14* (11), 6639-6643.

104. Woehl, T. J.; Evans, J. E.; Arslan, I.; Ristenpart, W. D.; Browning, N. D., Direct in Situ Determination of the Mechanisms Controlling Nanoparticle Nucleation and Growth. *ACS Nano* **2012,** *6* (10), 8599-8610.

105. Skrabalak, S. E.; Chen, J.; Sun, Y.; Lu, X.; Au, L.; Cobley, C. M.; Xia, Y., Gold Nanocages: Synthesis, Properties, and Applications. *Accounts of Chemical Research* **2008,** *41* (12), 1587-1595.

106. Kahraman, M.; Aydın, Ö.; Çulha, M., Oligonucleotide-Mediated Au–Ag Core–Shell Nanoparticles. *Plasmonics* **2009,** *4* (4), 293-301.

107. Lim, D.-K.; Kim, I.-J.; Nam, J.-M., DNA-embedded Au/Ag core-shell nanoparticles. *Chemical Communications* **2008,** (42), 5312-5314.

108. Lin, W.; Warren, T. H.; Nuzzo, R. G.; Girolami, G. S., Surface-selective deposition of palladium and silver films from metal-organic precursors: a novel metal-organic chemical vapor deposition redox transmetalation process. *Journal of the American Chemical Society* **1993,** *115* (24), 11644-11645.

109. Sun, Y.; Xia, Y., Shape-Controlled Synthesis of Gold and Silver Nanoparticles. *Science* **2002,** *298* (5601), 2176-2179.

110. Skrabalak, S. E.; Au, L.; Li, X.; Xia, Y., Facile synthesis of Ag nanocubes and Au nanocages. *Nature Protocols* **2007,** *2* (9), 2182-2190.

111. Chen, J.; Wiley, B.; McLellan, J.; Xiong, Y.; Li, Z.-Y.; Xia, Y., Optical Properties of Pd−Ag and Pt−Ag Nanoboxes Synthesized via Galvanic Replacement Reactions. *Nano Letters* **2005,** *5* (10), 2058-2062.

112. Cobley, C. M.; Campbell, D. J.; Xia, Y., Tailoring the Optical and Catalytic Properties of Gold-Silver Nanoboxes and Nanocages by Introducing Palladium. *Advanced Materials* **2008,** *20* (4), 748-752.

113. Sun, Y.; Wiley, B.; Li, Z.-Y.; Xia, Y., Synthesis and Optical Properties of Nanorattles and Multiple-Walled Nanoshells/Nanotubes Made of Metal Alloys. *Journal of the American Chemical Society* **2004,** *126* (30), 9399-9406.

114. González, E.; Arbiol, J.; Puntes, V. F., Carving at the Nanoscale: Sequential Galvanic Exchange and Kirkendall Growth at Room Temperature. *Science* **2011,** *334* (6061), 1377-1380.

115. Sun, Y.; Xia, Y., Mechanistic Study on the Replacement Reaction between Silver Nanostructures and Chloroauric Acid in Aqueous Medium. *Journal of the American Chemical Society* **2004,** *126* (12), 3892-3901.

116. Sutter, E.; Jungjohann, K.; Bliznakov, S.; Courty, A.; Maisonhaute, E.; Tenney, S.; Sutter, P., In situ liquid-cell electron microscopy of silver–

palladium galvanic replacement reactions on silver nanoparticles. *Nature Communications* **2014,** *5*.

117. Sun, Y.; Wang, Y., Monitoring of Galvanic Replacement Reaction between Silver Nanowires and HAuCl4 by In Situ Transmission X-ray Microscopy. *Nano Letters* **2011,** *11* (10), 4386-4392.

118. Oldenburg, S. J.; Averitt, R. D.; Westcott, S. L.; Halas, N. J., Nanoengineering of optical resonances. *Chemical Physics Letters* **1998,** *288* (2–4), 243-247.

119. Tsuji, M.; Matsuo, R.; Jiang, P.; Miyamae, N.; Ueyama, D.; Nishio, M.; Hikino, S.; Kumagae, H.; Kamarudin, K. S. N.; Tang, X.-L., Shape-Dependent Evolution of Au@Ag Core−Shell Nanocrystals by PVP-Assisted N,N-Dimethylformamide Reduction. *Crystal Growth & Design* **2008,** *8* (7), 2528-2536.

120. Ma, Y.; Li, W.; Cho, E. C.; Li, Z.; Yu, T.; Zeng, J.; Xie, Z.; Xia, Y., Au@Ag Core−Shell Nanocubes with Finely Tuned and Well-Controlled Sizes, Shell Thicknesses, and Optical Properties. *ACS Nano* **2010,** *4* (11), 6725-6734.

121. Gong, J.; Zhou, F.; Li, Z.; Tang, Z., Synthesis of Au@Ag Core–Shell Nanocubes Containing Varying Shaped Cores and Their Localized Surface Plasmon Resonances. *Langmuir* **2012,** *28* (24), 8959-8964.

122. Noh, K. W.; Liu, Y.; Sun, L.; Dillon, S. J., Challenges associated with in-situ TEM in environmental systems: The case of silver in aqueous solutions. *Ultramicroscopy* **2012,** *116* (0), 34-38.

123. Sutter, E. A.; Sutter, P. W., Determination of Redox Reaction Rates and Orders by In Situ Liquid Cell Electron Microscopy of Pd and Au Solution Growth. *Journal of the American Chemical Society* **2014,** *136* (48), 16865-16870.

Chapter 3

Self-assembly of Silver Nanoparticles with Sub-Nanometer Separations

Abstract: *A bottom-up method was developed to fabricate structures of the form Ag-SAM-Ag (where SAM = self-assembled monolayer). Silver nanocubes with edge lengths of 30-40 nm were synthesized via established methods, with mixed SAMs of thiolates and dithiolates on their surfaces. The SAMs were used to control the self-assembly process and the width of the sub-nanometer gap sizes. The fabricated structures were characterized by various techniques: TEM, SEM, XPS, UPS, and UV/Vis. It was demonstrated that the SAMs control the structure's optical properties and provide molecular-electronic control over the barrier heights of the studied system. The synthesis routines discussed here will be used in the Chapter 4 to demonstrate quantum plasmonics.*

3.1. Introduction

Nanostructures with tunable gap sizes are good candidates to study plasmon-induced tunneling effects[1-3] or surface-enhanced Raman spectroscopy (SERS) enhancement.[4-5] These structures are challenging to fabricate by top-down nanofabrication techniques such as electron-beam lithography (EBL), because of resolution limitations. Additionally, top-down approaches only yield polycrystalline structures that suffer from defects and plasmon damping.[6-9]

On the other hand, sub-nanometer gaps are relatively easily achievable by wet-chemical solution processing methods. Wet chemical or bottom-up approaches have been widely used for the fabrication of silver nanoparticles with different sizes and shapes and with high monodispersity. Despite their single-crystallinity, the atomically smooth surfaces also enable the formation of interparticle gaps with distinct and flat interfaces. Moreover, wet chemical method facilitates the production of single-crystalline defect-free silver nanostructures with sub-nanometer gap sizes at massive scales.

In this Chapter, we report a new method to prepare crystalline structures of Ag plasmonic resonators with edge lengths of 30-40 nm and with high aspect ratio nano-gaps by functionalizing the silver nanocube surfaces with mixed self-assembled monolayers (SAMs) of thiolates and dithiolates. The SAMs were used to control the sub-nanometer gap sizes and optical properties between two silver nanoparticles. We characterized the functionalized nanoparticles with transmission electron microscopy (TEM), UV-visible spectroscopy (UV-Vis), X-ray photoelectron spectroscopy (XPS), UV-Violet photoelectron spectroscopy (UPS) and 3D scanning TEM tomography.

3.2. Results & Discussion

3.2.1. Synthesis and Functionalization of Silver Nanocubes

We used single crystalline silver nanocubes to form dimers for three reasons. (i) These particles can be functionalized with ligands with a length of approx. 0.5 nm to 2 nm which can direct the self-assembly of dimers and the gap size. (ii) These particles have atomically flat surfaces, resulting in defect free nanogaps. (iii) These particles have high aspect ratios of the nanogap that can be controlled by controlling particle size and the length of the molecule.

We followed the polyol method developed by the Xia's group to chemically synthesize the single-crystalline silver nanocubes.[10] The experimental details of the synthetic procedures and characterization techniques are reported in the experimental section at the end of this Chapter. Here, we only give a brief description.

In this reaction, ethylene glycol acts as both solvent and reducing agent while sodium sulfide acts as the catalyst. The silver nitrate is used as the silver precursor. The polymer, poly (vinyl) pyrrolidone (PVP) was used as a surfactants which selectively capped the {100} facets of the nanocrystals. The careful control among the ratios of these four reactants and temperature enables the formation of silver nanocubes with PVP stabilized {100} facets.

The silver nanocubes were functionalized with mixed self-assembled monolayers (SAMs) of thiolates and ditholates to form dimers and avoid aggregation (Figure 3.1 a). The molecules not only could act as the linkers to determine the gap sizes between two nanocubes (Figure 3.1 b and c), but also could alter the opto-electronic properties of such a Ag-SAMs-Ag plasmonic system (Figure 3.1 d).

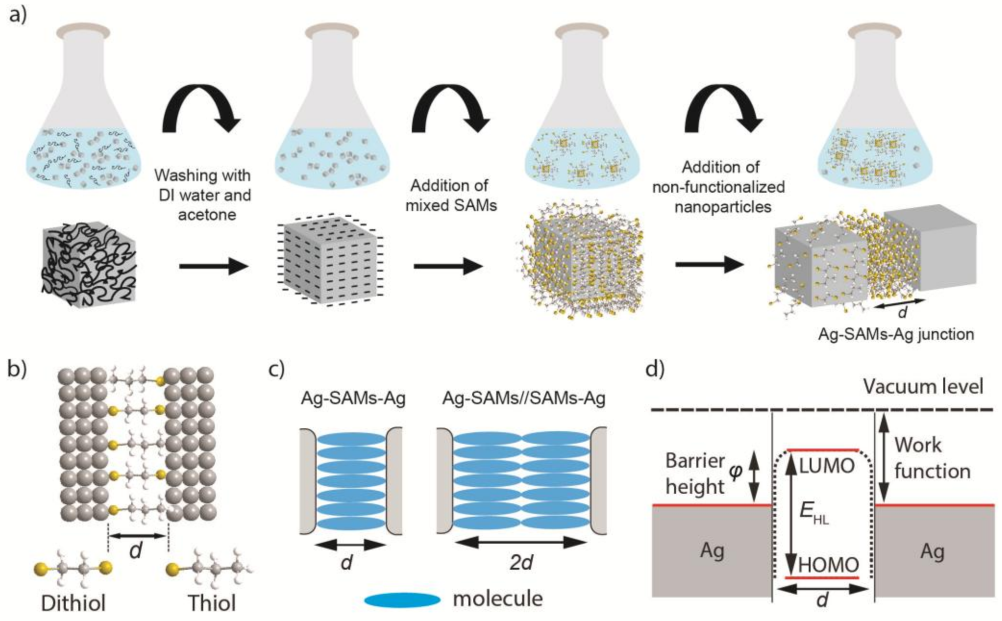

Figure 3.1 (a) Schematic of the surface modification process. (b) The distance between two adjacent nanoparticles is determined by the thickness of the self-assembled monolayers (SAMs). (c) Two types of junctions are possible in our system. (d) A schematic energy-level diagram of the junctions.

Figure 3.1 schematically shows the modification process. First, the silver nanoparticles with cuboidal shapes were dispersed in freshly-distilled ethanol after washing thoroughly with water and acetone in order to get rid of the polymer residue present during nanoparticles synthesis. Subsequently, we added the mixed SAM solution to change the dielectric environment of the nanocubes. In a second step, these functionalized nanoparticles were mixed with non-functionalized particles to form predominantly dimeric structures.

3.2.2. Transmission Electron Microscope (TEM) Gap Size Characterization

We characterized the functionalized nanoparticles with transmission electron microscopy (TEM), UV-visible spectroscopy (UV-Vis), X-ray photoelectron spectroscopy (XPS), UV-Violet photoelectron spectroscopy (UPS) and 3D Scanning TEM (3D STEM) Tomography.

Figure 3.2 (a) shows a TEM overview image of the chemically-synthesized silver nanocubes that are capped with thick layer of PVP. The edge length of the nanocubes is about 30-40 nm. Figure 3.2 (b) shows a TEM image and its electron diffraction pattern of a single-crystalline silver cube drop-casted on 30-nm thick SiN_x membrane. The electron diffraction (inset) suggests that the silver nanocubes were single crystalline and bounded by {100} facets. Figure 3.2 (c) is a representative TEM overview image of the Ag nanocubes after functionalization with mixed SAMs of PT and BDT. We typically obtained 20-30% dimeric structures; the remainders were single particles, or trimeric structures or larger aggregates. Figure 3.2 (d) shows a typical image of a dimer consisting of two silver nanocubes aligned parallel to each other and the inset shows a high resolution scanning TEM image (STEM) of the gap region, which is about 0.8 nm wide.

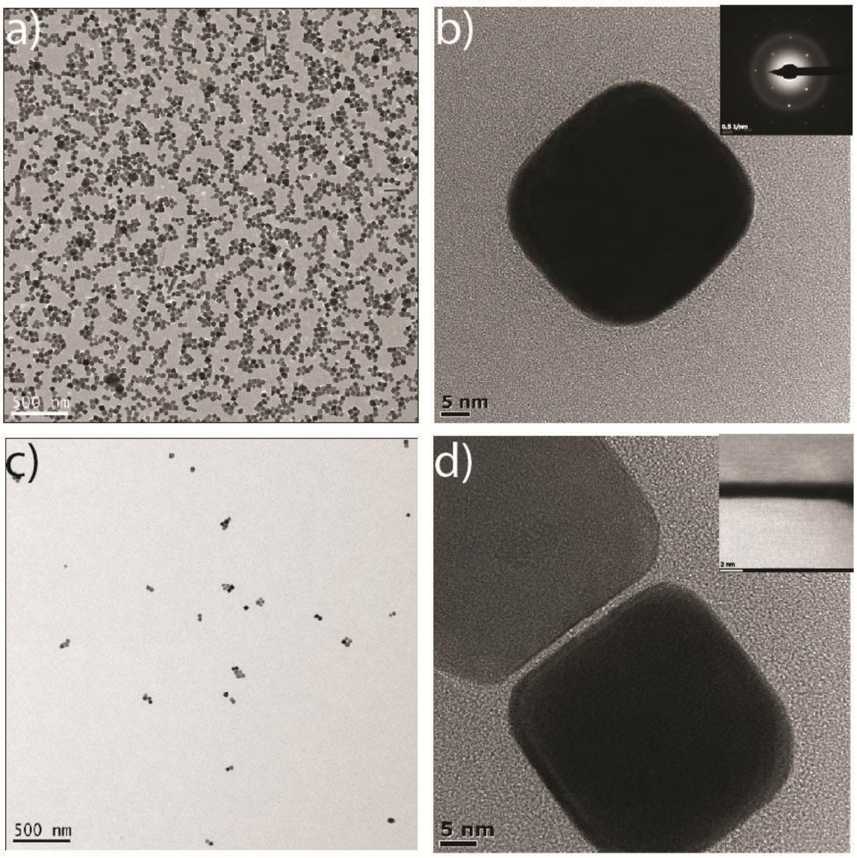

Figure 3.2 (a) TEM overview image of chemically-synthesized silver nanocubes. (b) TEM image and electron diffraction pattern of a single silver nanocube (inset). (c) Representative TEM overview image of the Ag nanocubes after functionalization with mixed SAMs of PT and BDT. (d) Dimer consisting of two silver nanocubes aligned parallel to each other and a high resolution scanning TEM image (STEM) of the gap region (inset).

To constitute the very small gaps, we performed a functionalization process to the Ag nanocubes with mixed self-assembled monolayers (SAMs) of alkanethiols and alkane/benzenedithiols with different chain lengths so that the silver-thiolate bonds would reduce the size of the nanogaps to sub-nm length scale. We define the nanogap as the distance between two silver nanocubes surfaces where they are parallel aligned. The length of EDT, HDT, ODT, BDT, BPDT, OPV and NDT are 0.44 nm, 0.93 nm, 1.17 nm, 0.63 nm, 1.03 nm, 1.24 nm and 0.88 nm, respectively (determined using Chem 3D ultra

10.0; see Figure 3.3 for the molecular structures).[11] These values are generated from the built-in parameters on bond lengths, bond angles and dihedral angles without further optimization procedures. Figure 3.3 shows that the gap sizes indeed were controlled by the molecular structure. The histograms we obtained for the nanogap sizes (d_g) show reasonable agreement where the maximum of the Gaussian peak lies at 0.6 ± 0.1 nm for EDT, 0.7 ± 0.1 nm for HDT and BDT, 1.0 ± 0.2 nm for ODT, 1.2 ± 0.2 nm for BPDT and OPV, 1.0 ± 0.3 nm for NDT and very close to the estimated molecular lengths (d_l).

For the structures self-assembled with these mixed SAMs, we observed a significant number of dimers where each particle was covered with a SAM, resulting in a value of d that is roughly double of that expected for a junction with only a single SAM. The second peak in these histograms is attributed to dimers with SAMs on both nanoparticles (Ag-SAM//SAM-Ag structures). Double peaks are not observed for SAMs of 1,4-biphenyldithiol (BPDT), 4,4-dimercaptostilbene (OPV) and 1,5-napthalenedithiol (NDT). These three SAMs contain biphenyl moiety which had been proven in literature[12] to result in a molecular dipole moment that affects the adsorption kinetics on metal surfaces. Unlike the SAMs of alkanethiolates in which the packing is driven by the interchain Van der Waals attraction, biphenyl derivative molecules possess a strong dipole moment, resulting in intermolecular repulsion and instability. Thus, double layers of SAMs are not observed in Figure 3.3 (e-g). Figure 3.4 also shows that our experimentally measured gap sizes (aliphatic molecules: black solid squares; aromatic molecules: red solid squares) are in good correlation with the molecular length predicted by a Corey-Pauling-Koltun (CPK) model (red and black dotted lines).

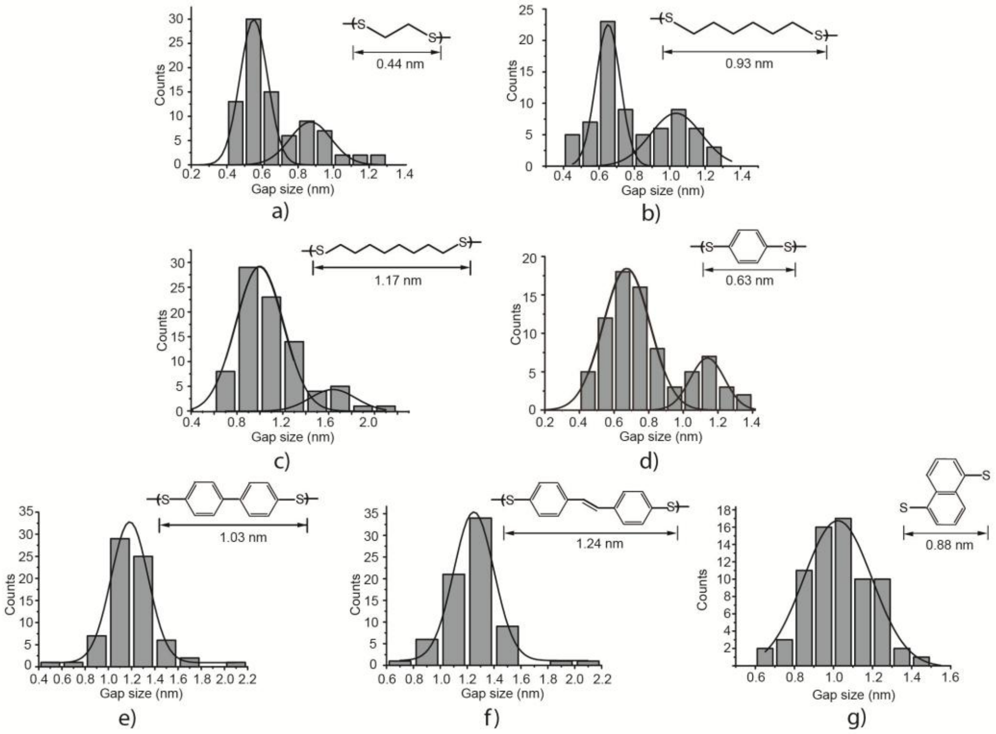

Figure 3.3 (a) Histograms of the gap sizes between two silver nanocubes with Gaussian fits to these histograms functionalized with mixed SAMs of 1-propanethiol and 1,2-ethanedithiol (EDT) (b) with mixed SAMs of 1-heptanethiol and 1,6-hexanedithiol (HDT) (c) with mixed SAMs of 1-nonanethiol and 1,8-octanedithiol (ODT) (d) with mixed SAMs of 1-propanethiol and 1,4-benzenedithiol (BDT) (e) with SAMs of 1,4-biphenyldithiol (BPDT) (f) with SAMs of 4,4-dimercaptostilbene (OPV) (g) with SAMs of 1,5-napthalenedithiol (NDT).

Table 3.1 Summary of Figure 3.3: Number of junctions, interparticle spacing of silver nanocubes assembled with linkers of different molecular length d_l estimated by a CPK model and the gap sizes d_g determined experimentally from TEM images.

Linker	Number of Junctions	Molecular Length (nm), d_l	Gap Size (nm), d_g
1,2-ethanedithiol (EDT)	84	0.44	0.55 ± 0.08
1,6-hexanedithiol (HDT)	73	0.93	0.65 ± 0.11
1,8-octanedithiol (ODT)	85	1.17	1.00 ± 0.23
1,4-benzendithiol (BDT)	79	0.63	0.67 ± 0.12
1,5-dimercaptonapthalene (NDT)	73	0.88	1.02 ± 0.35
1,4-biphenyldithiol (BPDT)	73	1.03	1.18 ± 0.23
4,4-dimercaptostilbene (OPV)	76	1.24	1.24 ± 0.21

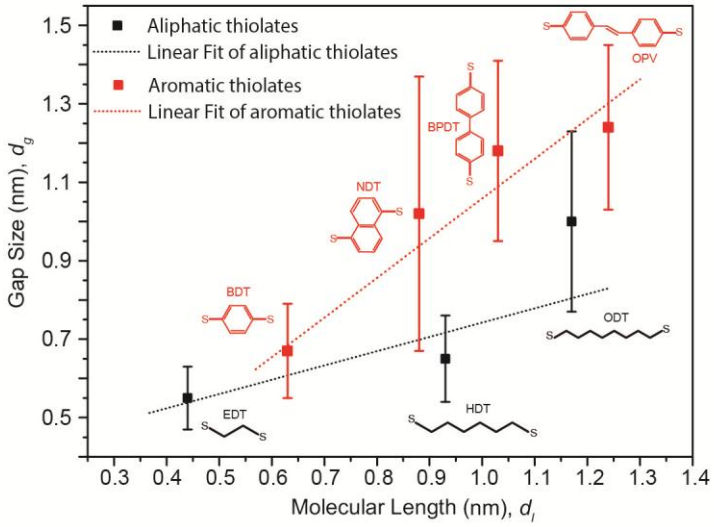

Figure 3.4 Experimentally measured gap sizes versus molecular lengths as predicted by the CPK model.

3.2.3. 3D Scanning TEM Tomography

To further characterize the high aspect ratio nano-gaps, 3D scanning TEM (STEM) tomography was conducted to obtain a 3-dimensional view of these nanogaps. We functionalized the silver nanocubes with ODT (procedure as shown in the experimental section) and dropcasted ~3µl of the final solution onto a Si_3N_4 substrate (30 nm thick, from Agar Scientific). The substrate with nanocube dimers was tilted from -50° to 50° with respect to the horizontal axis of the nanocubes dimer and a STEM image was taken at intervals of 1-3°. The series of images were aligned and a 3D volume was reconstructed from a total of 55 STEM images, as shown in Figure 3.5. Due to the lack of projections from the high tilt angle ranges (beyond ± 70°), we suffered from the missing wedge effect[13] which give rises to the volume artifacts that are indicated by the white arrow in Figure 3.5 (c). Nonetheless, the reconstructed 3D volume showed clearly that the gap between the cubes is free of metal filaments.

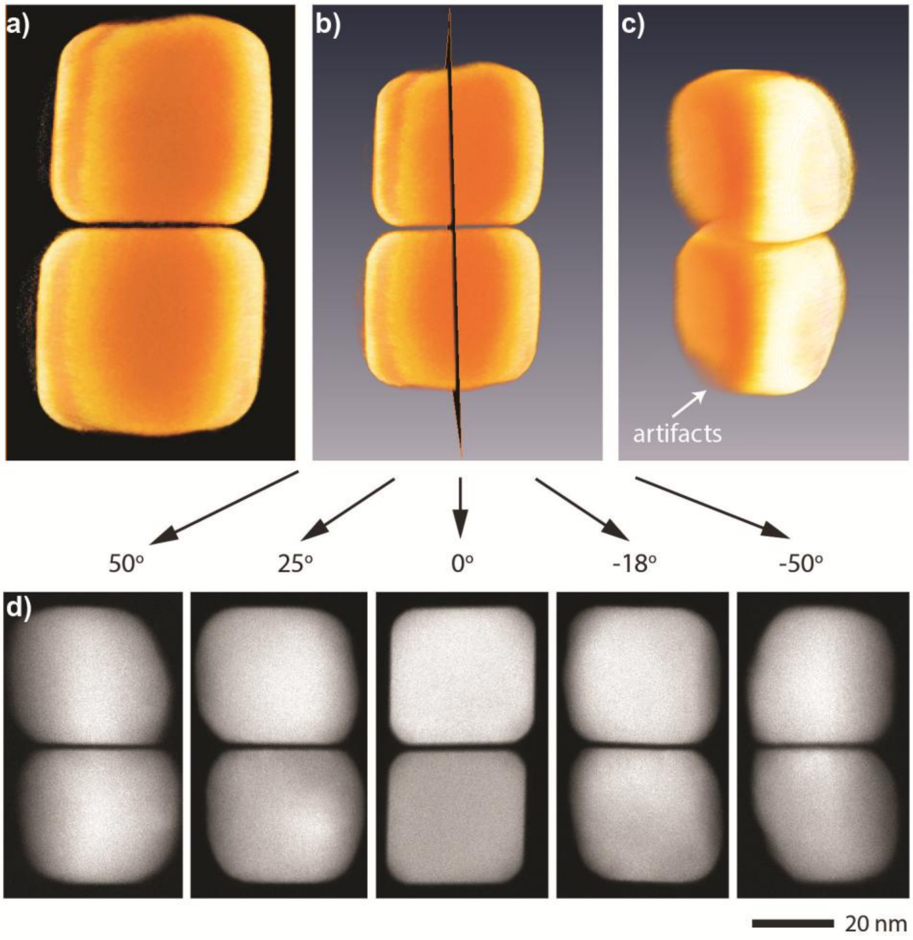

Figure 3.5 HAADF-STEM tomography images of a dimer of Ag nanocube where the sample was tilted from -50° to 50°. (a) A reconstructed x-y slice extracted from the 3D volume in (c).

(b) The combination of both. (d) Reconstructed STEM images at different dimer tilts, looking parallel to the gap.

3.2.4. UV-Visible (UV-Vis) Spectroscopy

The energy and intensity of the absorption peaks in UV-Vis spectra of plasmonic particles are dependent on the size, shape, and on the dielectric constants of both the metal and surrounding medium.[14] A well-dispersed sample of our silver nanocubes shows a distinct absorption peak at 429 nm (λ_1) which is same as reported in literature.[10] This peak is equivalent to ~3 eV which is assigned to the plasmon mode of transverse charge oscillation between the cuboid corners. Figure 3.6 (a) and (c) show the absorption spectra changes of silver nanocubes before and after addition of mixed SAMs in ethanol for EDT and BDT, respectively. For systems, upon the addition of mixed SAMs, the peak at 429 nm (I) shifted to the ~440 nm (II) and further shifted to ~450 nm (VIII) within 60 minutes. This is due to the change in dielectric constant of the particle environment compared to the PVP coating.[15] The absorbance value dropped significantly after washing with ethanol (IX) and the newly formed broad band around 550 nm is prominent after washing with EtOH. After addition of non-functionalized nanocubes, the absorbance value of this newly formed band ~ 550 nm (λ_2) gradually increases with time. Nanocube assemblies of different lengths exhibit different spectral maxima, but we could only observe a collective response in a broader absorption, without any dominant peak for the EDT system (Figure 3.6 b).[16]

For BDT system, a relatively strong extinction was observed for the band (λ_2) at ~550 nm (Figure 3.6 d). This peak is equivalent to ~2 eV, which is the longitudinal plasmon mode. We attributed this observation to the stronger π-π interaction between the rigid benzene rings than intercalating alkyl chains and $\pi\rightarrow\pi^*$ transitions which results in more linear assemblies than is the case with aliphatic SAMs. Linear dimers and oligomers showed much more pronounced differences in mode energies compared to non-linear arrays.[17] Figure 3.6 (e) and (f) show the absorption spectra of silver nanocubes before and after addition of different SAMs for 60 minutes and the addition of non-functionalized particles after 60 minutes respectively. From these observations we derive three conclusions. (i) Overall, the redshift of the peak at 429 nm (λ_1) after the addition of SAMs is due to the change in dielectric constant of the environment compared to the PVP coating. (ii) The new peak or band (λ_2) appearing at ~550 nm corresponds to the formation of assemblies after the addition of non-functionalized particles. (iii) The band was not obvious for long alkyl chain assemblies such as HDT and ODT which could be due to the intercalating alkyl chains resulting in severe aggregation.

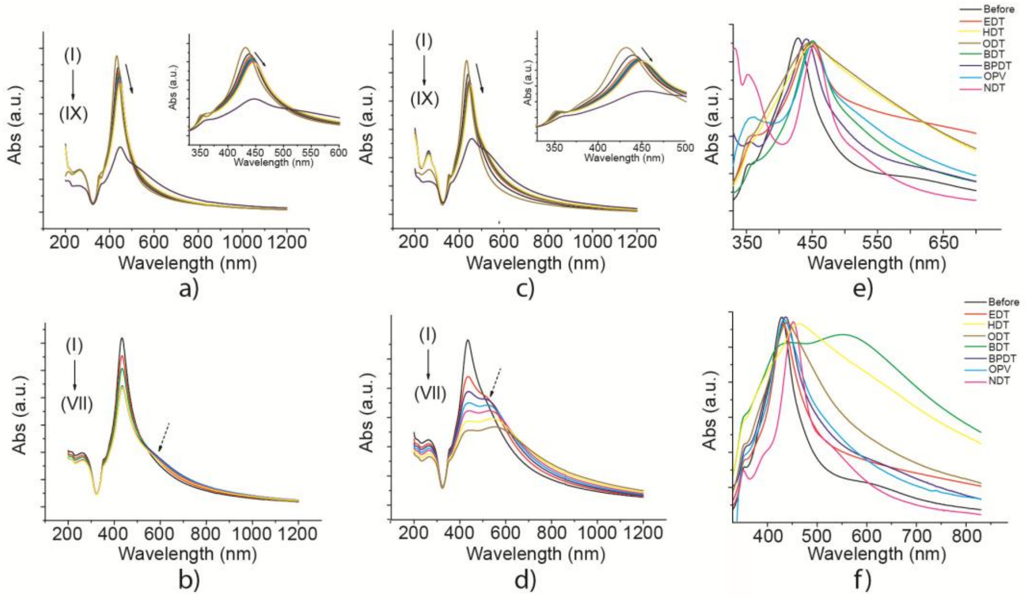

Figure 3.6 (a) UV-Vis spectra of silver nanocubes functionalized with mixed SAMs of 1-propanethiol and 1,2-ethanedithiol or (c)1,4-benzenedithiol: (I) Ag cubes before addition of mixed SAMs, (II) 0 minute upon addition of mixed SAMs, (III) 10 minutes after addition of mixed SAMs, (IV-VIII) each spectrum was recorded in the interval of 10 minutes, (IX) Ag nanocubes after addition of mixed SAMs after 60 minutes and washed with EtOH. (inset) Close up of Figure (a) at 330-500 nm. (b) and (d) UV-Vis spectra of functionalized silver nanocubes with addition of non-functionalized silver nanocubes for both EDT and BDT system respectively: (I) Ag nanocubes after addition of mixed SAMs after 60 minutes and washed with EtOH. (II) 0 minute upon addition of non-functionalized silver nanocubes, (III) 10 minutes after addition of non-functionalized silver nanocubes, (IV-VIII) each spectrum was recorded in the interval of 10 minutes. (e) UV-Vis spectra of different SAMs coated silver nanocubes after 60 minutes. (f) UV-Vis spectra of different SAMs coated silver nanocubes after addition of non-functionalized particles after 60 minutes.

Table 3.2 Summary of Figure 3.6: The wavelength shift between two plasmon resonance modes after the addition of SAMs and subsequent addition of non-functionalized particles for each linker.

Linker	Molecular Length (nm), d_l	After addition of SAMs		After addition of non-functionalized Ag nanocubes	
		λ_1 (nm)	$\Delta\lambda=\lambda_1-\lambda_{before}$ (nm)	λ_2 (nm)	$\Delta\lambda=\lambda_2-\lambda_1$ (nm)
Before	NA	429	NA	NA	NA
1,2-ethanedithiol (EDT)	0.44	447	18	432	-15
1,6-hexanedithiol (HDT)	0.93	452	23	464	12
1,8-octanedithiol (ODT)	1.17	447	18	440	-7
1,4-benzenedithiol (BDT)	0.63	451	22	434	-17
1,4-biphenyldithiol (BPDT)	0.88	442	13	437	-5
4,4-dimercaptostilbene (OPV)	1.03	452	23	434	-18
1,5-dimercaptonapthalene (NDT)	1.24	454	25	452	-2

3.2.5. X-Ray and UV Photoelectron Spectroscopy (XPS and UPS)

The XPS S_{2p} spectra in Figure 3.7 (a) show that there was no sulfur signal for silver nanocubes before functionalization. After addition of mixed SAMs, silver nanocubes were bonded with mixed SAMs through silver-thiolate bonds. The two doublet peaks at 162 eV (S1) and 163 eV (S2) were assigned to sulfur bound to the silver nanocubes[18-20] and free thiol groups respectively.[21-22] The relative intensities of S1 and S2 were summarized in Table 3.3.

On the other hand, we attributed the peak at 168 eV for BDT functionalized silver nanocubes to the presence of oxidized thiols/dithiols molecules. The N_{1s} spectra in Figure 3.7 (b) also show that the nitrogen signal at 399 eV for silver nanocubes after functionalization was significantly lower than before functionalization. The nitrogen signal originated from the polyvinylpyrrolidone (PVP), the polymer used during synthesis of silver nanocubes. From the relative intensities as shown in Table 3.3, the N_{1s} signal was significantly lowered by 50.6-99.3% after functionalization. This indicates that the PVP is being replaced by the SAMs. These findings further justify the role of SAMs in controlling the gap sizes between silver nanocubes.

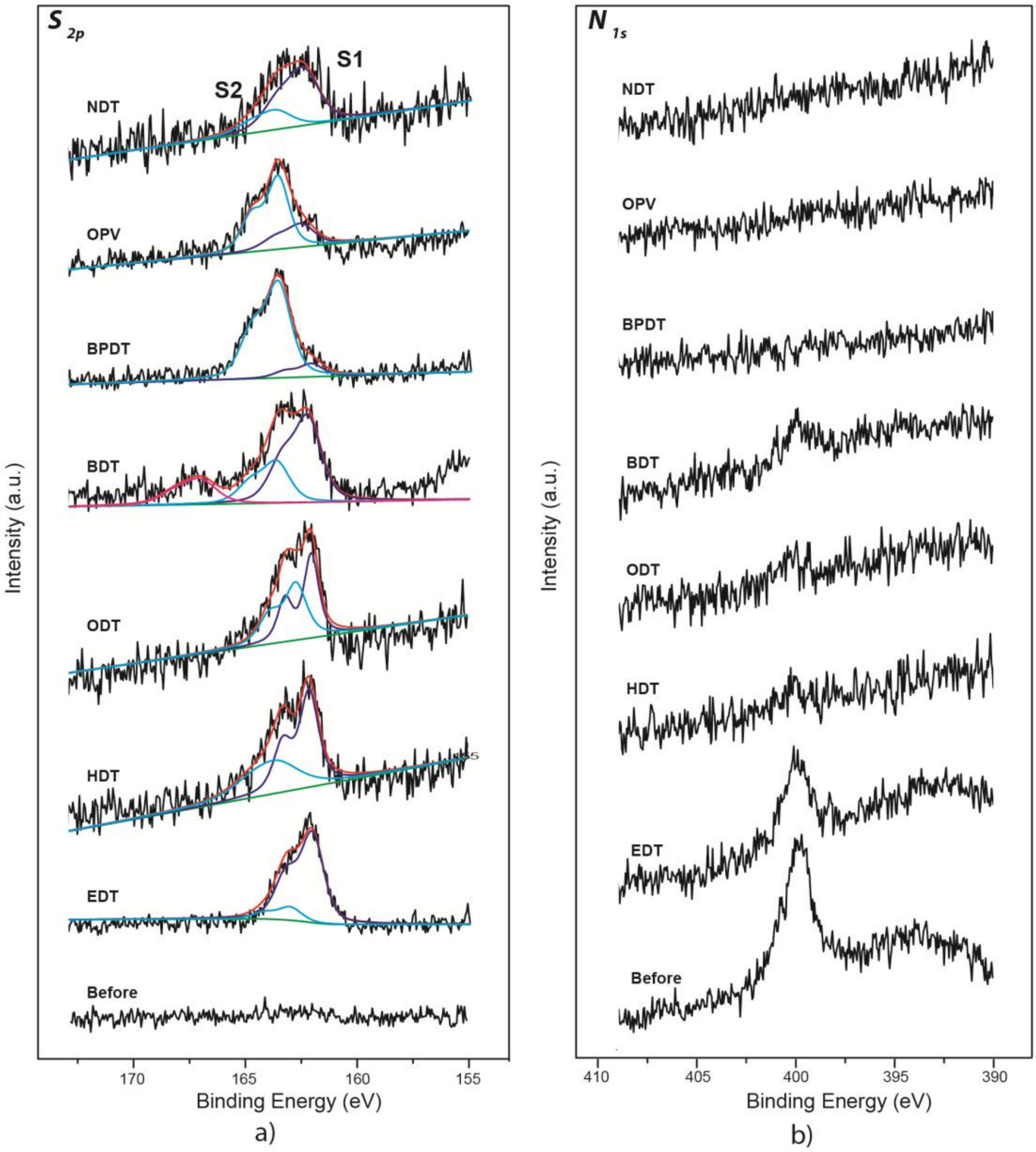

Figure 3.7 (a) and (b) XPS spectra (S_{2p} and N_{1s} region) of silver nanocubes before (bottom) and after addition of mixed SAMs of thiolates and dithiolates (EDT, HDT, ODT and BDT) or SAMs of dithiolates only (BPDT, OPV, and NDT).

Table 3.3 Summary of Figure 3.7: Relative intensities of peak S1 and S2 for S_{2p} signal and N_{1s} from XPS spectra for each type of junction with different linkers.

Linker	S_{2p}		N_{1s}
	S_1 (%)	S_2 (%)	Relative peak area intensity (%)
before	NA	NA	100
1,2-ethanedithiol (EDT)	87.1	12.9	49.4
1,6-hexanedithiol (HDT)	59.7	40.3	2.3
1,8-octanedithiol (ODT)	51.0	49.0	7.2
1,4-benzendithiol (BDT)	67.2	32.8	20.3
1,5-dimercaptonapthalene (NDT)	73.8	26.2	5.4
1,4-biphenyldithiol (BPDT)	11.4	88.6	0.7
4,4-dimercaptostilbene (OPV)	27.9	72.1	7.7

Figure 3.8 (a) shows the UPS spectra for Ag nanocubes functionalized with different SAMs. From the UPS data, we obtained the energy difference between the HOMO onset of the molecule to the Fermi onset of the metal; the data are listed in Table 3.4. The values of the HOMO-LUMO energy gaps were obtained from those reported in the literature.[23-27] By having these two values, we could construct our proposed energy level diagram as shown in Figure 3.8 (b-h). The barrier height for junctions bridged by conjugated molecules such as BDT and OPV is lower than those of long and non-conjugated molecules such as EDT. Therefore, by changing the molecule inside the junction, we could not only alter the gap dimension, but also the electronic properties of the junctions. With this, we show the molecular control over the barrier height of the studied system.

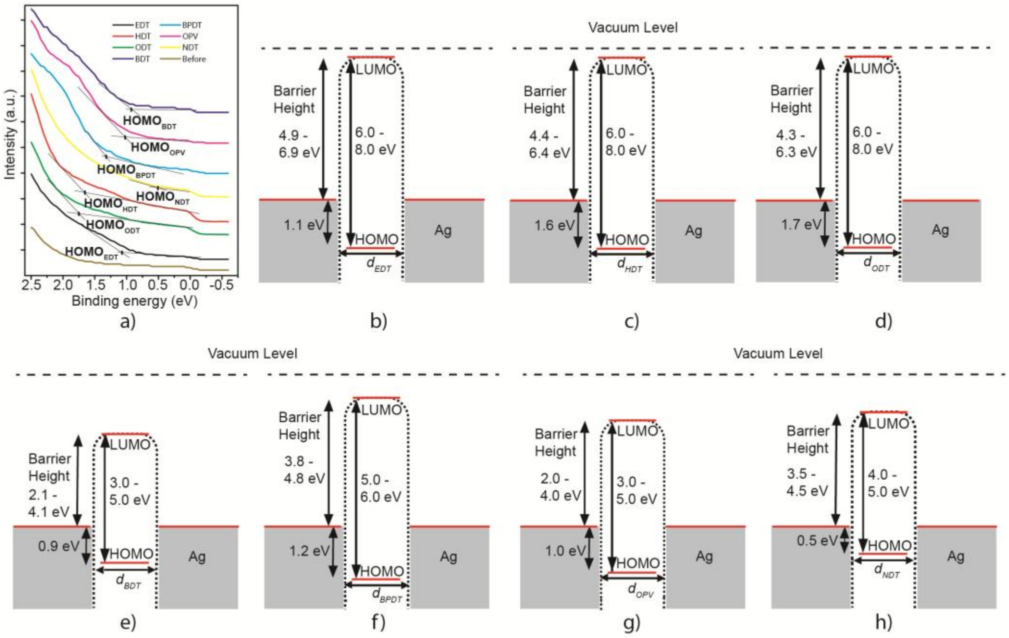

Figure 3.8 (a) UPS spectra for Ag nanocubes functionalized with mixed SAMs of thiolates and dithiolates (EDT and BDT) or SAMs of dithiolates only (BPDT, OPV, and NDT). (b)-(h) are the illustration of energy diagram for all systems.

Table 3.4 Summary of Figure 3.8: HOMO onset values, HOMO-LUMO energy gap values obtained from literature and the estimated barrier height values for each type of junctions with different linkers.

Linker	HOMO Onset (eV)	HOMO-LUMO Gap, E_{HL} (eV)	Barrier Height, Φ (eV)
1,2-ethanedithiol (EDT)	1.1	7.0 ± 1.0	4.9 ± 1.0
1,6-hexanedithiol (HDT)	1.6	7.0 ± 1.0	4.4 ± 1.0
1,8-octanedithiol (ODT)	1.7	7.0 ± 1.0	4.3 ± 1.0
1,4-benzendithiol (BDT)	0.9	4.0 ± 1.0	3.1 ± 1.0
1,5-dimercaptonapthalene (NDT)	0.5	4.5 ± 0.5	4.0 ± 0.5
1,4-biphenyldithiol (BPDT)	1.2	5.5 ± 0.5	4.3 ± 0.5
4,4-dimercaptostilbene (OPV)	1.0	4.0 ± 1.0	3.0 ± 1.0

3.3. Conclusions

We have demonstrated the use of self-assembled monolayers (SAMs) of molecules to selectively control the gap sizes between two nanostructures down to sub-nanometer scales through self-assembly, assisted by the covalent bonding of anchored sulfur groups. Our experimental approach will be beneficial for connecting nanomaterials into desired arrays and thereby tuning the plasmonic and optoelectronic properties of the nanomaterials which will be important for the future design of plasmonic structures and the development in SERS experiments.

3.4. Experimental Section

3.4.1. General Procedures. The chemicals: poly (vinyl) pyrrolidone, silver nitrate, 1,2-ethanedithiol (EDT), 1,6-hexanedithiol (HDT), 1,8-octanedithiol (ODT), 1,4-benzenedithiol (BDT), biphenyl-4,4'-dithiol (BPDT), and 4,4-dimercaptostilbene (OPV) were all purchased from Sigma-Aldrich. 1,5-dimercaptonapthalene (NDT) was purchased from Tokyo Chemical Company. Sodium sulfide and ethylene glycol were purchased from J.T. Baker. The glass vials used for synthesis were from Fisher Scientific. Chemicals were used without further purification. Solvents for nanoparticles functionalization were freshly distilled prior to use. All stirrer bars were soaked in aqua-regia (mixture of 3:1 volume ratio of nitric acid: hydrochloric acid) for at least 1 hour, washed with deionized water (18.2 MΩ.cm) and dried in oven before use. The centrifuges, used for washing nanoparticles, were Rotina (380R) and Profuge (14D). The Transmission Electron Microscopy (TEM) images are recorded on an FEI Titan TEM and a JEOL 2010FEG TEM.

3.4.2. Synthesis of Silver Nanocuboids. The polyol method developed by the Xia's group[10] was used to chemically synthesize the single-crystalline silver nanocubes. 5 ml of ethylene glycol (EG) were injected into each of the four glass vials labeled A, B, C, and D. Then, the stirrer bars were inserted into each vials and pre-heated at 150°C in an oil bath for at least one hour. Then, 70, 80, 90 and 100 μl of sodium sulfide solution (30 mM, Na_2S in EG) were added into the glass vials A, B, C, D respectively. After 8-9 mins, 1.5 ml of polyvinylpyrridone solution (0.02 g/ml PVP in EG) and 0.5 ml of silver nitrate solution (0.048 g/ml $AgNO_3$ in EG) were added sequentially. The reaction was quenched by removing the glass vials from the oil bath and to place it in an ice water bath once the color of the reaction mixture turned ochre-green. This reaction is highly sensitive to water and the concentration of sodium sulfide and that usually only one out of the four glass vials showed the expected color changes. This reaction was completed within 20 minutes. Once the reaction mixture is cooled to room temperature, the Ag nanocubes solution was washed by centrifugation at 2200 rpm (Rotina, 380R) for 30 minutes with 25 ml of acetone (AR grade). The supernatant was discarded and the nanoparticles washed two times by redispersing them in 2 ml of deionized (DI) water followed by centrifugation (Profuge, 14D) at 10000 rpm for 10 minutes. Finally, the Ag nanocubes solution was transfered into clean glass vials and dispersed them in 4 ml of DI water. The Ag nanocubes solution was wrapped with aluminium foils, sealed with parafilm and kept in dark. Under these conditions, the solutions were stable for two weeks.

3.4.3. Functionalization of Silver Nanocubes with Mixed SAMs. 0.1 ml of Ag nanocubes solution was transfered from the glass vial above into a

1.5 ml-centrifuge tube. Centrifugation and redispersion in water was done twice (Profuge, 14D) at 10000 rpm for 10 minutes in order to minimise the concentration of PVP and EG prior to functionalization with mixed self-assembled monolayers (SAMs). Note that too many times of washing (centrifuge and redisperse) will cause the deformation of Ag cubes. Specifically, 5.0 µl of 1-propanethiol ethanolic solution ($1x10^{-3}$ M) and 3.0 µl of 1,2-ethanedithiol ethanolic solution ($1x10^{-3}$ M) were added into 2.36 ml of distilled ethanol. Subsequently, 36 µl of 6-8 nM Ag nanocubes solution was added into the mixture and stirred for 60 mins. The reaction mixture was centrifuged with distilled ethanol twice (Profuge, 14D) at 10000 rpm for 10 minutes and re-dispersed in the same solvent. Subsequently, an additional 36 µl of as-prepared non-functionalized Ag nanocubes solution was added quickly into the mixture and incubated for another 60 mins. The same procedure was followed for different chain length of thiols and dithiols: 1-heptanethiol and 1,6-hexanedithiol (HDT), 1-nonanethiol and 1,8-octanedithiol (ODT), 1-propanethiol and 1,4-benzenedithiol (BDT). For longer molecules such as biphenyl-4,4'-dithiol (BPDT), 4,4-dimercaptostilbene (OPV) and 1,5-dimercaptonapthalene (NDT), due to their poor solubility in ethanol and binding kinetics, merely dithiol molecules were used instead of mixed SAM of thiols and dithiols. Other than that, the same procedure was repeated for longer molecules except BPDT and OPV solutions, which were prepared in tetrahydrofuran (THF) solvent before adding them into the reaction mixture.

3.4.4. Experimental Techniques. The functionalization process is monitored by UV/VIS/NIR spectroscopy (PerkinElmer Lambda 750). Light transmission was measured through a cuvette of 1 cm light-path. The resulting suspensions ~100 µl of each were spin-coated onto 30 nm-thick gold substrates for XPS characterization. The surface analysis system used for XPS characterization was VG ESCALAB Mark 2. It is equipped with an Omicron (EA125 U7) hemispherical electron spectrometer with 7 channel detection, emission angle of 15 deg, maximum entrance and exit slits. A pass energy of 20 eV was used with a FWHM of 1.0 eV. The X-ray gun used was Omicron Twin Anode X-ray Mg/Al source. Monochromatic Mg K (alpha) radiation at power of 300W (15kV x 30mA) was used for excitation. The peaks fitting were done by using the software of XPSPEAK version of 4.1. Characterization of the nanogap sizes and 3D scanning TEM tomography were done with a high-resolution FEI Titan TEM, operated at 200 kV where typically 3 µl of the final suspension was dropcasted onto the silicon nitride membrane (30 nm-thick, S1N1 Agar Scientific**)**. Gap size measurement was performed on every single TEM image of individual dimer pairs and clusters of particles using the profile function in Gatan software Digital Micrograph version 1.4. The gap size was defined as the interface between two metal surfaces aligned parallel to each other. The histogram in Figure 3.3 was constructed over 80-100 gap sizes each. The Gaussian peaks fitting were done by using Origin software version 7. The 3D volumes shown in Figure 3.5 were constructed by using the software Inspect3D.

3.5. References

1. Savage, K. J.; Hawkeye, M. M.; Esteban, R.; Borisov, A. G.; Aizpurua, J.; Baumberg, J. J., Revealing the quantum regime in tunnelling plasmonics. *Nature* **2012,** *491* (7425), 574-577.

2. Scholl, J. A.; García-Etxarri, A.; Koh, A. L.; Dionne, J. A., Observation of Quantum Tunneling between Two Plasmonic Nanoparticles. *Nano Letters* **2012,** *13* (2), 564-569.

3. Tan, S. F.; Wu, L.; Yang, J. K. W.; Bai, P.; Bosman, M.; Nijhuis, C. A., Quantum Plasmon Resonances Controlled by Molecular Tunnel Junctions. *Science* **2014,** *343* (6178), 1496-1499.

4. Camargo, P. H. C.; Rycenga, M.; Au, L.; Xia, Y., Isolating and Probing the Hot Spot Formed between Two Silver Nanocubes. *Angewandte Chemie International Edition* **2009,** *48* (12), 2180-2184.

5. Li, W.; Camargo, P. H. C.; Au, L.; Zhang, Q.; Rycenga, M.; Xia, Y., Etching and Dimerization: A Simple and Versatile Route to Dimers of Silver Nanospheres with a Range of Sizes. *Angewandte Chemie International Edition* **2010,** *49* (1), 164-168.

6. Broers, A. N.; Molzen, W. W.; Cuomo, J. J.; Wittels, N. D., Electron‐beam fabrication of 80‐Å metal structures. *Applied Physics Letters* **1976,** *29* (9), 596-598.

7. Cord, B.; Yang, J.; Duan, H.; Joy, D. C.; Klingfus, J.; Berggren, K. K., Limiting factors in sub-10nm scanning-electron-beam lithography. *Journal of Vacuum Science & Technology B* **2009,** *27* (6), 2616-2621.

8. Ou, F. S.; Hu, M.; Naumov, I.; Kim, A.; Wu, W.; Bratkovsky, A. M.; Li, X.; Williams, R. S.; Li, Z., Hot-Spot Engineering in Polygonal Nanofinger Assemblies for Surface Enhanced Raman Spectroscopy. *Nano Letters* **2011,** *11* (6), 2538-2542.

9. Bosman, M.; Zhang, L.; Duan, H.; Tan, S. F.; Nijhuis, C. A.; Qiu, C. W.; Yang, J. K. W., Encapsulated Annealing: Enhancing the Plasmon Quality Factor in Lithographically–Defined Nanostructures. *Scientific Reports.* **2014,** *4*.

10. Skrabalak, S. E.; Au, L.; Li, X.; Xia, Y., Facile synthesis of Ag nanocubes and Au nanocages. *Nature Protocols* **2007,** *2* (9), 2182-2190.

11. Mills, N., ChemDraw Ultra 10.0 CambridgeSoft, 100 CambridgePark Drive, Cambridge, MA 02140. www.cambridgesoft.com. Commercial Price: $1910 for download, $2150 for CD-ROM; Academic Price: $710 for download, $800 for CD-ROM. *Journal of the American Chemical Society* **2006,** *128* (41), 13649-13650.

12. Ulman, A.; Kang, J. F.; Shnidman, Y.; Liao, S.; Jordan, R.; Choi, G.-Y.; Zaccaro, J.; Myerson, A. S.; Rafailovich, M.; Sokolov, J.; Fleischer, C., Self-assembled monolayers of rigid thiols. *Reviews in Molecular Biotechnology* **2000,** *74* (3), 175-188.

13. Lin, M.; Tan, H. R.; Tan, J. P. Y.; Boothroyd, C.; Foo, Y. L.; He, C. B., Transmission Electron Microscope Tomography of Nanostructured Materials. *Journal of Nanoengineering and Nanomanufacturing* **2011,** *1* (3), 257-264.

14. Eustis, S.; El-Sayed, M. A., Why gold nanoparticles are more precious than pretty gold: Noble metal surface plasmon resonance and its enhancement of the radiative and nonradiative properties of nanocrystals of different shapes. *Chemical Society Reviews* **2006,** *35* (3), 209-217.

15. Moran, C. H.; Rycenga, M.; Zhang, Q.; Xia, Y., Replacement of Poly(vinyl pyrrolidone) by Thiols: A Systematic Study of Ag Nanocube Functionalization by Surface-Enhanced Raman Scattering. *The Journal of Physical Chemistry C* **2011,** *115* (44), 21852-21857.

16. Thomas, K. G.; Barazzouk, S.; Ipe, B. I.; Joseph, S. T. S.; Kamat, P. V., Uniaxial Plasmon Coupling through Longitudinal Self-Assembly of Gold Nanorods. *The Journal of Physical Chemistry B* **2004,** *108* (35), 13066-13068.

17. Quinten, M.; Kreibig, U., Optical properties of aggregates of small metal particles. *Surface Science* **1986,** *172* (3), 557-577.

18. Laibinis, P. E.; Whitesides, G. M.; Allara, D. L.; Tao, Y. T.; Parikh, A. N.; Nuzzo, R. G., Comparison of the structures and wetting properties of self-assembled monolayers of n-alkanethiols on the coinage metal surfaces, copper, silver, and gold. *Journal of the American Chemical Society* **1991,** *113* (19), 7152-7167.

19. Heister, K.; Zharnikov, M.; Grunze, M.; Johansson, L. S. O.; Ulman, A., Characterization of X-ray Induced Damage in Alkanethiolate Monolayers by High-Resolution Photoelectron Spectroscopy. *Langmuir* **2001,** *17* (1), 8-11.

20. Himmelhaus, M.; Gauss, I.; Buck, M.; Eisert, F.; Wöll, C.; Grunze, M., Adsorption of docosanethiol from solution on polycrystalline silver surfaces: an XPS and NEXAFS study1. *Journal of Electron Spectroscopy and Related Phenomena* **1998,** *92* (1–3), 139-149.

21. Full length article. *Surface Science* **1998,** *405* (1), L472-L476.

22. George, G. A., High resolution XPS of organic polymers—the scienta ESCA 300 data base. G. Beamson and D. Briggs. John Wiley & Sons, Ltd, Chichester, 1992. Pp. 295, price £65.00. ISBN 0-471-93592-1. *Polymer International* **1994,** *33* (4), 439-440.

23. Strange, M.; Rostgaard, C.; Häkkinen, H.; Thygesen, K. S., Self-consistent GW calculations of electronic transport in thiol- and amine-linked molecular junctions. *Physical Review B* **2011,** *83* (11), 115108.

24. Reddy, P.; Jang, S.-Y.; Segalman, R. A.; Majumdar, A., Thermoelectricity in Molecular Junctions. *Science* **2007,** *315* (5818), 1568-1571.

25. Xiao; Xu; Tao, N. J., Measurement of Single Molecule Conductance: Benzenedithiol and Benzenedimethanethiol. *Nano Letters* **2004,** *4* (2), 267-271.

26. Scheer, A. M.; Gallup, G. A.; Burrow, P. D., Unoccupied orbital energies of 1,4-benzenedithiol and the HOMO–LUMO gap. *Chemical Physics Letters* **2008,** *466* (4–6), 131-135.

27. Wold, D. J.; Frisbie, C. D., Formation of Metal−Molecule−Metal Tunnel Junctions: Microcontacts to Alkanethiol Monolayers with a Conducting AFM Tip. *Journal of the American Chemical Society* **2000,** *122* (12), 2970-2971.

Chapter 4

Quantum Plasmon Resonances controlled by Molecular Tunnel Junction

Abstract: *Quantum tunneling between two plasmonic resonators links nonlinear quantum optics with terahertz nanoelectronics. Direct observation of and control over quantum plasmon resonances at length scales in the range 0.4 to 1.3 nanometers across molecular tunnel junctions made of two plasmonic resonators bridged by self-assembled monolayers (SAMs) were demonstrated. The tunnel barrier width and height are controlled by the properties of the molecules. Using electron energy-loss spectroscopy, a plasmon mode, the tunneling charge transfer plasmon, whose frequency (ranging from 140 to 245 terahertz) is dependent on the molecules bridging the gap was observed.*

4.1. Introduction

Quantum mechanical effects in plasmonic structures are believed to become important when two plasmonic resonators are placed so closely that electrons can tunnel across the gap.[1-11] Direct experimental access to the resulting tunneling charge transfer plasmon (tCTP) mode is expected to open up new opportunities in, for instance, nano-scale opto-electronics, single molecule sensing, and non-linear optics.[1]

Generally, two types of CTP (Figure 4.1) have been investigated so far: (1) CTP via conduction and (2) CTP via tunnelling (tCTP). The former has been well-studied by Duan *et al*.[11] The low- energy CTP via conduction peak between two gold polycrystalline nanoprisms showed a red-shift in energy loss as a function of the bridge width. However, when the bridge was replaced by a gap of 0.5 nm, the low-energy peak disappeared.

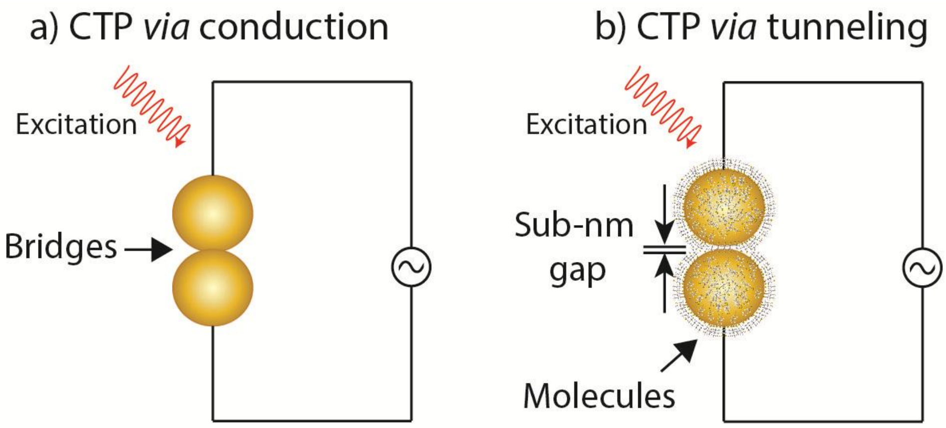

Figure 4.1 Schematic illustration of quantum tunnelling assisted electrical circuits facilitated by (a) conductive bridges and (b) sub-nanometer gap.

Experimental and theoretical studies so far have concluded that quantum mechanical effects i.e.: the observation of the tCTP mode are important only at length scales below 0.3 to 0.5 nm, close to the bond length of gold and silver.[6, 9-11] Such structures are technologically inaccessible and therefore it is important to demonstrate the tCTP mode across gaps larger than a nanometer that can be fabricated by state-of-the-art fabrication techniques.[11]

Unlike past works that investigated tunneling through vacuum,[6, 10] we placed molecules in the gap because tunneling rates across molecules depend on the molecular structure and are much higher than across vacuum.

Routine experimental tunnel junctions on molecular monolayer (Figure 4.2) has been proven that the low tunnelling decay coefficient of the molecules will give rise to the high tunnelling rates across the junctions. This approach made it possible to directly observe and control tCTPs experimentally in tunneling gaps up to at least 1.3 nm, depending on the type of molecules bridging the gap, and moves quantum plasmonics into the size domain that is accessible via bottom-up or top-down fabrication methods.[11]

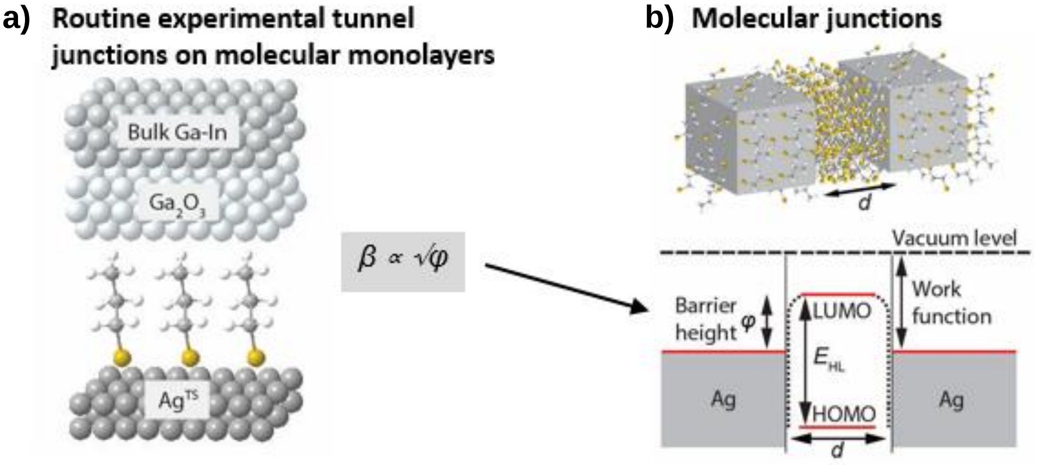

Figure 4.2 (a) Routine experimental tunnel junctions on molecular monolayers. (b) Schematic illustration of the molecular tunnel junctions made of two silver nanoparticles bridged by SAMs and a schematic energy-level diagram of the junctions.

Quantum effects have been observed only indirectly as shifts in the bonding dipolar resonance plasmon mode.[1, 6, 10] Our aim was to perform an experiment where the presence of a tunneling barrier can be directly imaged, while the tCTP mode is simultaneously measured spectroscopically. In this Chapter, we study the molecular electronic control over the tCTP mode.

4.2. Results & Discussion

4.2.1. Synthesis and Functionalization of Silver Nanocubes

Refer to the Chapter 3 Section 3.2.2. The experimental details of the synthetic procedures and characterization techniques are reported in the experimental section at end of this chapter. Here, we only give a brief description.

We introduced two experimental innovations: (1) the cross-sectional area of the tunnel junction was increased from a few nm^2 to roughly 10^3 nm^2 and (2) the tunneling rate across the nano-gaps was increased by tunneling through molecules rather than vacuum.

Cuboidal silver nanoparticles were used[12] separated by SAMs with thicknesses of 0.5 – 0.6 nm forming metal-SAM-metal junction via self-assembly (Figure 4.3 a). The facets of the nanoparticles are atomically flat, which results in a very large cross-sectional area of around 10^3 nm^2, maximizing the number of tunneling events across the junctions. The silver nanoparticles were functionalized with either saturated, aliphatic 1,2-ethanedithiolates (EDT), or aromatic 1,4-benzenedithiolates (BDT).[13] The lengths of EDT and BDT are similar, but they have very different HOMO-LUMO gaps of 8 and 5 eV, respectively.[14-16] Therefore, the tunneling rates across junctions with BDT molecules are higher than those junctions with EDT. The interaction between the two nanoparticles was optimized to avoid aggregation or misalignment by diluting the dithiols with 1-propanethiol

(PT).[13] After self-assembly of the dimeric structures, they were deposited on a 30 nm thick, electron-transparent silicon nitride membrane.

A simplified form of the Simmons equation (Eq. 1) is commonly used to approximate molecular tunnel junctions[17-18]

$$J = J_0 e^{-\beta d} \text{ with } \beta = 2\sqrt{\frac{2m\varphi}{\hbar^2}}, \qquad (1)$$

where β (Å^{-1}) is the tunneling decay coefficient, d (nm) is the width of the tunneling barrier, and the pre-exponential factor J_0 (A/cm^2) is the hypothetical current when d = 0; m is the mass of the charge carrier (kg), and $\hbar$ is the reduced Plank's constant. The value of β depends on the barrier height φ (eV). Tunneling rates through molecular bonds, so-called through-bond tunneling, are much higher ($\beta \approx 0.8 - 0.9$ Å^{-1} for saturated molecules and $0.1 - 0.3$ Å^{-1} for unsaturated molecules) than through vacuum ($\beta = 2.9$ Å^{-1}).[19] Figure 4.2 (b) shows the energy level diagram of the metal-SAM-metal junctions schematically. As indicated in Figure 4.2 (b), in molecular electronics d is defined by the length of the molecule, d_l (nm), and φ by the offset between the Fermi-levels of the metal and the energy level of the molecular frontier orbitals. In contrast, when the through-space tunneling is the dominant mechanism of charge transport, the barrier height equals the work function of the electrode materials and d equals the gap, d_g (nm), between the two electrodes, i.e., the distance between the nanoparticles.[20]

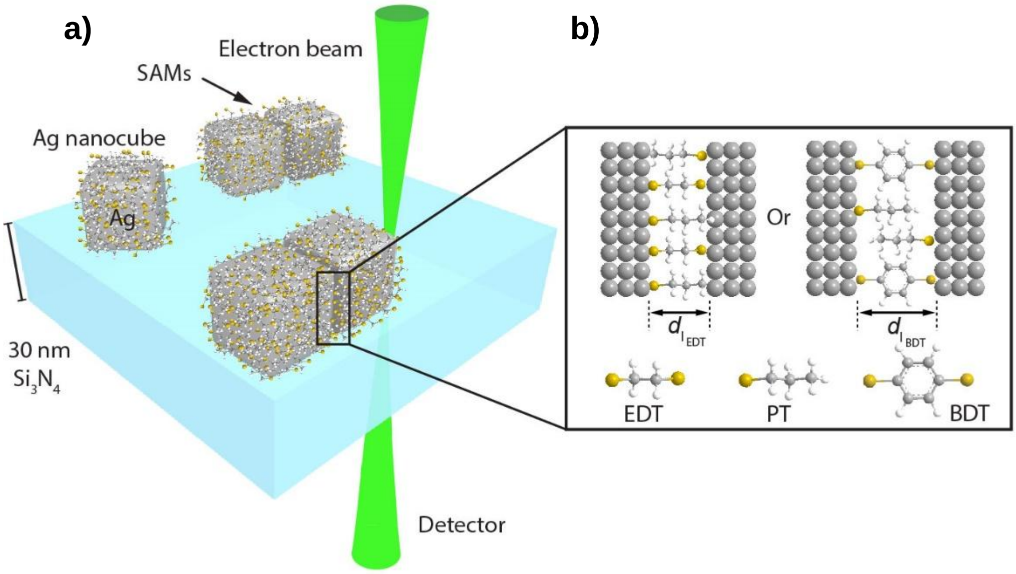

Figure 4.3 Quantum plasmonic tunnel junctions. (a) Schematic illustration of the molecular tunnel junctions made of two silver nanoparticles bridged by a SAM on an electron-transparent silicon nitride membrane. The contactless electron nano-probe was placed near the functionalized silver nanoparticles to excite and measure the surface plasmons of individual dimers. (b) The distance between two adjacent nanoparticles is determined by the thickness of the SAMs of EDT or BDT.

4.2.2. Electron Energy-Loss Spectroscopy (EELS)

Instead of bringing the dimer particles in contact with electrical probes that will perturb the plasmon resonances, we used in our experiment a focused beam of energetic electrons in a scanning transmission electron microscope (STEM) as a contactless nanoprobe to excite and analyze the surface plasmon resonances in individual dimers. We positioned the electron probe opposite the gap at the long axis of a silver particle dimer, as illustrated in Figure 4.3 (a), to excite longitudinal plasmon modes—similar to lateral plane wave illumination of the dimer.[13] During the plasmon excitation, the tunnel junction was therefore not exposed to the electron beam to minimize irradiation damage.[13]

The excitation of plasmon resonances results in an energy transfer from the electron beam to the particle system, which we analyzed with monochromated electron energy-loss spectroscopy (EELS).[21-23] The junctions were imaged before and after acquiring the EELS spectra to ensure that none of these junctions formed conductive metal filaments during the experiment.[13] Thus, in all of our experiments we could discriminate between the tunneling and conduction through metal filaments – CTP modes conclusively.

4.2.3. Molecular Control over the Gap Sizes

Figure 4.4 (a) shows the representative TEM overview image after the functionalization process. From these images, it can be seen that dimers, as well as single particles and larger clusters are present on our samples. Figure 4.4 (c) shows atomic-resolution TEM images of a silver nanoparticle dimer. The first peak in the histograms of values of d_g estimated from TEM images on a series of dimers are centred at 0.55 ± 0.08 nm for EDT (Figure d) and 0.67 ± 0.12 nm for BDT (Figure e) which are close to d_l as expected for Ag-SAM-Ag structures. The second peak in these histograms is attributed to dimers with SAMs on both nanoparticles (Ag-SAM//SAM-Ag structures). Intercalating SAMs or not completely removed polymer that was used in the nanoparticle synthesis may result in smaller and larger gap sizes than expected from the molecular lengths, as indicated schematically in Figure 4.8 (a).

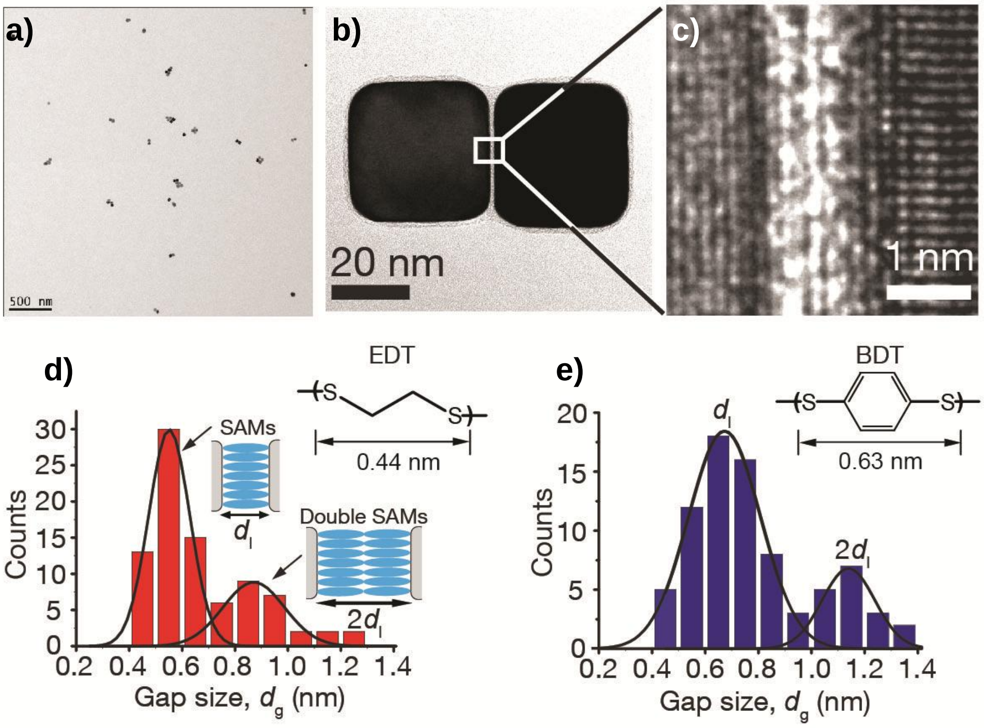

Figure 4.4 (a) Representative TEM overview image of the Ag nanocubes after functionalization with mixed SAMs of PT and BDT. (b) High resolution TEM image of a dimer with 0.8 nm separation. (c) Atomic resolution TEM image of the high aspect ratio gap (0.8 × 30 × 30 nm^3). Histogram of gap sizes for (d) EDT and (e) BDT molecular junctions.

4.2.4. Molecular Control over the Barrier Heights

From the UPS data, we obtained the energy difference between HOMO onset of the molecule to the Fermi onset of the metal. The HOMO onset values were determined by linear extrapolation of the lower binding energy side of the HOMO peak intercepted with the linear extrapolation of the base line as denoted by the black lines and solid vertical bars in Fig. 4.5 (a).[24] The value of HOMO-LUMO energy gap were obtained from those reported in single-molecule spectroscopy.[25-29] By having these two values, we could construct our proposed energy level diagram as shown in Figure 4.5 (b). Barrier height for junctions bridged by conjugated molecules such as BDT is lower than the non-conjugated molecules such as EDT by 2.7 eV. By changing the molecule inside the junction, we could not only alter the gap dimension, but also the electronic properties of the junctions. With this, we show the molecular control over the barrier height of the studied system.

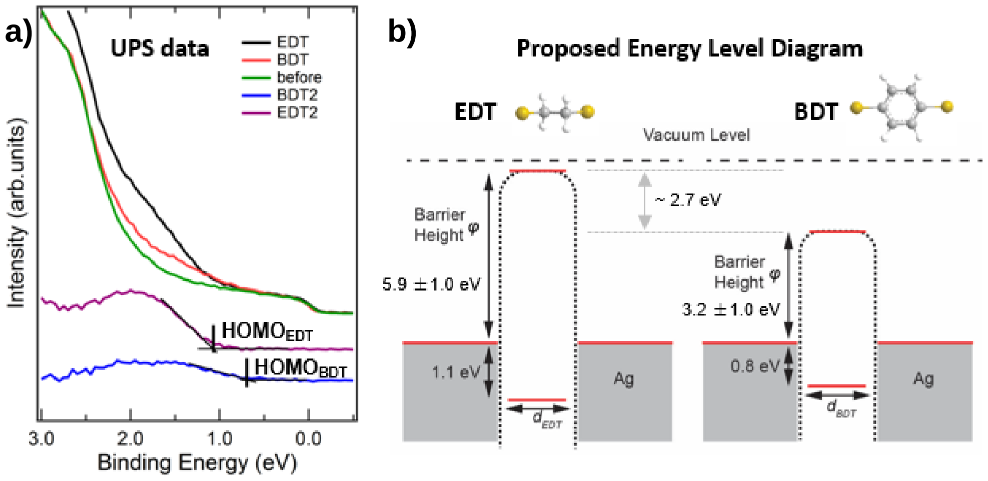

Figure 4.5 (a) UPS spectra for Ag nanocubes functionalized with mixed SAMs of thiolates and dithiolates (EDT and BDT) (b) Proposed energy level diagram for the EDT and BDT system.

4.2.5. Experimental Evidence of Tunneling CTP Peak

Figure 4.6 (a) and (b) show EELS spectra recorded from junctions with SAMs of EDT and BDT. Three main plasmon peaks were observed around 2.2 eV, 3.2 eV and 3.6 eV, which we assigned to the bonding dipolar plasmon mode (II), the transverse corner mode (III), and the transverse edge mode (IV), respectively, in agreement with the finite-element-model (FEM) simulations (Figure 4.6 c).[13, 20] A new low-energy plasmon mode is observed at 0.60 ± 0.04 eV for EDT and 1.01 ± 0.01 eV for BDT.

We assigned this plasmon mode to the tCTP based on our calculations that show the transfer of net charge between the cuboids (Figure 4.6 c, mode I). The plasmon resonances of the Ag-SAM-Ag system were simulated using a quantum-corrected FEM optical simulation model.[13, 20] Briefly, the optical properties of the junctions are calculated through a quantum mechanical approach and then used to simulate the plasmon resonances of the Ag-SAM-Ag system. The model predicts that the tCTP mode strongly depends on φ, d, and gap field, E_{gap} (V/m). The value of φ is modeled analytically as $\varphi = \alpha\, E_{HL}$, where $0 < \alpha < 1$ relates to the energy-level alignment, and E_{HL} is the HOMO-LUMO gap, which was obtained from single molecule experiments.[14-16] We assume $E_{gap} = 7\times10^8$ V/m throughout the calculations based on previously-reported work.[13, 20]

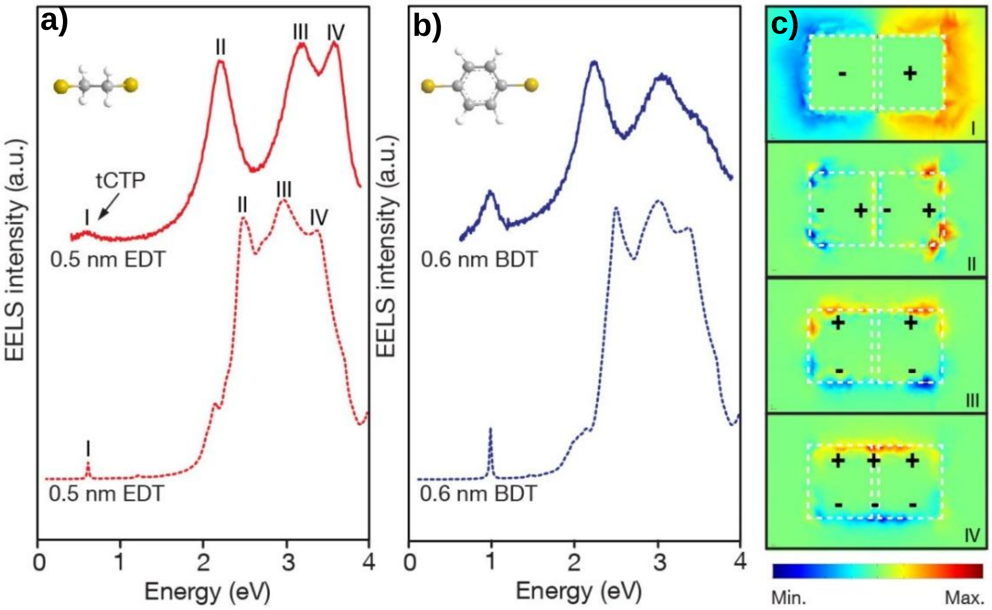

Figure 4.6 Direct observation of quantum tunneling between plasmon resonators. Two examples of measured EELS spectra with the occurrence of quantum tunneling directly observed via the tCTP peak and quantum-corrected simulations of the extinction spectra, confirming the identification of the peaks. Experimentally measured EELS spectra (solid line) and theoretical calculated spectra (dotted line) for dimers functionalized with (a) EDT and (b)

BDT respectively. (c) Simulated maps of the electrical-field distributions for the plasmon modes I-IV, corresponding with the spectral peaks.

4.2.6. Through Bond versus Through Space Tunneling

There are two possible tunneling processes in our molecular tunnel junction: (1) through-space tunneling and (2) through-bond tunneling. For junctions with either tilted SAMs or well-aligned SAMs (Figure 4.7) both types of mechanisms may apply. In through-space tunneling, the tunneling path is defined by the gap size d_g between the two electrodes; and for through-bond tunneling, the electrons will tunnel through the molecule with the tunneling path defined by the molecular length $d_{l.}$ In case that through-bond tunneling dominates over through-space tunneling, we expect the tCTP to be only dependent on d_l and not on d_g.

In calculating through-space tunneling process, the gap size d_g was used, which is defined by the distance between the two electrodes. For different dimers with the same monolayer SAM, although the SAMs are the same length, the measured d_g could be different due to the orientation of SAMs (Figure 4.7 and 4.4 d and 4.8 a). In the calculations, the measured gap sizes are used. On the other hand, for the through-bond tunneling process, the molecular length defines the tunnel length, so we used d_l for all the monolayer samples in the quantum-tunneling calculations. It should be noted that our model is a simplified physical model, which does not consider any microscopic details of the SAM. These effects can for example be taken into consideration by changing the barrier height $\varphi = \alpha\ E_{HL}$. To take into the account the molecular orientations, the barrier height φ (or the energy alignment parameter α) is varied: φ = 3.3 – 3.5 eV for EDT and φ = 1.0 – 1.5 eV for BDT. The exact values of barrier height inside the molecular junction will likely be smaller than the one measured by UPS[30] due to the charge renormalization of the energy levels.[31-33] This is induced by charges on the molecule and the corresponding image charges in the metal surfaces during charge transport. Thus, the values we used for calculation are smaller than the one measured in UPS but the exact factor is still unknown.

In addition to the two possible tunneling mechanisms, if by any chance our SAM layer is damaged or ionized during our experiment, we may have the third possibility: ionic conduction and/or hopping (which are slow relative to optical time scales). If this is the case, the conductivity of SAM will be (nearly) independent of spacing (either d_g or d_l). The nature of the charge transport—through-space or through-bond tunneling—was determined from EELS measurements on 32 junctions, for which the energy of the tCTP mode was plotted as a function of d_g (Figure 4.7 c). This graph shows that the tCTP depends only weakly on the value of d_g. The dotted lines in Figure 4.5 (c) show simulations of the tCTP energy shifts if through-space tunneling would dominate, with $d = d_g$.[13] The solid lines are simulations for through-bond tunneling with $d = d_l$, where the through-bond tunneling distance depends on the length of the molecule and can be different from d_g when the molecules are not perfectly aligned in the gap. Figure 4.7 (c) shows that through-bond tunneling has a much weaker dependence on gap size than through-space tunneling. The good agreement with the experimental results indicates that coherent through-bond tunneling is the dominant mechanism of charge transport.[13]

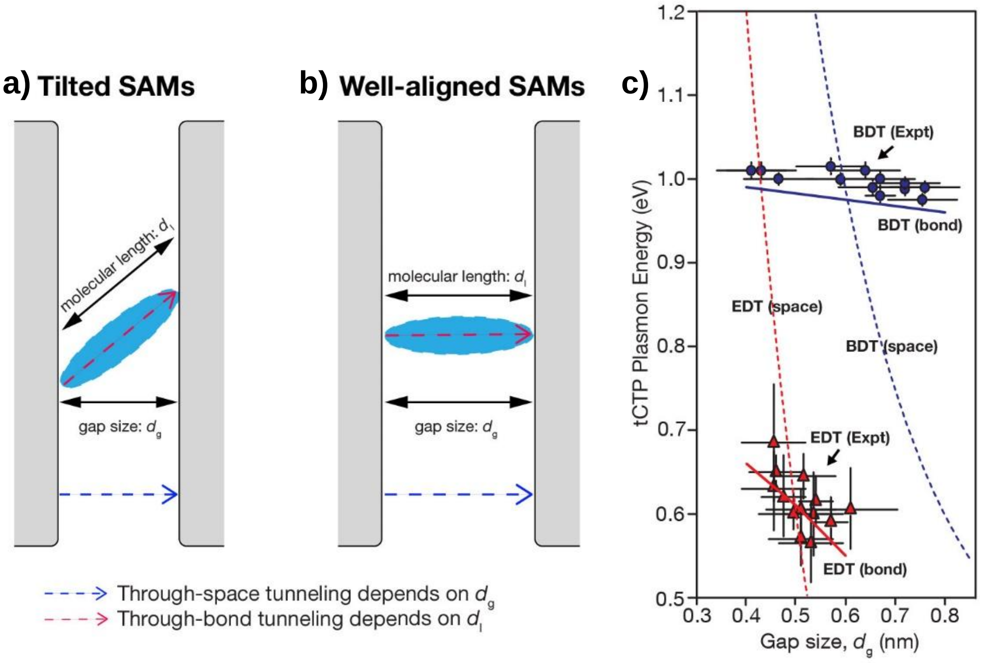

Figure 4.7 Schematic of molecular orientation in the dimer gap, and its effect on the tunneling process.(a) Tilted SAMs and (b) Well-aligned SAMs. (c) Experimentally measured plasmon energy as a function of gap size for dimers functionalized with monomers of BDT (●) and EDT (▲). Theoretical calculations for through-space and through-bond tunneling are shown as dotted lines and solid lines respectively for the two SAMs.

4.2.7. Tunneling is Possible for Gap Size > 1 nm

Through-bond tunneling could allow us to explore tCTP across a large gap as the tunneling is less dependent on the gap size. EELS spectra were recorded on Ag-SAM//SAM-Ag junctions to study whether the tCTP mode could be observed over larger length scales up to 1.3 nm. Figure 4.8 shows that a tCTP mode for the structures with BDT appears at 0.975-1.015 eV. The tCTP peak energy only weakly depends on d_g, which confirms that though-bond tunneling is the dominant mechanism of charge transport. The marginal difference in energy of the tCTP mode for single and double SAMs is likely due to strong π–π coupling between the BDT SAMs.[34] For Ag-SAM//SAM-

Ag structures with EDT, the tCTP mode was not observed because of the low β value and that no π–π coupling occurs between aliphatic molecules, we expected its peak—if any—to be at very low energies beyond the detection limit of our instrument.

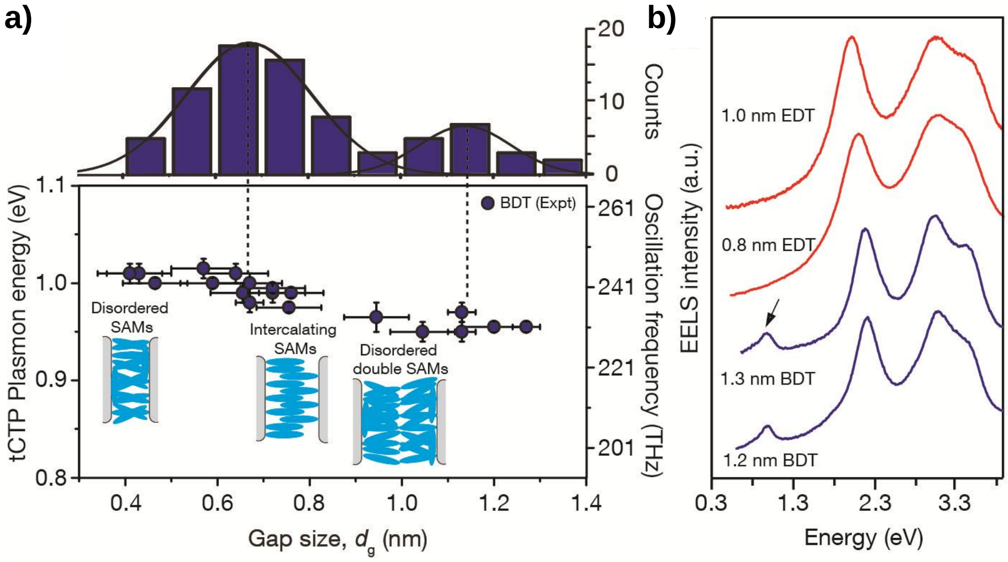

Figure 4.8 Quantum plasmon resonances as a function of tunneling distance. (a) Experimentally measured plasmon energy as a function of gap size for BDT- (●) functionalized dimers. The gap size varies between individual dimers because of structural disorder in the SAMs. (b) Measured EELS spectra for double SAMs of EDT (red) and BDT (blue). Tunneling was observed for the double layer BDT but not in the double layer EDT.

4.3. Conclusions

By combining atomic-resolution imaging, single-particle spectroscopy, and monolayer molecular control, we have demonstrated quantum-mechanical electron tunneling at optical frequencies between plasmon resonators. By varying the self-assembled molecular monolayers in the junctions, the plasmon-induced tunneling frequencies could be controlled from 1.01 ± 0.01 eV, or 244 ± 3 THz, for a monolayer of BDT molecules, to 0.60 ± 0.04 eV, or 145 ± 10 THz, for a monolayer of EDT molecules. The mechanism of charge transport was coherent through-bond tunneling which is only weakly dependent on the gap size. The relatively large distance of up to 1.3 nm over which the tunneling takes place in Ag-BDT//BDT-Ag junctions, may provide potential for molecular control over quantum plasmonic systems through longer molecules to perhaps 4-5 nm,[35] i.e., gap sizes that are currently accessible by top-down fabrication techniques. Our results show that tunneling can reconcile molecular electronics with plasmonics, opening up a whole new, interdisciplinary field of exploration.

4.4. Experimental Section

4.4.1. General Procedures. For the silver nanocuboids, the chemicals polyvinylpyrridone, silver nitrate, 1,2-ethanedithiol, 1,4-benzenedithiol were all purchased from Sigma-Aldrich and used without further purification. Sodium sulfide and ethylene glycol were purchased from J.T. Baker. For the gold nanocuboids, the chemicals 1-butanethiol, 1,3-propanedithiol, gold (ш) chloride trihydrate, sodium borohydride, cetyltrimethylammonium bromide, copper sulfate, L-ascorbic acid were all purchased from Sigma-Aldrich and used without further purification. The glass vials used for synthesis were obtained from Fisher Scientific. Solvents for nanoparticles functionalization were freshly distilled prior to use. All stirrer bars were soaked in aqua-regia (mixture of 1:3 volume ratio of nitric acid: hydrochloric acid) for at least 1 hour, washed with deionized water (18.2 Ωcm) and dried in an oven before use. Nanoparticles were washed in Rotina (model 380R) and Profuge (model 14D) centrifuges.

4.4.2. Synthesis of Silver Nanocubes.

Refer to Chapter 3 Section 3.4.

4.4.3. Functionalization of Silver Nanocubes with Mixed SAMs.

Refer to Chapter 3 Section 3.4.

4.4.4. EELS Measurements. Plasmon characterization on individual pairs of Ag nanocuboids is carried out in scanning TEM (STEM) mode using an FEI Titan TEM with Schottky electron source, operated at 80 kV. The diameter of the used electron probe is about 1 nm, and a 13 mrad convergence semiangle was used. For EELS spectroscopy, electrons within a solid semiangle of 13 mrad were collected, using a Gatan Tridiem ER EELS detector. It is worth noting here that during the EELS measurements, the STEM probe was positioned outside the tunnel junction. The SAMs were therefore not exposed to the electron beam when the spectra were acquired. This proved critical, as we also tried EELS mapping, but here the whole dimer had to be irradiated during the acquisition, including the tunnel junction. The long (minutes) total exposure of the SAMs during these mapping attempts proved too destructive and the tCTP mode disappeared. For tCTP measurements, it is therefore important to minimize the electron beam exposure of the SAMs, as we did during our EELS measurements without irradiating the dimer gaps.

A Wien-type monochromator dispersed the electron beam in energy, and a narrow energy-selecting slit formed a monochrome electron beam with typical full-width at half-maximum values of 70-80 meV. EELS spectra were acquired with a modified binned gain averaging routine.[22] Each individual spectrum was acquired fast, with illumination periods around 40 ms, using 16 times on-chip binning for detector CCD readout. Spectra shown are typically summations of 2000 individual, aligned spectra. The spectra were all normalized at their maximum, the top of the zero-loss peak. All spectra were acquired 1-2 nm off the edge on the long dimer axis. The background signal was corrected by fitting and subtracting a high-quality background spectrum that was measured at a clean area of the same sample without particles nearby.

4.4.5. Simulation Methods. The simulation work is developed in collaboration with Dr. Wu Lin and Dr. Bai Ping from Institute of High Performance Computing (IHPC). A quantum-corrected finite-element-method (FEM) optical simulation model[9, 20] is employed to study the plasmon resonances of the Ag-SAM-Ag system. The quantum-tunneling process in the molecular tunnel junction is modeled by first determining the tunneling barrier profile of the Ag-SAM-Ag[20] via: (1) the intrinsic barrier height φ at the interface of Ag and SAM, (2) the image charge potential, which is gap size d_g dependent and is essential for the sub-nanometer gaps, (3) the electric field E_{gap} in the gap (4), the tunneling electron self-induced space charge field, and (5) the quantum exchange-correlation field. Then the Schrödinger equation and the Poisson equation are solved iteratively using a WKB-type approximation technique for the tunneling barrier profile and the tunneling electron density (n) which can be used to obtain the optical conductivity of the tunneling junction $\sigma(\omega)$.[20]

The difference here for our Ag-SAM-Ag system is the intrinsic barrier height φ, which is no longer the work function of the Ag electrode. Instead, the barrier height φ is the energy level alignment of the molecular frontier orbitals of the SAMs and the Fermi-levels of the Ag electrode, which is rather difficult to predict theoretically. We used a simple formula to model the intrinsic barrier height $\varphi = \alpha E_{\mathrm{HL}}$ (where $0 < \alpha < 1$), which is determined by two factors. The first is the type of SAM in the tunneling junction, which is modeled by E_{HL} (i.e., the energy difference between HOMO and LUMO). The values of E_{HL} used in our calculation are obtained by single molecule experiments[14-16, 19] and *ab initio* calculations.[36] The second factor is the energy level alignment of the molecular frontier orbitals with respect to the Fermi-levels of the Ag electrode, which is modeled by α with $0 < \alpha < 1$. Simply changing the parameter α allows us to study the effect of the energy alignment on the plasmonic response. The value of α used in the calculations is determined by experimental results, for example, $\alpha = 0.425$ for EDT and $\alpha = 0.25$ for BDT.

The gap field E_{gap} at the Ag/SAM interface generated during the EELS excitation is difficult to be obtained experimentally. To find the E_{gap}, we first conducted theoretical calculations using our previously published method[20] and found that the E_{gap} is ~7×10^8 V/m for the Ag/EDT/Ag system to excite a tCTP mode at 0.6eV. To further confirm the calculation result, we estimated the average field in the SAM layer with a capacitance model based on our

EELS measurements. The capacitance of a gap is defined as $C = \varepsilon_r \varepsilon_0 \frac{A}{d_g}$, where A is the area of overlap of the two plates, ε_r is the relative static permittivity of the material between the plates, ε_0 is the electric constant ($\varepsilon_0 \approx 8.854\times10^{-12}$ Fm^{-1}), and d_{g} is the separation between the plates. Taking the energy stored in the capacitor is the plasmon energy E_{plasmon}, then $E_{plasmon} = \frac{1}{2}CV^2$, where V gives the voltage between the plates. Therefore the average field in the gap is $\bar{E}_{gap} = \frac{V}{d_g} = \sqrt{\frac{2E_{plasmon}}{d_g A \varepsilon_r \varepsilon_0}}$. For the case of EDT [$\varepsilon_r$ = $(1.558)^2$], a gap size of 0.5 nm and cross sectional area of 37×37 nm^2, the CTP plasmon energy is about 0.6 eV. This gives an average field of 1.142×10^8 V/m. The field distribution within the SAM layer shows a non-uniform profile which has the strongest field at the edge of Ag/SAM. It is this edge field at the interface of Ag/SAM that plays the major role in the tunneling process. Taking into account the fact that edge field is much larger than the average field, the theoretically estimated gap field E_{gap} = 7×10^8 V/m. This value of E_{gap} was then used throughout the calculations to predict the trends in the frequency of tCTP peak as a function of d_{g}, d_{l}, and the tunnel barrier height, (as shown in Figure 4.7 and 4.8) which are in excellent agreement with the experimental results.

After obtaining the optical properties of the molecular tunnel junction, the plasmon resonances of the Ag-SAM-Ag system can be simulated from classical electromagnetic calculations, more specifically, a finite-element-method (FEM) optical simulation model is used. Here the two identical Ag cuboids are assumed to have a square cross section with side length w = 37 nm, and the length of each Ag cuboid is L = 35 nm based on the TEM images. The Ag's dielectric function is taken from Palik's handbook.[37] Between the two Ag cuboids, a tunneling path (filled with the tunneling electrons) is assumed to have a square cross section with area A = 37 × 37 nm^2, and the length of the tunneling path is determined either by the gap size d_g or the molecular length d_l (discussed in next section). This tunneling path is modeled using $\varepsilon(\omega) = 1 + i\frac{\sigma(\omega)}{\omega\varepsilon_0}$ as described above. In addition, to account for the fact that species may be added during our experiment, each Ag cuboid is assumed to be coated with a 0.5-nm-thick self-assembled monolayer (SAM), with a refractive index of 1.558 (EDT) or 1.665 (BDT).[38] For simplicity, the 30 nm Si_3N_4 substrate is neglected in our optical simulations. As the effect of the thin substrate is small for low-energy plasmon modes, this simplification has little effects on the simulations of the low-energy tCTP mode.[39]

Scattered-field formulation in COMSOL finite element method is used to solve the three-dimensional Maxwell's equations. The spectra of absorption, scattering and their sum (i.e., extinction) cross sections of the Ag-SAM-Ag system can be calculated. Simulations are performed using plane-wave excitation for two polarization conditions: the incident light is polarized along the longitudinal axis (i.e., long axis) or along the transverse axis (i.e., short axis). Longitudinal and transverse mode components (dash lines in Figure 4.9) are obtained separately. The final simulated extinction spectrum (the black solid line in Figure 4.9) to be compared with EELS measurement is an algebraic summation of the longitudinal and transverse mode components. This is based on arbitrary mixing because the exact ratio of Ex and Ey component is unknown. In this case, same magnitude of Ex and Ey are assumed.

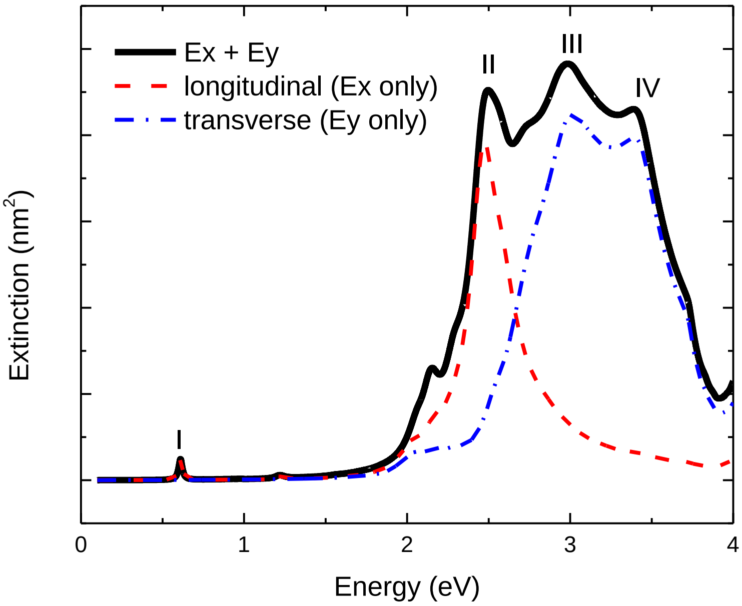

Figure 4.9 Simulated EELS spectra for an Ag-EDT-Ag dimer system under longitudinal polarization (in the dimer's length direction; red dashed line), or transverse polarization (perpendicular to the dimer's length axis; blue dash-dotted line), and their summation (black line).

As shown in Figure 4.7, our quantum corrected classical model indeed fits our experimental data well. This good agreement makes it possible to estimate the molecular conductance of individual EDT and BDT at their tCTP resonance crudely. In our simulations, we used an electric field of 7×10^8 V/m resulting in a conductance of 3238G_0 for EDT and 7321G_0 for BDT, where the molecular length is 0.5 nm for EDT and 0.6 nm for BDT, the cross sectional area of the both SAM layers are 37×37 nm^2, and G_0 is the quantum conductance. We estimate that 16000 molecules are present in the junction based on a previously reported surfaces coverage of 8.0×10^{-10} mol/cm^2 for these molecules on Ag surfaces.[40-41] Therefore, the conductance per EDT or BDT molecule is roughly 0.20 G_0 and 0.46 G_0 at the tCTP resonance respectively. These single molecule conductance values are in good agreement with those literature reported for break junction measurements.[42-43]

We have also performed electron-beam excitation simulations, which produce similar results as our plane-wave excitation simulations as shown in Figure 4.10. The electron-beam excitation is modelled as a small electron beam (~1 nm^2) which carries current in the incident direction and creates an electromagnetic field background, and then the optical extinction spectra of the particle system are collected.

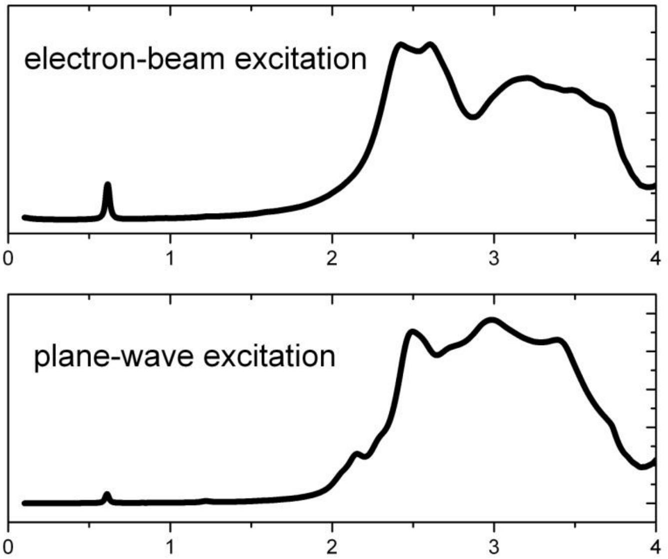

Figure 4.10 Simulated EELS spectra for an Ag-EDT-Ag dimer system using an optical approach for electron-beam excitation (top panel) and plane-wave excitation (bottom panel, as shown in Figure 4.6).

The reason why we choose the present plane-wave excitation is mainly due to its simpler physics and less free-tuning parameters in simulation which makes the simulation results more reliable. Compared to the well-established plane-wave excitation modelling, using an optical approach to model electron-beam excitation is still a relatively new research area[44-45] and more efforts will be made toward this direction.

4.5. References

1. Tame, M. S.; McEnery, K. R.; Ozdemir, S. K.; Lee, J.; Maier, S. A.; Kim, M. S., Quantum plasmonics. *Nature Physics* **2013,** *9* (6), 329-340.
2. Brongersma, M. L.; Shalaev, V. M., The Case for Plasmonics. *Science* **2010,** *328* (5977), 440-441.
3. Romero, I.; Aizpurua, J.; Bryant, G. W.; García De Abajo, F. J., Plasmons in nearly touching metallic nanoparticles: singular response in the limit of touching dimers. *Optics Express* **2006,** *14* (21), 9988-9999.
4. Zuloaga, J.; Prodan, E.; Nordlander, P., Quantum Description of the Plasmon Resonances of a Nanoparticle Dimer. *Nano Letters* **2009,** *9* (2), 887-891.
5. Marinica, D. C.; Kazansky, A. K.; Nordlander, P.; Aizpurua, J.; Borisov, A. G., Quantum Plasmonics: Nonlinear Effects in the Field Enhancement of a Plasmonic Nanoparticle Dimer. *Nano Letters* **2012,** *12* (3), 1333-1339.
6. Savage, K. J.; Hawkeye, M. M.; Esteban, R.; Borisov, A. G.; Aizpurua, J.; Baumberg, J. J., Revealing the quantum regime in tunnelling plasmonics. *Nature* **2012,** *491* (7425), 574-577.
7. Song, P.; Nordlander, P.; Gao, S., Quantum mechanical study of the coupling of plasmon excitations to atomic-scale electron transport. *The Journal of Chemical Physics* **2011,** *134* (7), -.
8. Kern, J.; Großmann, S.; Tarakina, N. V.; Häckel, T.; Emmerling, M.; Kamp, M.; Huang, J.-S.; Biagioni, P.; Prangsma, J. C.; Hecht, B., Atomic-Scale Confinement of Resonant Optical Fields. *Nano Letters* **2012,** *12* (11), 5504-5509.
9. Esteban, R.; Borisov, A. G.; Nordlander, P.; Aizpurua, J., Bridging quantum and classical plasmonics with a quantum-corrected model. *Nature Communications* **2012,** *3*, 825.

10. Scholl, J. A.; García-Etxarri, A.; Koh, A. L.; Dionne, J. A., Observation of Quantum Tunneling between Two Plasmonic Nanoparticles. *Nano Letters* **2012,** *13* (2), 564-569.

11. Duan, H.; Fernández-Domínguez, A. I.; Bosman, M.; Maier, S. A.; Yang, J. K. W., Nanoplasmonics: Classical down to the Nanometer Scale. *Nano Letters* **2012,** *12* (3), 1683-1689.

12. Henzie, J.; Andrews, S. C.; Ling, X. Y.; Li, Z.; Yang, P., Oriented assembly of polyhedral plasmonic nanoparticle clusters. *Proceedings of the National Academy of Sciences* **2013,** *110* (17), 6640-6645.

13. Tan, S. F.; Wu, L.; Yang, J. K. W.; Bai, P.; Bosman, M.; Nijhuis, C. A., Quantum Plasmon Resonances Controlled by Molecular Tunnel Junctions. *Science* **2014,** *343* (6178), 1496-1499.

14. Salomon, A.; Cahen, D.; Lindsay, S.; Tomfohr, J.; Engelkes, V. B.; Frisbie, C. D., Comparison of Electronic Transport Measurements on Organic Molecules. *Advanced Materials* **2003,** *15* (22), 1881-1890.

15. Reed, M. A.; Zhou, C.; Muller, C. J.; Burgin, T. P.; Tour, J. M., Conductance of a Molecular Junction. *Science* **1997,** *278* (5336), 252-254.

16. Cui, X. D.; Primak, A.; Zarate, X.; Tomfohr, J.; Sankey, O. F.; Moore, A. L.; Moore, T. A.; Gust, D.; Nagahara, L. A.; Lindsay, S. M., Changes in the Electronic Properties of a Molecule When It Is Wired into a Circuit. *The Journal of Physical Chemistry B* **2002,** *106* (34), 8609-8614.

17. Nijhuis, C. A.; Reus, W. F.; Barber, J. R.; Whitesides, G. M., Comparison of SAM-Based Junctions with Ga2O3/EGaIn Top Electrodes to Other Large-Area Tunneling Junctions. *The Journal of Physical Chemistry C* **2012,** *116* (26), 14139-14150.

18. Joachim, C.; Ratner, M. A., Molecular electronics: Some views on transport junctions and beyond. *Proceedings of the National Academy of Sciences of the United States of America* **2005,** *102* (25), 8801-8808.

19. McCreery, R. L., Molecular Electronic Junctions. *Chemistry of Materials* **2004,** *16* (23), 4477-4496.

20. Wu, L.; Duan, H.; Bai, P.; Bosman, M.; Yang, J. K. W.; Li, E., Fowler–Nordheim Tunneling Induced Charge Transfer Plasmons between Nearly Touching Nanoparticles. *ACS Nano* **2012,** *7* (1), 707-716.

21. Nelayah, J.; Kociak, M.; Stephan, O.; Garcia de Abajo, F. J.; Tence, M.; Henrard, L.; Taverna, D.; Pastoriza-Santos, I.; Liz-Marzan, L. M.; Colliex, C., Mapping surface plasmons on a single metallic nanoparticle. *Nature Physics* **2007,** *3* (5), 348-353.

22. Michel, B.; Vicki, J. K.; Masashi, W.; Abbas, I. M.; Michael, B. C., Mapping surface plasmons at the nanometre scale with an electron beam. *Nanotechnology* **2007,** *18* (16), 165505.

23. Bosman, M.; Ye, E.; Tan, S. F.; Nijhuis, C. A.; Yang, J. K. W.; Marty, R.; Mlayah, A.; Arbouet, A.; Girard, C.; Han, M.-Y., Surface Plasmon Damping Quantified with an Electron Nanoprobe. *Scientific Reports* **2013,** *3*.

24. Yuan, L.; Breuer, R.; Jiang, L.; Schmittel, M.; Nijhuis, C. A., A Molecular Diode with a Statistically Robust Rectification Ratio of Three Orders of Magnitude. *Nano Letters* **2015,** *15* (8), 5506-5512.

25. Strange, M.; Rostgaard, C.; Häkkinen, H.; Thygesen, K. S., Self-consistent GW calculations of electronic transport in thiol- and amine-linked molecular junctions. *Physical Review B* **2011,** *83* (11), 115108.

26. Reddy, P.; Jang, S.-Y.; Segalman, R. A.; Majumdar, A., Thermoelectricity in Molecular Junctions. *Science* **2007,** *315* (5818), 1568-1571.

27. Xiao; Xu; Tao, N. J., Measurement of Single Molecule Conductance: Benzenedithiol and Benzenedimethanethiol. *Nano Letters* **2004,** *4* (2), 267-271.

28. Scheer, A. M.; Gallup, G. A.; Burrow, P. D., Unoccupied orbital energies of 1,4-benzenedithiol and the HOMO–LUMO gap. *Chemical Physics Letters* **2008,** *466* (4–6), 131-135.

29. Wold, D. J.; Frisbie, C. D., Formation of Metal−Molecule−Metal Tunnel Junctions: Microcontacts to Alkanethiol Monolayers with a Conducting AFM Tip. *Journal of the American Chemical Society* **2000,** *122* (12), 2970-2971.

30. Levine, I.; Weber, S. M.; Feldman, Y.; Bendikov, T.; Cohen, H.; Cahen, D.; Vilan, A., Molecular Length, Monolayer Density, and Charge Transport: Lessons from Al–AlOx/Alkyl–Phosphonate/Hg Junctions. *Langmuir* **2012,** *28* (1), 404-415.

31. Kaasbjerg, K.; Flensberg, K., Strong Polarization-Induced Reduction of Addition Energies in Single-Molecule Nanojunctions. *Nano Letters* **2008,** *8* (11), 3809-3814.

32. Barr, J. D.; Stafford, C. A.; Bergfield, J. P., Effective field theory of interacting π-electrons. *Physical Review B* **2012,** *86* (11), 115403.

33. HeimelG; DuhmS; SalzmannI; GerlachA; StrozeckaA; NiederhausenJ; BürkerC; HosokaiT; Fernandez Torrente, I.; SchulzeG; WinklerS; WilkeA; SchlesingerR; FrischJ; BrökerB; VollmerA; DetlefsB; PflaumJ; KeraS; Franke, K. J.; UenoN; Pascual, J. I.; SchreiberF; KochN, Charged and metallic molecular monolayers through surface-induced aromatic stabilization. *Nature Chemistry* **2013,** *5* (3), 187-194.

34. Wu, S.; Gonzalez, M. T.; Huber, R.; Grunder, S.; Mayor, M.; Schonenberger, C.; Calame, M., Molecular junctions based on aromatic coupling. *Nature Nanotechnology* **2008,** *3* (9), 569-574.

35. Ho Choi, S.; Kim, B.; Frisbie, C. D., Electrical Resistance of Long Conjugated Molecular Wires. *Science* **2008,** *320* (5882), 1482-1486.

36. Pontes, R. B.; Rocha, A. R.; Sanvito, S.; Fazzio, A.; da Silva, A. J. R., Ab Initio Calculations of Structural Evolution and Conductance of Benzene-1,4-dithiol on Gold Leads. *ACS Nano* **2011,** *5* (2), 795-804.

37. Palik, E. D., *Handbook of Optical Constants of Solids* Academic: San Diego, California, 1991.

38. Haynes, W. M., *CRC Handbook of Chemistry and Physics*. 94th ed.; Taylor and Francis: 2013.

39. Bosman, M.; Zhang, L.; Duan, H.; Tan, S. F.; Nijhuis, C. A.; Qiu, C. W.; Yang, J. K. W., Encapsulated Annealing: Enhancing the Plasmon Quality Factor in Lithographically–Defined Nanostructures. *Scientific Reports* **2014,** *4*.

40. Sellers, H.; Ulman, A.; Shnidman, Y.; Eilers, J. E., Structure and binding of alkanethiolates on gold and silver surfaces: implications for self-assembled monolayers. *Journal of the American Chemical Society* **1993,** *115* (21), 9389-9401.

41. Cox, E. G.; Cruickshank, D. W. J.; Smith, J. A. S., The Crystal Structure of Benzene at -3○ C. *Proceedings of the Royal Society of London. Series A, Mathematical and Physical Sciences* **1958,** *247* (1248), 1-21.

42. Kiguchi, M. S., N. ; Murakoshi, K., In-Situ Preparation of a Single Molecular Junction with Mechanically Controllable Break Junctions in Vacuum. *Journal of Physics: Conference Series* **2008,** *100*, 052059.

43. Kim, Y.; Pietsch, T.; Erbe, A.; Belzig, W.; Scheer, E., Benzenedithiol: A Broad-Range Single-Channel Molecular Conductor. *Nano Letters* **2011,** *11* (9), 3734-3738.

44. García de Abajo, F. J., Optical excitations in electron microscopy. *Reviews of Modern Physics* **2010,** *82* (1), 209-275.

45. Bigelow, N. W.; Vaschillo, A.; Iberi, V.; Camden, J. P.; Masiello, D. J., Characterization of the Electron- and Photon-Driven Plasmonic Excitations of Metal Nanorods. *ACS Nano* **2012,** *6* (8), 7497-7504.

Chapter 5

Stability of Silver and Gold Nanoparticles under Electron Beam Irradiation

Abstract: *The STEM-EELS experiments that have been introduced in Chapter 4 were performed on closely-spaced gold nanocuboids as well. However, the high aspect ratio gaps degraded in many cases as a result of filament formation during electron beam irradiation. In this Chapter, a detailed study on the degradation mechanisms and preventive approaches is given, focusing in particular on the nanoparticle coatings that could act as a protective barrier for minimizing the electron beam induced damage on passivated gold and silver nanoparticles.*

5.1. Introduction

Nanoparticles with tunable surface properties are used in many applications, ranging from nanostructured catalysis, (quantum) plasmonics, to surface-enhanced Raman spectroscopy. The characterization of nanoparticles often involves the utilization of transmission electron microscope (TEM) or scanning electron microscope (SEM) based techniques, but these techniques rely on high-energy electron beams which cause (un)wanted changes to the specimen such as degradation, radiolysis of surface molecules, contamination build-up, electron beam-induced atomic displacements, or heating. Nanoparticles have limited stability under these conditions and the mechanisms of electron beam-induced damages are poorly understood.

Passivated nanoparticles are potential building blocks of novel devices and materials,[1-4] so a better understanding of nanoparticle stability under analysis conditions would be useful to avoid drawing faulty conclusions from experimental observations. Here, an investigation is presented on whether different types of coatings on Au and Ag nanocuboids could prevent, or significantly reduce electron beam radiation damage. These noble metal nanoparticles are meta-stable and their morphology is usually stabilized by an organic monolayer such as cetyl trimethyl ammonium bromide, self-assembled monolayers of thiolates or a polymer such as poly (vinyl pyrrolidone), ethylene glycol, etc.

Electron beam-induced damages and the preventive approaches reported in literature to minimize the effects were discussed in Chapter 2. Among the effects mentioned above, the knock-on damage and the ionization damage are critical for organic monolayer-coated inorganic nanoparticles. Knock-on effects usually occur in conducting inorganic specimens[5] where the accelerating voltage of the incident electron beam is higher than the displacement energy of the material or when the electron dose exceeds 1000 C cm^{-2}. On the other hand, ionization damage is predominant for insulators, such as organic monolayer molecules in our study, at all incident energies (10-300 keV).

5.2. Results & Discussion

5.2.1. Synthesis and Functionalization of Silver and Gold Nanocuboids

We refer to Chapter 3, Section 3.2.2 for the synthesis and functionalization of silver nanocuboids. The experimental details of the synthetic procedures and characterization techniques are reported in the experimental section at end of Chapter 3.

Besides silver, we shall also look at gold nanocuboids in this Chapter. For these, we followed the seed-mediated method developed by Sun *et al.*[6] The experimental details of the synthetic procedures and characterization techniques are reported in the experimental section at end of this Chapter. Here, only a brief description is given.

The synthesis of gold nanocuboids was performed by a two-step method. First, a gold seed solution was prepared by rapid reduction of the gold precursor i.e.: chloroauric acid with a strong reducing agent sodium borohydride in the presence of surfactant cetyltrimethylammonium bromide. The seed solution contained quasi-spherical gold nanoparticles of size less than 5 nm. In the second step, the seed was added into the growth solution which consisted of gold precursor, a mild reducing agent, i.e. ascorbic acid and a chemical additive: copper sulfate. Carefully controlling the concentration of each component enables the formation of gold nanocuboids stabilized with {100} facets.

The silver and gold nanocuboids were functionalized with mixed self-assembled monolayers (SAMs) of thiolates and ditholates and the polymer PVP, following the method described previously in Chapter 3.

5.2.2. Tunneling CTP between Gold Nanocuboids

We performed monochromated STEM-EELS experiments (introduced in Chapter 4) on gold cuboids, with PDT as the SAM in the gap. Gold is much more susceptible to electron beam-induced changes to the morphology, so imaging had to be performed in low-dose STEM mode. We could not obtain TEM images without inducing morphological changes to the gold in the gap due to the high dose exposure during TEM imaging.

Figure 5.1 shows a series of EELS measurements that were taken during the formation of filaments in the dimer gap. Before starting the monochromated EELS measurements, a low-dose STEM image was taken (at 200 kV, with a 0.2 nm probe) of the gold dimer; no filaments were observed in the 0.5-0.7 nm gap. Monochromated EELS was subsequently performed, starting with the black EELS spectrum in panel (b), and finishing 180 s later with the yellow spectrum.

Without further illuminating the dimer, another STEM image was taken at 200 kV (Figure 5.1 a, top panel), showing gold filaments that were formed in the gap. A close look at the low-energy peaks in panel (b) shows that there is a transition from the tCTP mode (▲) to a conventional (non-tunneling) CTP (●) mode during the cause of the EELS measurements when the filaments formed.

For both cases CTP and tCTP, charge is transferred from one particle to an adjacent particle. We use the term (1) CTP for gaps filled with gold/silver filaments and (2) tCTP for gaps filled with molecules. We have chosen to make this distinction in order to emphasize the different nature of the charge transfer mechanisms. In the case of a gold/silver bridge or filament between the two particles, a current of electrons flows across the bridge, at a resonant frequency that is only weakly dependent on the length of the bridge. In the case of a molecule-filled gap, charge is transferred via tunneling, which is more strongly dependent on the length of the bridge. Moreover, with tunneling as conduction mechanism, there are other potential ways to control the tunneling rate. Using the difference in molecular quantum conductance, for example, as we have demonstrated (Chapter 4) by showing the strong difference in resonance frequency between EDT- and BDT-filled gaps, even when the gap lengths are the same. Another example is the use of the molecular alignment as a tuning factor which is not possible for a gold/silver bridges, as these materials are isotropic conductors. It is also expected (but we have not yet experimentally demonstrated this) that the tCTP is more temperature-sensitive than the normal CTP mode, due to the temperature-sensitivity of the tunneling mechanism.

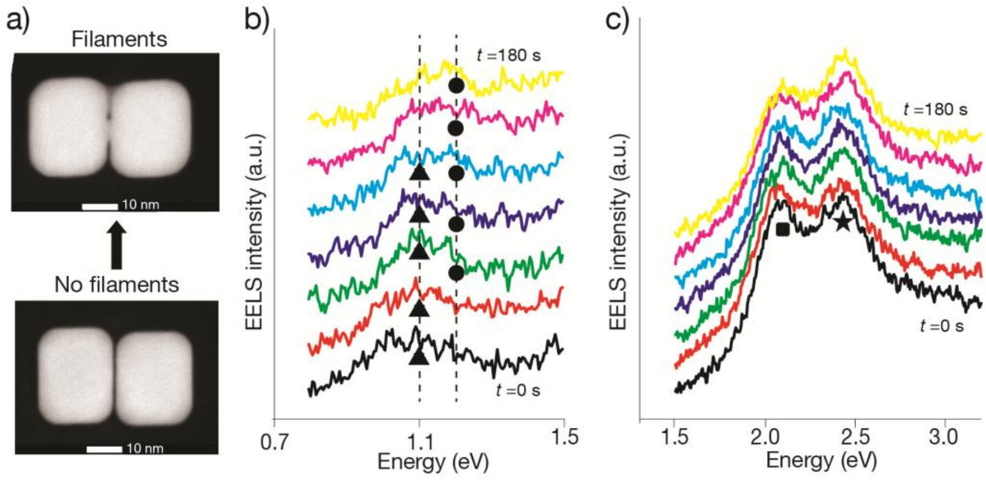

Figure 5.1 (a) STEM images of the dimer recorded before and after EELS measurements. (b) Transition from the tunneling charge transfer (tCTP) mode at 1.05 eV (with a clean gap, labeled with ▲) to the conventional, non-tunneling CTP mode at 1.18 eV (when filaments are formed in the gap, labeled with ●), acquired over a 180 s time interval. (c) EELS spectra for

the same data in the energy range of 1.5 to 3.0 eV. The ratio of the higher-energy peaks (labeled with ■ and ★) changed from 1: 0.9 to 1: 1.6. The widening of the filament reduces the charge reflection at the gap and therefore lowers the bonding dipolar mode.

5.2.3. Filament Formation between Closely-Spaced Gold Nanocuboids

To investigate the filament formation in more detail, a time-lapse series of TEM images (Figure 5.2) was recorded where filament formation is observed between two gold nanocubes upon electron beam irradiation. The imaging is done on the mixed SAMs -coated Au nanocubes with 200 kV electrons, using electron doses ranging from 2000 to 2500 e/(Å^2·s) for 32 minutes.

Filament formation between two gold nanocubes was observed, in the following order. (1) Tiny filaments (~2-3 nm) form between the corners of each nanocube. (2) The filaments grow and fill up the whole gap gradually. (3) Two nanocubes are completely connected when the filaments have filled the whole gap.

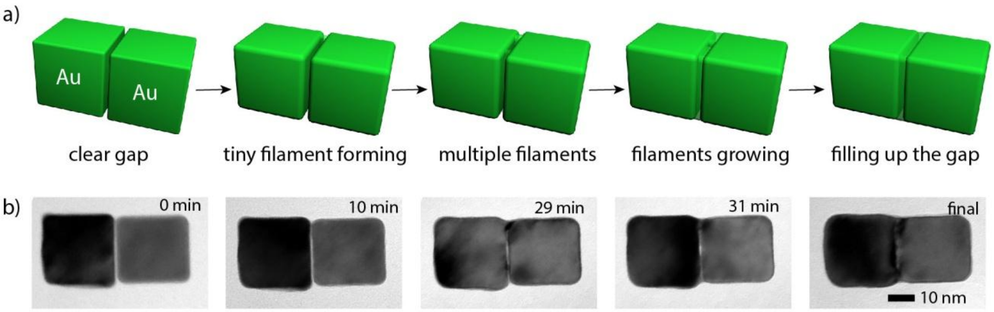

Figure 5.2 (a) Schematic the filament formation between gold nanocubes coated with SAMs of thiolates under electron beam irradiation. (electron dose: 2000-2500 e/Å^{2}s) (b) A time-resolved series of TEM images where filaments form and grow between two closely-spaced

monocrystalline gold nanocuboids coated with SAMs on a copper grid. Eventually, the gap is filled completely and the two particles are merged.

In an attempt to avoid the filament formation, we functionalized the gold cuboids with the polymer poly (vinyl) pyrrolidone (PVP). PVP is a commonly used capping agents in nanoparticle synthesis because it selectively interacts with {100} facets and prevents the nanoparticles suspension to aggregate *via* steric repulsion resulting in kinetically (i.e., not thermodynamically) stable monocrystalline Ag nanocubes.[7-8] It is worth noting that kinetic stability occurs in colloidal suspension, however, the situation for dried particles will likely to be different. Previous studies[8] suggested that as the layer of PVP was dried, it is likely that the polymer collapsed due to the removal of hydrogen bonding with water, causing the carbonyl groups to lay parallel to the metal surface. Here, we irradiated PVP and SAMs-coated Au nanocuboids with 200 kV electrons, with doses ranging from 100 to 1300 e/($Å^2$·s) for 24 and 42 minutes, respectively, as shown in Figure 5.3. We observed the filament formation between two thiolates-SAMs -coated gold cube dimer but not for the one with PVP coatings. Many studies[9-12] report that sintering of two nanoparticles separated by 1-2 nm occurs when the atoms in the material diffuse across the surfaces of the particles, fusing the particles together to constitute one solid piece. Two sintering mechanisms are reported[13]: (1) Ostwald Ripening (2) Surface diffusion. Since the particles are not in solution, we suggest the latter case is dominant for the filament formation in this study.

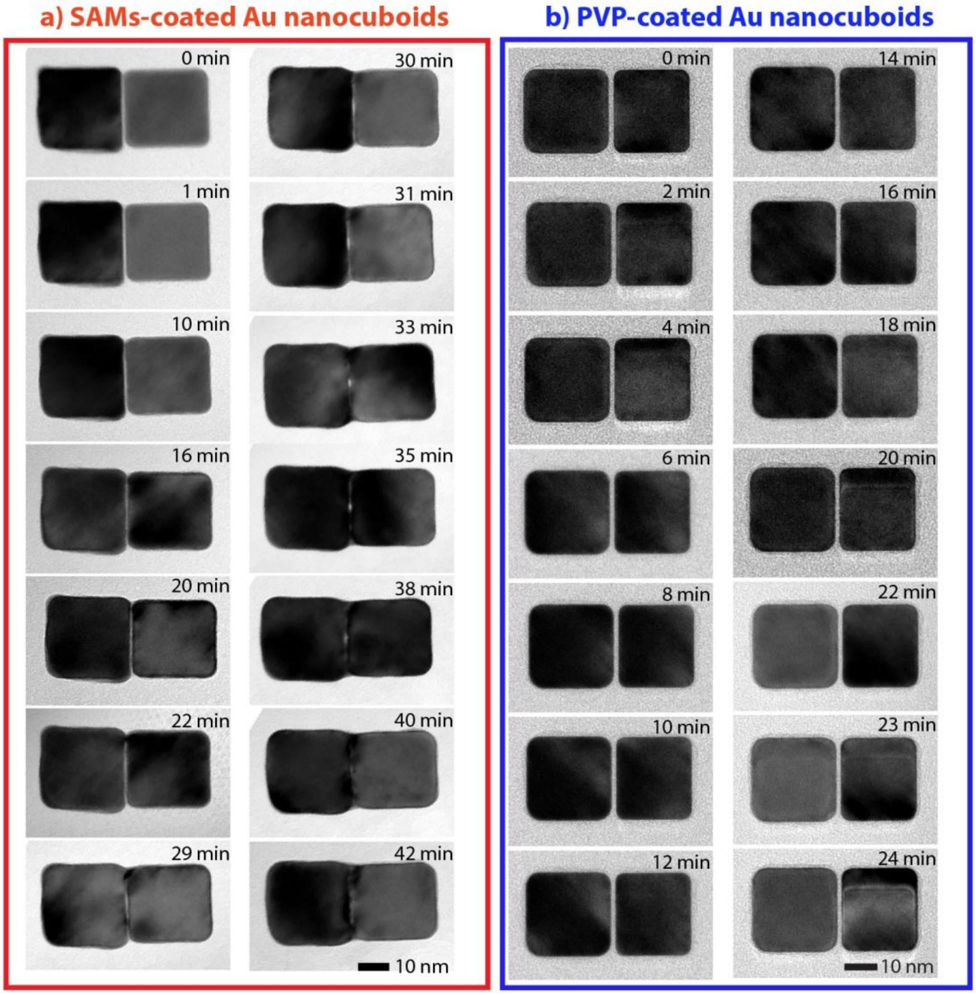

Figure 5.3 (a) and (b) show the sequence of high resolution transmission electron microscopy (TEM) images of filament formation of single-crystalline gold cube dimer coated with SAMs (electron dose: 2000-2500 e/Å^{2}s) and PVP (electron dose for the first 20 minutes: 100-120 e/Å^{2}s, after 20 minutes: 1100-1300 e/Å^{2}s) on copper grid under electron beam irradiation.

However, this problem still persists even though we performed the same experiment at liquid nitrogen temperature by using a special cooling holder. It has been proposed that lowering the temperature would help in reducing the sensitivity of an organic species to structural damage and mass loss, even though it does not change the inelastic cross-section.[14] In this case, lowering the temperature does not help to slow down the subsequent diffusion processes but coating with long chain polymer does. Surprisingly, the polymer PVP acts as a diffusion barrier that could significantly minimize the possibility of the surface diffusion driven filament formation. It is well-known that the ring-containing chemical species (PVP) would be more resistant than the aliphatic molecules (alkanethiolate SAMs) towards electron beam induced damage since the irreversible bond scissions will require higher energy.[15] This shows that the ligands stability is crucial in protecting the metal nanoparticles against the electron beam.

5.2.4. The Role of Ligands

We now replace Au nanocuboids with Ag nanocubes. It is well-known that Ag is harder than Au (Vickers hardness Ag = 251 MN/m^2, Au = 216 MN/m^2). However, the displacement (E_d) and sputtering (E_s) threshold energies of silver (E_d and E_s are 28 eV and 7-14 eV respectively) are lower than those of gold (E_d and E_s are 36 eV and 9-18 eV respectively).[16]

Figure 5.4 (a) schematically illustrates the deformation of a silver nanocube coated with a mixed SAM of 1-propanethiolate and 1,2-ethanedithiolate (volume ratio of 5:3) with a thickness of 0.5 nm while irradiated on a SiN_x membrane with an electron beam of 200 kV with electron doses ranging from 100 to 3000 $e/(Å^2 \cdot s)$. Figure 5.4 (b) shows the sequence of TEM acquired images, along with the corresponding fast Fourier Transforms, of a single silver nanocube recorded at intervals of 2 minutes over a period of 27 minutes (after which the experiment was stopped).

During the first 6 minutes, the particle morphology did not change noticeably, but at t = 6 minutes protrusions formed at the faces of the nanocube (indicated by red triangles). These protrusions have lower contrast than the rest of the particle and therefore they are probably thinner than the cubic nanoparticle. The monocrystalline FCC crystal structure of the original particle remains visible up to t = 22 minutes, but the final state is a quasi-spherical, polycrystalline FCC Ag nanoparticle.

The degradation started from the top or bottom facet of the cube where we observed a contrast change (green triangles), subsequently the newly-formed protrusions (red triangle) emerged at the corners and edges. At the same time, the size of the silver nanocube shrank and its corners became more and more truncated.

After 10 minutes, we observed a new lattice reflection spot emerged which arising from the (111) reflection originated from FCC silver protrusions. From this experiment we conclude that mixed SAMs do not stabilize the Ag nanocube under high e-beam irradiation.

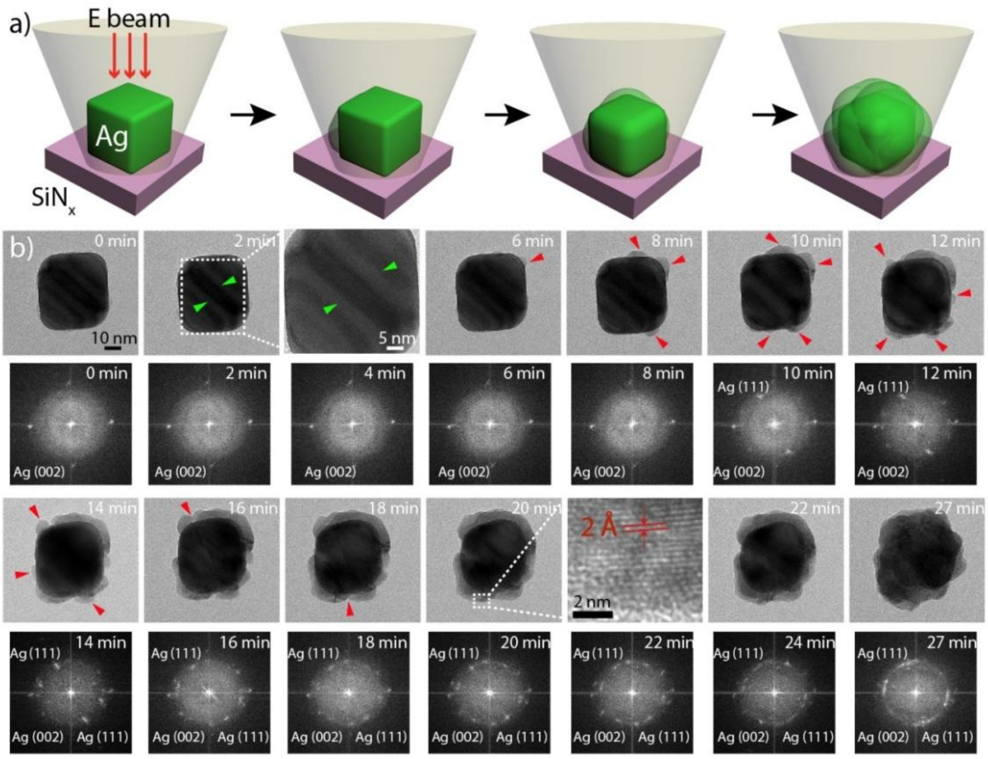

Figure 5.4 (a) Schematic the deformation of silver nanocube coated with SAMs of thiolates under electron beam irradiation. (b) Sequence of high resolution transmission electron microscopy (TEM) and the corresponding Fast Fourier Transforms of a single-crystalline silver cube coated with SAMs on SiN_x membrane, during electron beam irradiation (electron dose: 1500-2000 e/$Å^2$s), where a cube-shaped particle evolves to an irregular quasi-spherical particle.

A similar experiment was performed by drop-casting the as-synthesized, PVP-coated Ag nanocubes onto the 30 nm thick silicon nitride membrane. To investigate whether PVP also stabilizes the NPs during a typical TEM experiment, we irradiated PVP-coated Ag nanocubes with 200 kV electrons, with doses ranging from 1100 to 2000 e/($Å^2$·s) for 20 minutes.

Figure 5.5 shows a sequence of TEM images of a single silver nanocube coated with PVP. At t = 0, the particle had a PVP layer of 2.8 nm thickness, appearing in the images as a slight change in contrast around the nanocube. During the entire course of the experiment, the Ag particle remained stable and no obvious changes in shape or phase were observed, but the organic layer surrounding the particle increased in thickness from 2.8 to 6.1 nm.

We attribute this increase in the thickness to the e-beam-induced build-up of organic contamination. Contamination in electron microscopy often refers to the electron beam induced deposition (EBID) where there is an interaction between the electron beam and organic matter,[17-18] i.e., PVP in our case. The PVP tends to crosslink and form structures on the sample that are clearly visible in TEM images[19] as seen in Figure 5.5. Muller *et al.*[20] also reported that the non-conducting electron beam-induced carbon contamination layers can possibly act as both diffusion and sputtering barrier, thereby preventing structural damage. From this experiment, we conclude that a thin PVP coating, unlike SAMs, stabilizes the Ag nanocubes during e-beam irradiation. This is probably due to the stability of the molecules against electron beam irradiation and, hence, we conclude that monolayers of thiolates can easily suffer from ionization damage but polymers like PVP which are thicker than the monolayer thiolates tend to be stable against ionization damage induced by the electron beam.

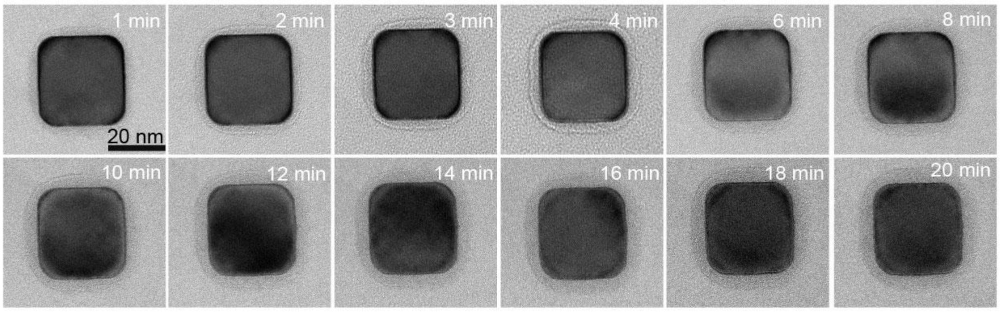

Figure 5.5 Sequence of TEM images of a monocrystalline silver cube coated with polymer (polyvinylpyrrolidone) on a SiN_x membrane, during electron beam irradiation. (electron dose: 1100-2000 e/Å^{2}s) The cubical-shaped was maintained throughout the whole illumination period.

From experiments above, we infer that PVP-coated Ag nanocubes are stable against electron beam irradiation but mixed SAMs coated ones are not. To further understand the degradation mechanism, we performed the same experiment on dimers with the two types of coatings. Figure 5.6 shows the effect of electron beam irradiation on a dimer of silver nanocubes coated with SAMs of thiolates (Figure 5.6 a) and with PVP (Figure 5.6 b).

We make the following three observations for the dimer coated with SAMs. (1) During electron beam irradiation, the degradation starts from the centre of the cube (green triangles) where we observe a contrast change. (2) Subsequently, newly-formed protrusions emerge at the corners and edges. (3) At the same time, the silver nanocubes become more and more truncated and finally turn into rounded nanocubes. The observed phenomena for the Ag nanocubes dimers are similar to those of single silver nanocubes functionalized with thiolated-SAMs. In other words, when we observe degradation of single particles, they will also occur on dimers, and when single particles are stable, so are dimers.

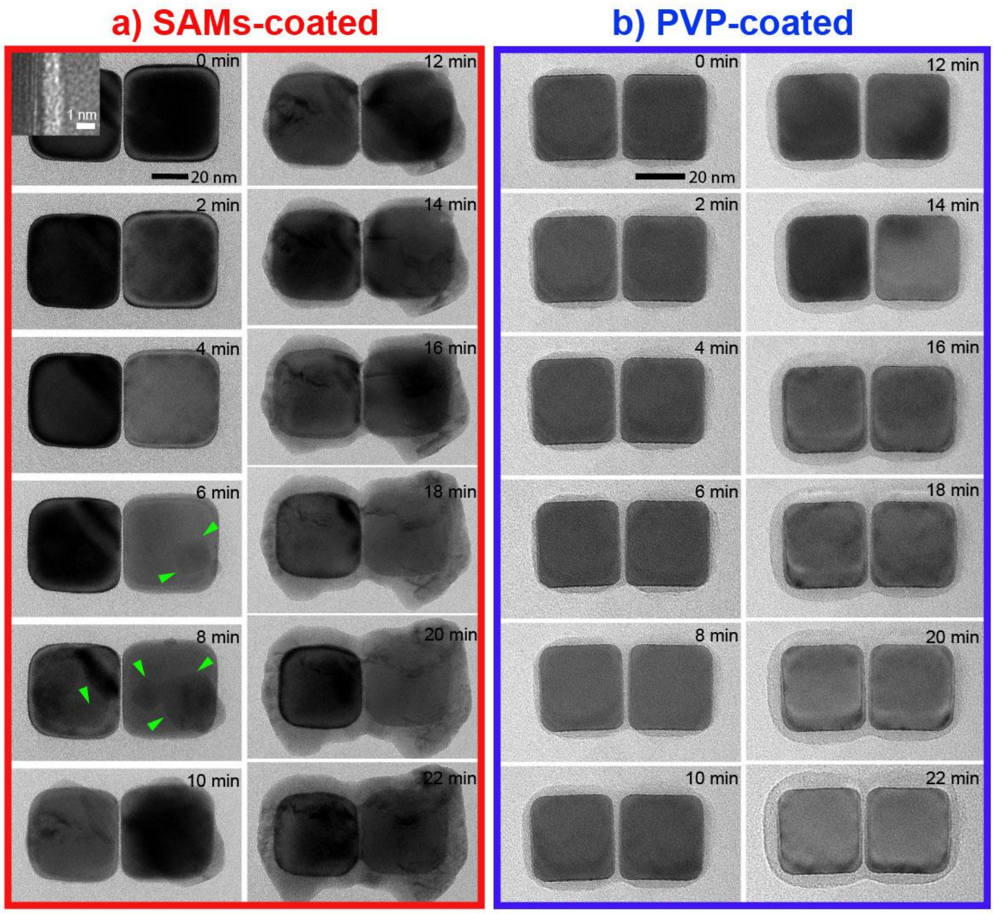

Figure 5.6 (a) and (b) A comparison between SAMs-coated and polymer-coated silver nanocubes dimers. Two sequences of TEM images are shown with monocrystalline silver cube dimers, coated with either SAMs (thiolates) or with a polymer capping agent (PVP) on a SiNx membrane under electron beam irradiation. (electron dose: 1500-2000 e/Å^{2}s)

Chen *et al.*[13] reported that the sintering behavior of nanoparticles is dependent on the stability of the molecules against electron beam damage. Thus, the extent of electron beam-induced damage depends on the ability of the molecules to stabilize the surface atoms even while they are being bombarded by fast electrons. Here, we observed the degradation, i.e., formation of silver protrusions between two nanoparticles for the case of thiolates-coated nanocube dimers while the particles coated with PVP still maintained their good square shape. The interaction between PVP and Ag nanoparticles is thought to occur between the Ag atoms and the carbonyl group located on the pyrrolidone ring[21] (Figure 5.7 c-d) while the monolayer of thiolates molecules bind to the Ag nanoparticles *via* an Ag-S covalent bond[22] (Figure 5.7 a-b). It is well-known that energy transferred during inelastic scattering would cause heating within the specimen and the temperature rise in an organic specimen can reach a few hundred degrees for a stationary probe.[23] We speculate that the heating caused by the electron beam degrade both the ligands (SAMs and the PVP molecules) in different ways. Our observations show that thiolated SAMs lead to a more rapid growth of the protrusions (Figure 5.6 a), especially along the interface with the SiN_x. In effect, the particle is 'bleeding away' surface atoms that spread-out over the SiN_x membrane.

On the other hand, thermal degradation of PVP is accompanied by the release of pyrrolidone rings as reported before.[21, 24-25] This surprising results in pyrrolidone rings that bind in a bridging, side-on fashion, more strongly absorbed on the nanoparticle surface than units that are only singly coordinated. A schematic of this bidentate ligand is shown in Figure 5.7 (e-f). Although the bond strength of metal-sulfur (Ag-S) covalent bond is stronger than the singly coordination bond,[8, 22] the bidentate coordination bond formation as a result of interface heating caused by electron beam irradition may be the reason for PVP-coated particles to be well-protected against electron beam irradiation. Even though the exact mechanism is not elucidated here, the results were reproducible and practically useful enough to include PVP coating to stabilize our SAM-coating experiments.

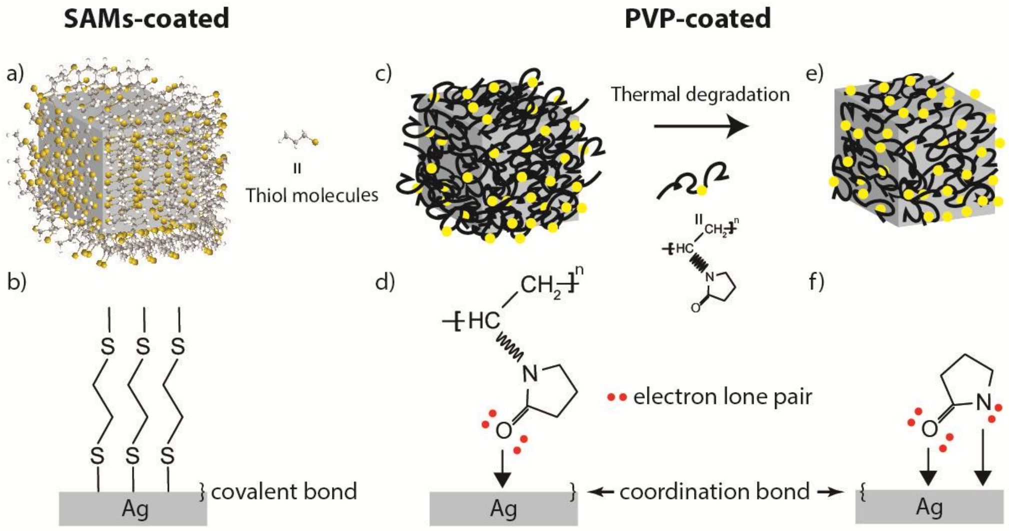

Figure 5.7 Illustration of (a) thiolated SAMs and (b) bonding to the metal nanoparticles. Schematic of the PVP coating at the nanoparticle surface and the bonding to Ag nanocubes (c-d) before (monodentate ligand) and (e-f) (bidentate ligand) after thermal degradation (model adapted from Borodko *et al.*[21]) .

5.3. Conclusions

In short, surface diffusion driven filament formation is an important factor to consider for the TEM study of passivated gold nanoparticles. For passivated silver nanoparticle on the other hand, electron beam-induced heating at metal-ligand interface appears to be the main degradation mechanism. We have demonstrated the important role of ligands in maintaining the shape of gold and silver nanocubes under TEM electron beam irradiation.

Self-assembled monolayers of thiolates molecules have very low stability in protecting nanoparticles against electron beam damage while coating the particles with polymers such as PVP may evolve as a new method for stabilization in order to improve the lifetime of plasmonic devices and materials under characterization conditions.

5.4. Experimental Section

5.4.1. General Procedures. For the silver nanocuboids, the chemicals poly (vinyl) pyrridone, silver nitrate, 1,2-ethanedithiol, 1,4-benzenedithiol were all purchased from Sigma-Aldrich and used without further purification. Sodium sulfide and ethylene glycol were purchased from J.T. Baker. For the gold nanocuboids, the chemicals 1-butanethiol, 1,3-propanedithiol, gold (ш) chloride trihydrate, sodium borohydride, cetyltrimethylammonium bromide, copper sulfate, L-ascorbic acid were all purchased from Sigma-Aldrich and used without further purification. The glass vials used for synthesis were obtained from Fisher Scientific. Solvents for nanoparticles functionalization were freshly distilled prior to use. All stirrer bars were soaked in aqua-regia (mixture of 1:3 volume ratio of nitric acid: hydrochloric acid) for at least 1 hour, washed with deionized water (18.2 Ωcm) and dried in an oven before use. Nanoparticles were washed in Rotina (model 380R) and Profuge (model 14D) centrifuges.

5.4.2. Synthesis of Silver Nanocubes. Refer to Chapter 3 Section 3.4.

5.4.3. Functionalization of Silver Nanocubes with Mixed SAMs. Refer to Chapter 3 Section 3.4.

5.4.4. Synthesis of Gold Nanocubes: We followed the seed-mediated method[6] developed by Sun *et al.* A gold seed solution was prepared by reducing 6.25 ml of $HAuCl_4 \cdot 3H_2O$ (1.0 mM) with 0.15 ml of ice-cold sodium borohydride aqueous solution ($NaBH_4$, 0.1 M) in the presence of 18.75 ml of cetyltrimethylammonium bromide aqueous solution (CTAB, 0.1 M). The $NaBH_4$ solution was added at once to a solution containing CTAB and gold precursor. We left the reaction mixture to stir for 4 hours at room temperature before proceeding to the next step. For the growth solution of gold nanocuboids, 20.0 ml of CTAB (0.02 M) was added to a clean polypropylene tube, followed by the addition of 5.0 ml of $HAuCl_4 \cdot 3H_2O$ (2.0 mM) aqueous solution. Then we added 50 µl of copper sulfate ($CuSO_4$, 0.01 M) aqueous solution, 3.0 ml of L-ascorbic acid (L-AA, 0.1 M) and 5.0 µl of gold seed solution sequentially. The solution was gently mixed by inversion of the test tube after the addition of each component.

5.4.5. Functionalization of Gold Nanocubes with Mixed SAMs: The gold nanocuboids solution was subjected to three times of washing treatment by centrifugation and re-dispersion in order to minimize the concentration of CTAB surfactant molecules before functionalization. Specifically, 1.5 µl of 1-butanethiol (BT) solution (1.0 mM in CH_3CN:H_2O mixture of 4:1) and 1.5 µl of 1,3-propanedithiol (PDT) solution (1.0 µM in CH_3CN:H_2O mixture of 4:1) was added into 2.0 ml of CH_3CN:H_2O mixture of 4:1. Subsequently, 0.38 ml of 0.12 nM gold nanocuboids solution was added into the mixture and stirred for 30 min. The reaction mixture was washed with CH_3CN:H_2O mixture of 4:1 once and re-dispersed in the same solvent mixture. Finally, 3.0 µl of the mixture was drop-cast onto a silicon nitride membrane (30 nm-thick, S1N1 Agar Scientific) and copper grid.

5.4.6. Functionalization of Gold Nanocubes with PVP: The gold nanocuboids solution was subjected to three times of washing treatment by centrifugation and re-dispersion in order to minimize the concentration of

CTAB surfactant molecules before functionalization. Then, 30 mg/ml of aqueous PVP solution was added into the as-washed nanocubes solution for 2 hours at room temperature. Finally, 3.0 µl of the mixture was drop-casted onto a silicon nitride membrane (30 nm-thick, S1N1 Agar Scientific) and copper grid.

5.4.7. EELS Measurements. Refer to Chapter 4 Section 4.2.2.

5.4.8. Imaging Techniques: The time-lapse TEM images were acquired with high-resolution FEI Titan and JEOL2010FEG transmission electron microscopes operating at 200 kV with electron doses ranging from 100 to 3000 e/(Å^2·s). We imaged at a rate of 10–25 frames per second for the gold nanocubes experiments, 1-2 frames per minute for the silver nanocubes experiments with ORIUS SC200 (Gatan, Inc.) CCD camera.

5.5. References

1. Wang, Y.; Zhou, Y.; Sokolov, J.; Rigas, B.; Levon, K.; Rafailovich, M., A potentiometric protein sensor built with surface molecular imprinting method. *Biosensors and Bioelectronics* **2008,** *24* (1), 162-166.
2. Chen, H.; Heng, C. K.; Puiu, P. D.; Zhou, X. D.; Lee, A. C.; Lim, T. M.; Tan, S. N., Detection of Saccharomyces cerevisiae immobilized on self-assembled monolayer (SAM) of alkanethiolate using electrochemical impedance spectroscopy. *Analytica Chimica Acta* **2005,** *554* (1–2), 52-59.
3. Huang, T. J.; Brough, B.; Ho, C.-M.; Liu, Y.; Flood, A. H.; Bonvallet, P. A.; Tseng, H.-R.; Stoddart, J. F.; Baller, M.; Magonov, S., A nanomechanical device based on linear molecular motors. *Applied Physics Letters* **2004,** *85* (22), 5391-5393.
4. Barfidokht, A.; Ciampi, S.; Luais, E.; Darwish, N.; Gooding, J. J., Distance-Dependent Electron Transfer at Passivated Electrodes Decorated by Gold Nanoparticles. *Analytical Chemistry* **2013,** *85* (2), 1073-1080.

5. Egerton, R. F., Mechanisms of radiation damage in beam-sensitive specimens, for TEM accelerating voltages between 10 and 300 kV. *Microscopy Research and Technique* **2012,** *75* (11), 1550-1556.

6. Sun, J.; Guan, M.; Shang, T.; Gao, C.; Xu, Z.; Zhu, J., Selective Synthesis of Gold Cuboid and Decahedral Nanoparticles Regulated and Controlled by Cu2+ Ions. *Crystal Growth & Design* **2008,** *8* (3), 906-910.

7. Skrabalak, S. E.; Au, L.; Li, X.; Xia, Y., Facile synthesis of Ag nanocubes and Au nanocages. *Nature Protocols* **2007,** *2* (9), 2182-2190.

8. Moran, C. H.; Rycenga, M.; Zhang, Q.; Xia, Y., Replacement of Poly(vinyl pyrrolidone) by Thiols: A Systematic Study of Ag Nanocube Functionalization by Surface-Enhanced Raman Scattering. *The Journal of Physical Chemistry C* **2011,** *115* (44), 21852-21857.

9. Scholl, J. A.; García-Etxarri, A.; Koh, A. L.; Dionne, J. A., Observation of Quantum Tunneling between Two Plasmonic Nanoparticles. *Nano Letters* **2012,** *13* (2), 564-569.

10. Surrey, A.; Pohl, D.; Schultz, L.; Rellinghaus, B., Quantitative Measurement of the Surface Self-Diffusion on Au Nanoparticles by Aberration-Corrected Transmission Electron Microscopy. *Nano Letters* **2012,** *12* (12), 6071-6077.

11. Flüeli, M.; Buffat, P. A.; Borel, J. P., Real time observation by high resolution electron microscopy (HREM) of the coalescence of small gold particles in the electron beam. *Surface Science* **1988,** *202* (1–2), 343-353.

12. Lim, T. H.; McCarthy, D.; Hendy, S. C.; Stevens, K. J.; Brown, S. A.; Tilley, R. D., Real-Time TEM and Kinetic Monte Carlo Studies of the Coalescence of Decahedral Gold Nanoparticles. *ACS Nano* **2009,** *3* (11), 3809-3813.

13. Chen, Y.; Palmer, R. E.; Wilcoxon, J. P., Sintering of Passivated Gold Nanoparticles under the Electron Beam. *Langmuir* **2006,** *22* (6), 2851-2855.

14. Cryoprotection in electron microscopy. *Journal of Microscopy* **1986,** *141* (3), 385-391.

15. Hadermann, J., High-Resolution Electron Microscopy. By John C. H. Spence. Oxford University Press, 2013. Pp. 406. Price [pound sign]75. ISBN: 978-0-19-966863-2. *Acta Crystallographica Section B* **2014,** *70* (4), 778.

16. Williams, D. B. C. C. B., *Transmission Electron Microscopy: A Textbook for Materials Science*. 2 ed.; Springer US: US, 2009.

17. Randolph, S. J.; Fowlkes, J. D.; Rack, P. D., Focused, Nanoscale Electron-Beam-Induced Deposition and Etching. *Critical Reviews in Solid State and Materials Sciences* **2006,** *31* (3), 55-89.

18. Soong, C.; Woo, P.; Hoyle, D., Contamination Cleaning of TEM/SEM Samples with the ZONE Cleaner. *Microscopy Today* **2012,** *20* (06), 44-48.

19. Egerton, R. F.; Li, P.; Malac, M., Radiation damage in the TEM and SEM. *Micron* **2004,** *35* (6), 399-409.

20. Muller, D. A.; Silcox, J., Radiation damage of Ni3Al by 100 keV electrons. *Philosophical Magazine A* **1995,** *71* (6), 1375-1387.

21. Borodko, Y.; Humphrey, S. M.; Tilley, T. D.; Frei, H.; Somorjai, G. A., Charge-Transfer Interaction of Poly(vinylpyrrolidone) with Platinum and Rhodium Nanoparticles. *The Journal of Physical Chemistry C* **2007,** *111* (17), 6288-6295.

22. Love, J. C.; Estroff, L. A.; Kriebel, J. K.; Nuzzo, R. G.; Whitesides, G. M., Self-Assembled Monolayers of Thiolates on Metals as a Form of Nanotechnology. *Chemical Reviews* **2005,** *105* (4), 1103-1170.

23. Li, P. Electron Irradiation Damage to Organic Light-Emitting Materials. University of Alberta, Canada, 2003.

24. Borodko, Y.; Habas, S. E.; Koebel, M.; Yang, P.; Frei, H.; Somorjai, G. A., Probing the Interaction of Poly(vinylpyrrolidone) with Platinum Nanocrystals by UV−Raman and FTIR. *The Journal of Physical Chemistry B* **2006,** *110* (46), 23052-23059.

25. Peniche, C.; Zaldívar, D.; Pazos, M.; Páz, S.; Bulay, A.; Román, J. S., Study of the thermal degradation of poly(N-vinyl-2-pyrrolidone) by thermogravimetry–FTIR. *Journal of Applied Polymer Science* **1993,** *50* (3), 485-493.

Chapter 6

Real-Time Imaging of Chemical Reactions between Silver and Gold Nanoparticles

Abstract: *In this Chapter, a study on the galvanic replacement reaction of silver nanocubes in dilute, aqueous ethylenediaminetetraacetic acid (EDTA)-capped gold aurate solutions using in-situ liquid cell electron microscopy will be demonstrated. Au/Ag etched nanostructures with concave faces are formed via (1) etching that starts from the faces of the nanocubes followed by (2) the deposition of an Au layer as a result of galvanic replacement, and (3) gold deposition via particle coalescence where small nanoparticles are formed during the reaction as a result of radiolysis. Analysis of the silver removal rate and gold deposition rate provides a quantitative picture of the growth process and shows that the morphology and composition of the final product are dependent on the stoichiometric ratio between gold and silver.*

6.1. Introduction

The formation and reaction dynamics during chemical synthesis or transformation of nanoparticles in solution have been widely studied using *ex-situ* methods. A popular method is the so-called ‘quench-and-look’ approach, where the reaction is stopped at various stages, after which the intermediate reaction products are imaged with transmission electron microscopy (TEM). This approach yields detailed information regarding the structure of the (intermediate) reaction products, but early stages of the reaction or fast reactions cannot be tracked. Also unknown is the way in which the sample preparation, i.e., quenching, drop-casting, drying, etc., affects the reaction. These limitations complicate mechanistic studies of structural evolution nanoparticles and related reactions including galvanic replacement, core-shell particle, or the formation of particles with well-defined shapes.

Using *in-situ* imaging in liquid cells mounted inside a TEM, we directly follow in real-time the galvanic replacement reaction between silver nanocubes and chloroauric acid in aqueous medium. We found that this reaction is fast and is completed within minutes, faster than the sample preparation and loading time of ~5 minutes, preventing the observation of the early stages of the reaction. Adding the chelating ligand ethylenediaminetetraacetic acid (EDTA) to the reaction mixture prior to the addition of the silver nanocubes made it possible to follow the reaction over a longer (7-10 minutes) period of time because EDTA is able to form complexes with gold ions.

In this Chapter, we show a new mechanistic pathway where the aurate etched the silver nanocubes' faces, making them bowl-shaped, while simultaneously a layer of gold was deposited onto the silver cube as a result of galvanic replacement. In parallel, gold was also deposited *via* coalescence and monomer attachment as small gold nanoparticles formed during the reaction as a result of radiolysis. These results help to understand the mechanisms of nanoparticle growth by galvanic replacement reactions, where the morphology and composition are governed by a subtle change in local stoichiometry, which is useful for field of material engineering and metallic microscopic corrosion.

Galvanic replacement reactions are based on the principle that metal ions with higher oxidation potentials undergo reduction by oxidizing the metal present on the nanoparticles.[1-5] In this study, we focus on the galvanic replacement between Ag nanocubes and aurate for which the following mechanism has been proposed by Sun *et al.*[1] The standard reduction potential of $AuCl_4^-$/Au (0.99 V *vs.* standard hydrogen electrode, SHE) and $AuCl_2^-$/Au (1.11 V *vs.* SHE) is higher than that of Ag^+/Ag (0.80 V *vs.* SHE) and consequently, the galvanic replacement of Ag by Au (Eq. 1 and 2) is thermodynamically favorable and spontaneous.

$$3Ag\ (s) + AuCl_4^-\ (aq) \rightarrow Au\ (s) + 3AgCl\ (s) + Cl^-\ (aq) \qquad \text{(Eq. 1)}$$

$$Ag\ (s) + AuCl_2^-\ (aq) \rightarrow Au\ (s) + AgCl\ (s) + Cl^-\ (aq) \qquad \text{(Eq. 2)}$$

Sun *et al.*[1] identified three distinct steps in the reaction of silver nanostructures with chloroauric acid ($HAuCl_4$) by *ex-situ* TEM imaging: first, pinholes form in the silver nanocubes *via* etching of the Ag by the gold aurate, then the silver nanocubes dissolve and an Au-Ag alloy forms on the walls of the cubes. Finally, the particles de-alloy followed by growth of the Au layer at the expense of the Ag till finally the hollow Au structures are formed (i.e., hollow nanocages). Moreover, Au *et al.*[6] investigated the effect of the reaction stoichiometric ratio by replacing the $AuCl_4^-$ with $AuCl_2^-$. They reported that Ag cubes reacting with $AuCl_2^-$ at an early stage produce nanoboxes and eventually form nanoframes without the dealloying step. They observed a molar ratio of 1:1 between generated Au and consumed Ag, i.e., more gold was deposited per oxidized Ag atom in the reaction with $AuCl_2^-$ than in the reaction with $AuCl_4^-$.

In order to understand the dynamic processes of galvanic replacement, high-resolution imaging and quantitatively analyzing the morphological and structural changes of the Ag cubes in this galvanic replacement reaction are needed.

6.2. Results & Discussion

6.2.1. The Attempt to Slow Down the Reactions

Refer to the Chapter 3 Section 3.2.2 for synthesis of the silver nanocubes used in this Chapter. The experimental detail of the synthetic procedures is reported in the experimental section at end of Chapter 3.

To investigate the mechanism of the galvanic replacement reaction of Ag by aurate, we used a combination of *in-situ* TEM imaging and *ex-situ* characterization techniques such as post-mortem TEM imaging, energy-dispersive X-ray spectroscopy (EDX), scanning TEM (STEM)-tomography, etc., to study the structure, morphology and composition variation of the nanostructures in detail. For the *ex-situ* measurements, we typically added 5 µl of 10 mM $HAuCl_4$ at once to react with a 1 ml ~0.7 nM Ag nanocube suspension, following the reaction kinetics by UV/Vis spectroscopy. The absorbance value of the Ag nanocube suspension at a wavelength of 419 nm dropped by 80% of its initial value within one minute. Since the time required to inject the reaction mixture into the liquid cell, mount the liquid cell into the TEM, and start imaging is ~5 minutes, we could not observe the early stages of the reaction. To lower the reaction rate, we added the chelating ligand ethylenediaminetetraacetic acid (EDTA) that readily binds to metal cations.[7] At the same volume ratio of $HAuCl_4$ and Ag nanocubes as stated above, the reaction was slowed down in the presence of 10 mM EDTA where the absorbance value of the Ag nanocube suspension decreased merely 20% of its initial value within one minute.

Figure 6.1 (a) shows the UV-vis spectra of Ag nanocubes solution before (green curve) and after interacting with gold ions solution with EDTA (red curve) and without EDTA (black curve) while Figure 6.1 (b) shows the plot of intensities versus time. In the absence of EDTA, the absorbance value at 419 nm dropped to ~20% of its initial value within 2 minutes. With EDTA, absorbance value at 419 nm dropped to ~80% of its initial value within 2 minutes. This proves that EDTA plays a role in slowing down the reaction rate between silver nanocubes and gold ions.

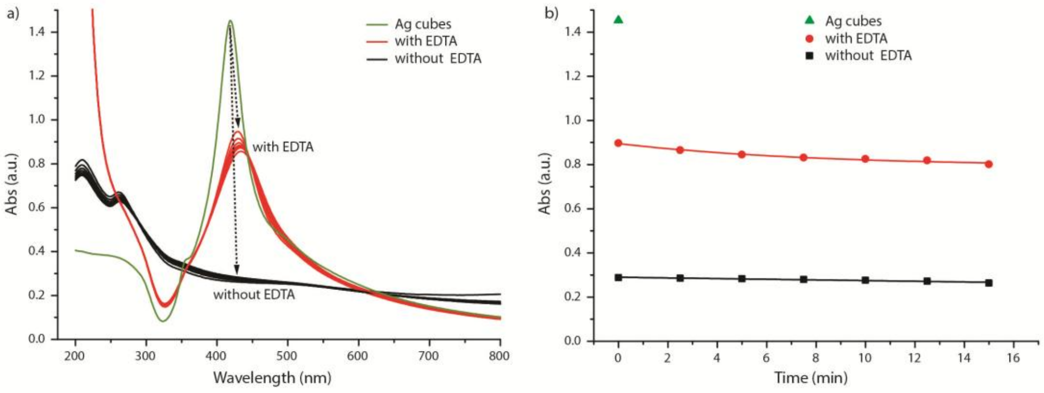

Figure. 6.1 (a) UV-vis spectra of Ag nanocubes solution before (green curve) and after interacting with gold ions solution with EDTA (red curve) and without EDTA (black curve). (b) The plot of absorbance intensities versus time. Each spectrum was recorded every 2 minutes.

6.2.2 *In-Situ* Observation of Galvanic Replacement Reactions

Figure 6.2 (a) shows a time (t, in s) series of TEM images from a single Ag nanocube reacting with the gold aurate solution inside a liquid cell. The EDTA-capped gold ions etch the faces of the Ag nanocube, resulting in bowl-shaped faces. Figure 6.2 (b) illustrates this process schematically. At t = 0 s, the Ag nanocubes and small particles (encircled in red) are visible. As the small nanoparticles were repelled from the electron beam too fast for analysis at the dry state, we were not able to measure their chemical composition but we suggest that these are small Au nanoparticles that formed *via* radiolysis (i.e., reduction of Au^{3+} by solvated electrons). The image recorded at t = 4.7 s, and the subsequent images, show that one of these nanoparticles slowly disappears. We propose that the small Au nanoparticles disappear and that the Au is deposited on Ag cubes *via* particle coalescence and a monomer attachment process. In addition, these images show that the volume of the nanocube increases during the reaction (indicated by the red and green arrows).

Figures 6.2 (c) and (d) show the evolution of the particle volume V (in nm^3) which is associated with the removal of silver and deposition of gold for five particles as a function of the reaction time (see Section 6.4 for volume estimation details). We observe two time domains with distinct reaction kinetics: from t = 0 s to t = 6 s (blue colour region) and from t = 7 s to t = 14 s (red colour region), we fitted all five curves to an exponential function, with the volume depletion or growth equal to Eq. 3.

$$V = V_0 e^{-kt}, \qquad \text{(Eq. 3)}$$

where V_0 is the initial volume of the nanocube (nm^3) and k is the rate constant (s^{-1}). The dotted lines represent fits to Eq. 3. For all five data sets from t = 0 s to *t* = 6 s (blue color region), simple exponential regression estimates *k* to be -0.02 ± 0.01 s^{-1} for silver removal and 0.12 ± 0.09 s^{-1} for gold deposition. The indicated errors represent the standard deviation from five independent measurements.

The order of the reaction tells us how the rate of the reaction varies with respect to the reactant concentration. Overall, the reaction order is two (first order with respect to silver nanocubes and gold aurate). For both regions, the rate of removal of Ag and deposition of Au show linearly dependent on the silver nanocube and aurate concentration respectively. Although the removal rate of silver is expected to be faster than the deposition rate of gold since the estimated molar ratio of gold deposition versus silver removal, M_{Ag}:M_{Au} would be 3:1, according to the Eq. 1, three equivalents of Ag atoms are required to reduce one equivalent of Au^{3+} to metallic Au. However, our results show that the rate constant ratio of Ag:Au is 1:5.9 where the deposition rate of gold is faster than the depletion rate of silver. This also explains in our experiments the absence of pinholes which serve as a pit for silver removal, as reported elsewhere.[6] In our experiment, the silver removal is much slower than the gold deposition due to three factors: the electron beam, the presence of EDTA and the presence of Ag atoms in the galvanic replacement reaction. For the time domain *t* = 7 s to *t* = 14 s (red coloured region), k is calculated to be -0.015 ± 0.01 s^{-1} for silver removal and 0.05 ± 0.01 s^{-1} for gold deposition. Our results show that the rate constant ratio of Ag: Au is 1.3.5 where the deposition rate of gold is faster than the depletion rate of silver, similar to the first time interval.

We attribute this discrepancy in molar ratio to the two reactions that happen in parallel: galvanic replacement and growth of a gold layer *via* particle coalescence and monomer attachment process. We believe that the excessive gold deposition results in the formation of gold nanoparticles *via* reduction of $AuCl_4^-$ to Au^0 through radiolysis.[8] This hypothesis also explains the formation of the small Au nanoparticles shown in Figure 6.2 (a) as described above. In addition, the solvated electrons readily reduce Au^{3+} to Au^+, thereby changing the stoichiometric ratio in Eqs. 1 and 2.

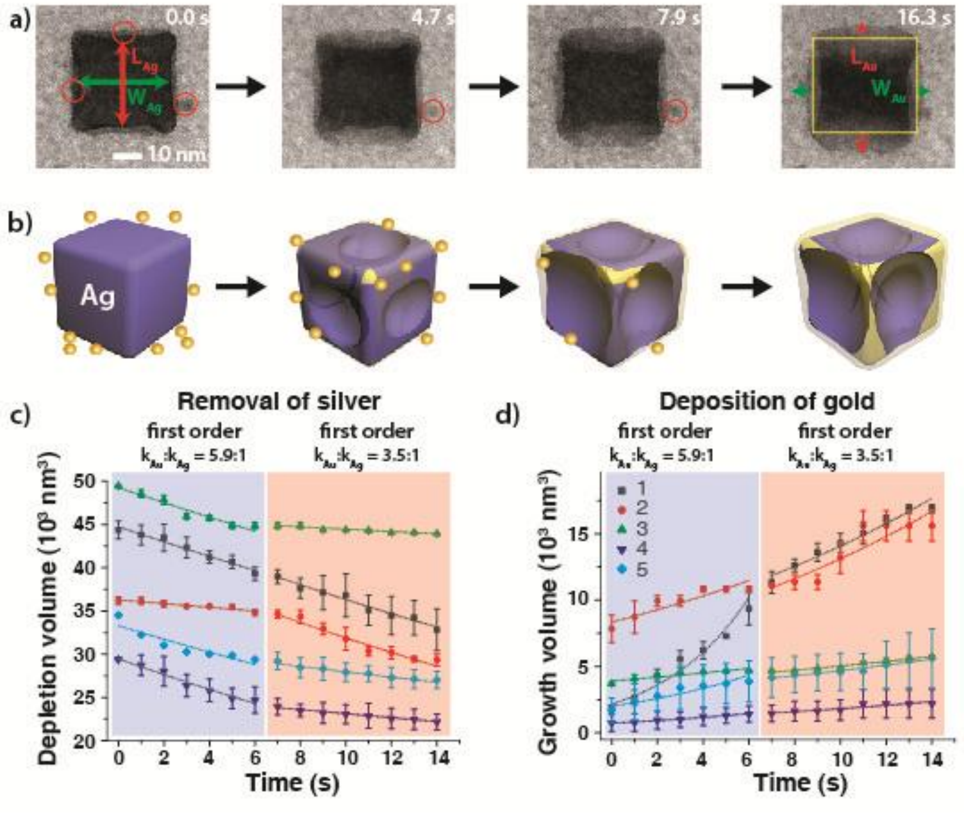

Figure 6.2 (a) Time-lapse TEM images showing a silver nanocube interacting with the gold aurate solution inside a liquids cell. (b) Schematic of the galvanic replacement reaction between silver nanocubes and EDTA-capped gold ions solution. Evolution of the particle volume depletion/growth rate as a function of time: (c) removal of silver and (d) deposition of

gold. Blue color region indicates faster initial reaction kinetics in comparison with the later red color region.

6.2.3. The Role of EDTA ligands

The TEM images in Figure 6.3 (a) and (c) show the control experiments of silver nanocubes performed with and without EDTA-capped gold ions solution respectively. The silver nanocubes were transformed into porous (*alloy*) nanocages without the presence of EDTA. In the presence of EDTA, the silver nanocubes were etched from the edges, a layer of gold was deposited surrounding the nanocube during the galvanic replacement reaction as shown in Figure 6.3 (c). Without the presence of chloroauric acid, EDTA itself is unable to induce any chemical reaction, therefore the nanocubes still maintain its shape as shown in Figure 6.3 (b).

In order to investigate the role of EDTA in this gold-silver galvanic replacement reaction, the EDTA and chloroauric solutions were mixed for 5, 8, and 10 minutes, before subsequent addition of silver nanocubes solution. Different extent of *etching* of silver nanocube was observed for different reaction times of EDTA with gold ions as shown in Figure 6.3 (d), (e) and (f). The extent of etching is the less when the reaction time between EDTA and gold ions is longer and vice versa. From this observation, the we conclude that the chelating behavior of EDTA to gold ions is significant.

We prepared the SEM samples by spinning down the silver nanoparticles suspension with centrifuge after reacting with EDTA-capped gold ions aqueous solution for 30 minutes, and subsequently spin-coated them onto a silicon wafer substrate. Unlike the previously reported isolation method[2] where they treated the suspension with NaCl in order to get rid of AgCl before centrifugation. However, due to the limitation of SEM technique, we are not able to resolve those etched particles.

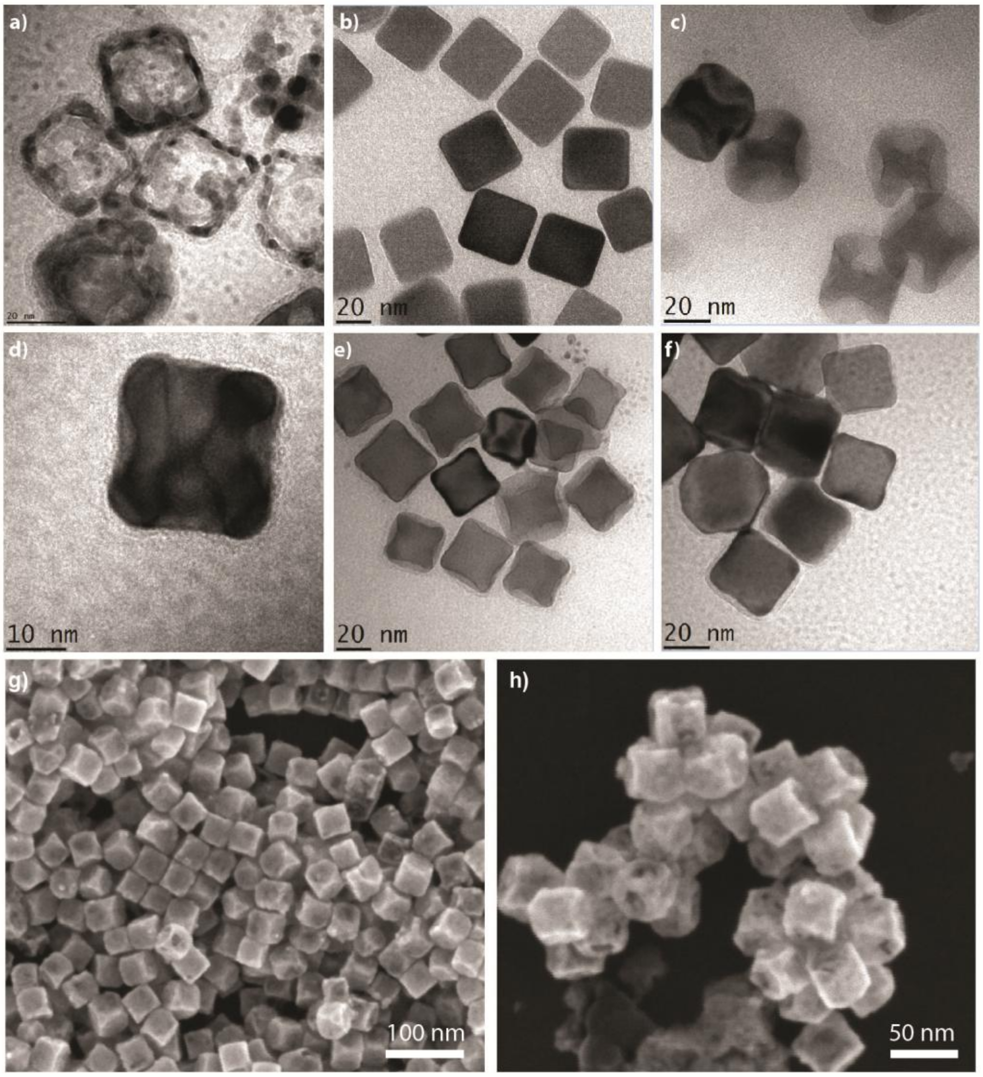

Figure 6.3 TEM images of silver nanocubes after reacting with (a) $HAuCl_4$ gold precursor solution (b) EDTA aqueous solution. (c) EDTA-capped gold ions solution for 8 minutes, while (c-f) show the nanostructures where EDTA capped gold ions for different reaction times: (d) 5 minutes (e) 8 minutes and (f) 10 minutes respectively. (g) and (h) SEM images of silver nanocubes after reacting with EDTA-capped gold ions solution for 8 minutes.

6.2.4. Energy-Dispersive X-Ray Spectroscopy

To study the structure of the nanoparticle before and after galvanic replacement reaction, we drop-casted nanoparticle suspensions onto the TEM grids. The low magnification TEM images in Figure 6.4 show the structure of the Ag nanocubes before (a) and after (b) reacting with EDTA-capped gold ions solution. Figure 6.4 (c) and (d) show the TEM images of a single Ag nanocube before and after interacting with EDTA-capped gold ions solution respectively, and the insets show the electron diffraction patterns of those individual nanostructures. Figure 6.4 (e) shows a high resolution TEM image of the particle. The electron diffraction patterns suggest that the Ag nanocubes are single crystals with {100} facets before interacting with the EDTA-capped gold ions solution, similar to what has been reported by Sun *et al*.[1] The crystallinity of the nanocubes is preserved after interacting with EDTA-capped gold ions solution.

To discriminate between the Au and Ag, we used STEM-EDX for the following reason. The lattice parameters of Au and Ag are nearly identical resulting in indistinguishable diffraction patterns. In contrast, EDX is element specific and readily allowed us to map the elemental composition of the nanoparticle using STEM-EDX.[9] Figure 6.4 (f-i) shows a STEM image and the corresponding EDX maps from a single particle. The results indicate that the final nanostructure consists of Ag and inhomogeneously distributed Au. The EDX line-scan in Figure 6.4 (j) suggests that the gold is mainly deposited at the edges of the structures, covered like a shell on the etched nanocubes. The atomic percentages of Ag and Au that extracted from the EDX map are 97 ± 1 and 3 ± 1 %.

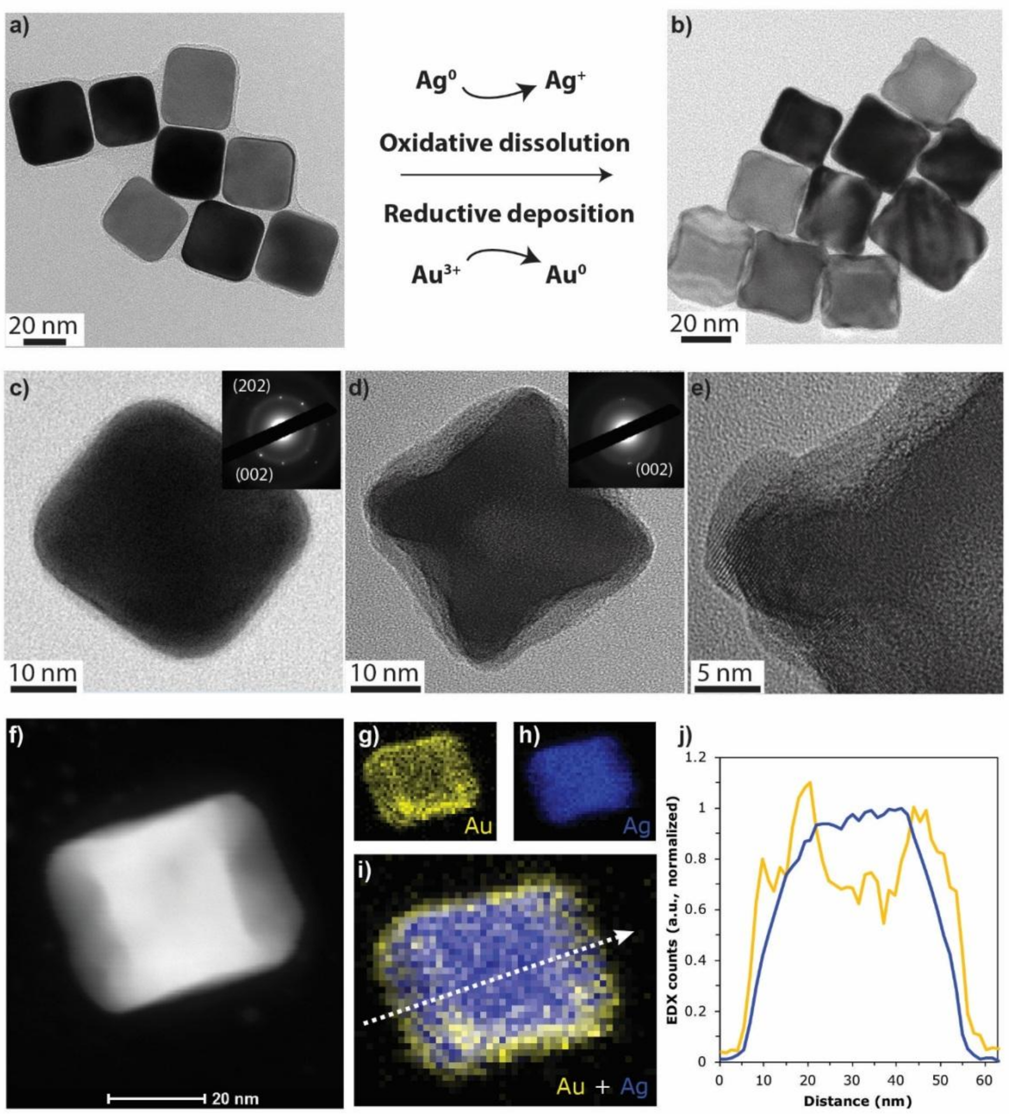

Figure 6.4 Low magnification TEM images of Ag nanocubes (a) before and (b) after reacting with EDTA-capped $HAuCl_4$ aqueous solution. HRTEM images of an Ag nanocube (c) before and (d and e) after reacting with EDTA-capped $HAuCl_4$ aqueous solution. The insets show the corresponding diffraction pattern. (f) HAADF-STEM image and (g-i) the corresponding STEM-EDX maps of an individual Ag/Au nanostructure. Note that (g) and (h) show the EDX signal for Ag and Au respectively, while (i) displays the signal for Au and Ag simultaneously. (j) EDX line-scan profiles of the same structure. The yellow line plots the relative counts for Au (yellow) and Ag (blue) along the white arrow in panel (i). (**j**) EDX line-scan profiles of the same structure. The yellow line plots the relative counts for Au (yellow) and Ag (blue) along the white arrow in panel (i).

6.2.5 3D STEM Tomography

To further characterize the final structure of the etched nanocube, 3D STEM tomography was conducted, providing a 3-dimensional view of this structure.[10] We tilted the substrate with the etched nanocube from -70° to 70° with respect to the horizontal axis of the nanocube. We brought the series of images to one rotation axis by aligning all images accurately and reconstructed a 3D volume over 58 STEM images. The reconstructed 3D volume in Figure 6.5 (b) shows concave faces on the silver nanocube, while the whole structure remains solid.

In addition, the x-y slice extracted from the 3D volume in Figure 6.5 (a) reveals that the edges and part of the faces appear brighter (having higher intensities), as indicated by red circles. It is known that the intensity in HAADF-STEM images scales with the atomic number of the elements present in the sample: Ag (47) and Au (79).[11] This is consistent with our EDX observation in Figure 6.4 (i) where the gold layer was deposited at the edges and surfaces of the Ag nanocube.

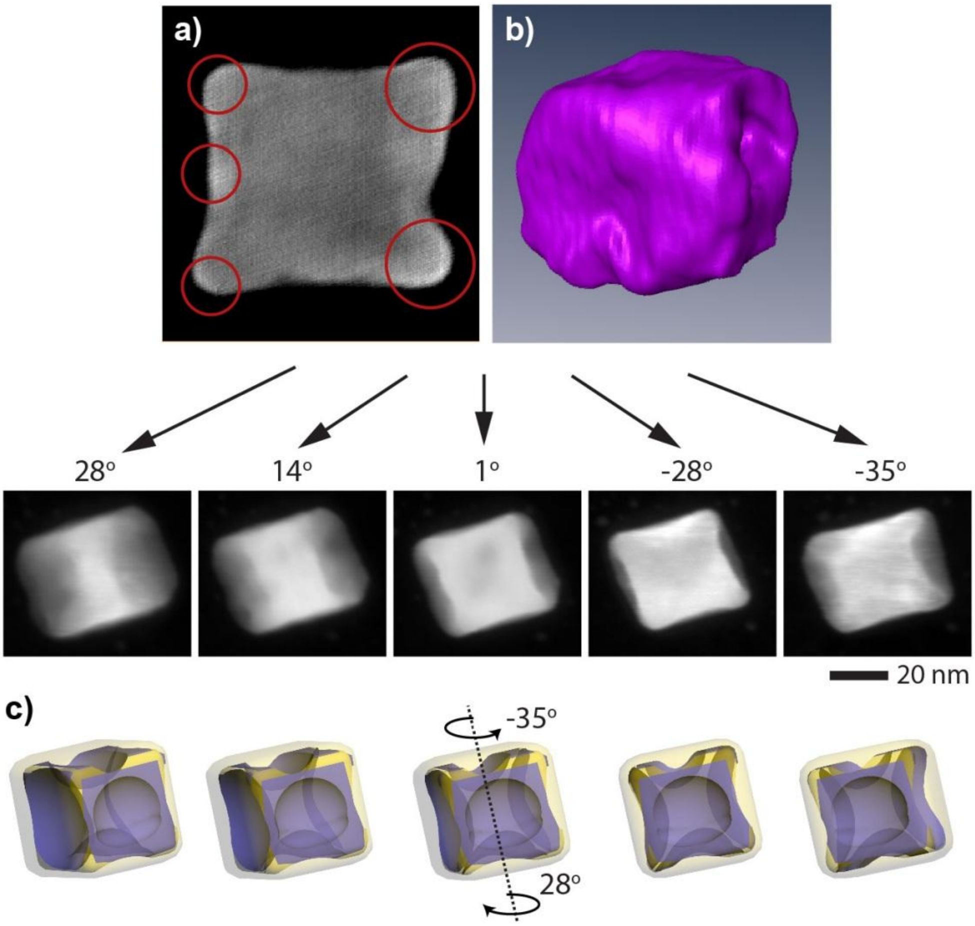

Figure 6.5 HAADF-STEM tomography images of an individual nanostructure where the substrate was tilted from -70° to 70°. (a) A reconstructed x-y slice extracted from the 3D volume in (b). (c) Schematic illustration showing the top and side view of the above structure.

6.3. Conclusions

We observed a different mechanistic pathway where an etching process starts from the faces of the nanocubes followed by gold deposition together with particle coalescence and monomer attachment process, finally lead to a bowl-shaped etched Au/Ag nanostructure. The use of chelating ligands EDTA makes it possible to quantitatively analyze the chemical reactions while they happen. We extracted all the reaction kinetics from the dynamics that we observed inside the *in-situ* TEM liquids cells and the final structure shows good agreement with the *ex-situ* characterization techniques such as EDX and 3D STEM Tomography. By using TEM liquids cells, we are able to conduct a quantitative analysis on single particle dynamics which offer us a way to determine the rate of silver removal and gold deposition at the nanoscale.

Our results will provide insights into the field of metallic microscopic corrosion and nanoparticle growth by galvanic replacement reaction, where a subtle change in stoichiometric ratio could lead to a huge difference in morphology and composition, thereby tuning the structural properties of the nanomaterials which will be important for material engineering in nanofabrication.

6.4. Experimental Section

6.4.1. General Procedures. We purchased the chemicals: poly(vinyl) pyrrolidone, silver nitrate, gold (ш) chloride trihydrate ($HAuCl_4$) and ethylenediaminetetraacetic acid disodium salt dihydrate (EDTA) from Sigma-Aldrich, sodium sulfide and ethylene glycol from J.T. Baker, all chemicals were used without further purification with glass vials from Fisher Scientific. We soaked all the stirrer bars in aqua-regia (mixture of 3:1 volume ratio of nitric acid: hydrochloric acid) for at least 1 hour, washed with deionized water (18.2 MΩ·cm), and dried them in an oven at 80-120° Celcius before use. We washed the nanoparticles with centrifuges of the brand Rotina (380R) and Profuge (14D). The UV/Vis spectra were recorded on a UV/VIS/NIR spectroscope (PerkinElmer Lambda 750), measuring the light transmission through a cuvette of 1 cm light-path.

6.4.2. Synthesis of Silver Nanocubes.

Refer to Chapter 3 Section 3.4.

6.4.3. *In-situ* Imaging Techniques: We pre-mixed the 5 µl of 10 mM $HAuCl_4$ aqueous solution with 900 µl of 10 mM EDTA aqueous solution for 8 minutes. Subsequently, we added 100 µl of as-prepared silver nanocubes solution into the mixture. We loaded approximately 400 nL of the resulting solution into a liquid cell, which is comprised of two ultrathin (∼14 nm) electron translucent SiN_x membranes separated by ∼200 nm with spacers. Prior to solution loading, these liquid cells were oxygen plasma treated to make their SiNx membrane surfaces hydrophilic. Each liquid cell, sealed with a copper gasket, is inserted into the TEM using a specimen holder. We used a JEOL 2010FEG TEM operated at 200 kV for in situ imaging with electron doses ranging from 2000 to 5000 e/($Å^2$·s). We imaged at a rate of 10−25 frames per second with ORIUS SC200 (Gatan, Inc.) CCD camera.

6.4.4. Volume Estimation (Particle in Figure 6.2):

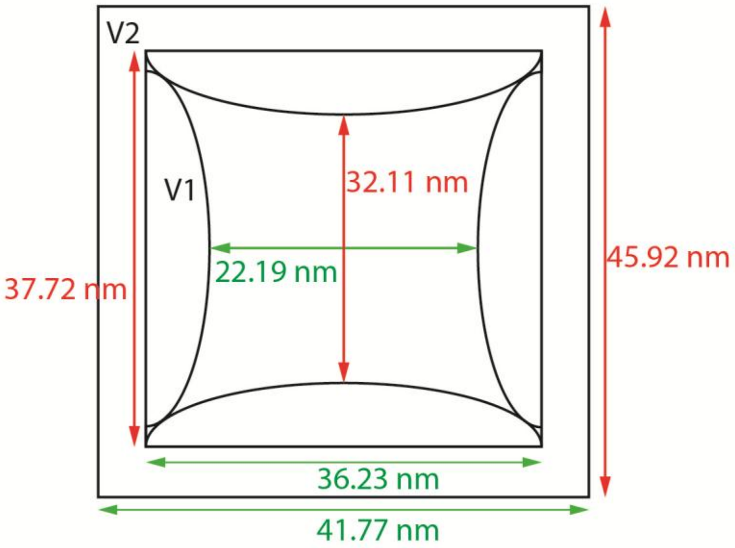

Average edge length of cube = 36.97 nm

Volume of a spherical cap:

$$V = \frac{\pi h}{6}(3a^2 + h^2)$$

$$a = \frac{36.97\ nm}{2} = 18.49\ nm$$

$$h1 = 36.97 - \frac{(32.11 + 22.19)nm}{2} = 4.91\ nm$$

$$V1 = \frac{\pi h1}{6}(3a^2 + h1^2)$$

$$V1 = \frac{\pi(4.91\ nm)}{6}[3(18.49\ nm)^2 + (4.91\ nm)^2] = 2698.74\ nm^3$$

$$V_{Ag} = 36.97^3 - 6\ (V1) = 34350.05\ nm^3$$

$$V2 = \left[\frac{(45.92 + 41.77)}{2}\right]^3 - [36.97]^3 = 33757.04\ nm^3$$

$$V_{Au} = (V2)/2 = 16883.91\ nm^3$$

6.5. References

1. Sun, Y.; Xia, Y., Shape-Controlled Synthesis of Gold and Silver Nanoparticles. *Science* **2002,** *298* (5601), 2176-2179.
2. Skrabalak, S. E.; Au, L.; Li, X.; Xia, Y., Facile synthesis of Ag nanocubes and Au nanocages. *Nature Protocols* **2007,** *2* (9), 2182-2190.
3. Chen, J.; Wiley, B.; McLellan, J.; Xiong, Y.; Li, Z.-Y.; Xia, Y., Optical Properties of Pd−Ag and Pt−Ag Nanoboxes Synthesized via Galvanic Replacement Reactions. *Nano Letters* **2005,** *5* (10), 2058-2062.
4. Sun, Y.; Xia, Y., Mechanistic Study on the Replacement Reaction between Silver Nanostructures and Chloroauric Acid in Aqueous Medium. *Journal of the American Chemical Society* **2004,** *126* (12), 3892-3901.
5. Xia, X.; Wang, Y.; Ruditskiy, A.; Xia, Y., 25th Anniversary Article: Galvanic Replacement: A Simple and Versatile Route to Hollow

Nanostructures with Tunable and Well-Controlled Properties. *Advanced Materials* **2013,** *25* (44), 6313-6333.

6. Au, L.; Lu, X.; Xia, Y., A Comparative Study of Galvanic Replacement Reactions Involving Ag Nanocubes and AuCl2− or AuCl4−. *Advanced Materials* **2008,** *20* (13), 2517-2522.

7. F. Danil de Namor, A.; Alfredo Pacheco Tanaka, D., Thermodynamics of protonation and complexation of EDTA derivatives and metal cations in water. *Journal of the Chemical Society, Faraday Transactions* **1998,** *94* (20), 3105-3110.

8. Sutter, E. A.; Sutter, P. W., Determination of Redox Reaction Rates and Orders by In Situ Liquid Cell Electron Microscopy of Pd and Au Solution Growth. *Journal of the American Chemical Society* **2014,** *136* (48), 16865-16870.

9. Shahjamali, M. M.; Salvador, M.; Bosman, M.; Ginger, D. S.; Xue, C., Edge-Gold-Coated Silver Nanoprisms: Enhanced Stability and Applications in Organic Photovoltaics and Chemical Sensing. *The Journal of Physical Chemistry C* **2014,** *118* (23), 12459-12468.

10. Goris, B.; Polavarapu, L.; Bals, S.; Van Tendeloo, G.; Liz-Marzán, L. M., Monitoring Galvanic Replacement Through Three-Dimensional Morphological and Chemical Mapping. *Nano Letters* **2014,** *14* (6), 3220-3226.

11. Pennycook, S. J.; Jesson, D. E., High-resolution incoherent imaging of crystals. *Physical Review Letters* **1990,** *64* (8), 938-941.

Chapter 7

Real-Time Imaging of Au@Ag Core-Shell Nanoparticles Formation

Abstract: *We studied the overgrowth process of silver on gold nanocubes in dilute, aqueous silver nitrate solution in the presence of reducing agent, ascorbic acid using in-situ liquid cell electron microscopy. Au@Ag core-shell nanostructures were formed via two mechanistic pathways: (1) nuclei coalescence where the silver nanoparticles absorbed onto the gold nanocubes and (2) monomer attachment where the silver atoms epitaxially deposited onto the gold nanocubes. Both patways lead to the same Au@Ag core-shell nanostructures. Analysis of the silver deposition rate reveals the growth modes of this process and show that this reaction is chemically-mediated by the reducing agent, ascorbic acid.*

7.1. Introduction

Core-shell nanoparticles are highly functionalized nanoparticles with distinctive properties that originate from different materials. The properties of the core-shell nanoparticles can be tuned by either the constituting materials or the core to shell ratio.[1] This tunability makes it possible to manipulate the surface properties so as to meet the requirements for a range of applications. including biomedical,[2] pharmaceutical,[3] catalysis,[4] electronics,[5] enhancing photoluminescence,[6-7] etc. The advantages of coating on the core particle over surface modification of nanoparticles are many-fold and core-shell nanoparticles have improved functionality, stability, dispersibillity, than the surface modified particles. Furthermore, core-shell nanoparticles are also used in applications requiring controlled released of the core to form hollow nanostructures, reduction in consumption of precious materials.[8]

The fabrication of core-shell nanoparticles with different morphology and composition can be accomplished by various chemicals means such as solution phase reduction[9-10] and physical methods such as wire electrical explosion followed by the ultrasonic irradiation.[11] Fine-tuning of the surface structure, i.e., the dominant crystalline facets and surface composition, is important for applications such as catalysis and can be accomplished with the addition of different chemical additives.[12] For instance, whether {111} or {100} facets dominate on the Ag shells is determined by the presence of chemical additives poly (vinyl) pyrrolidone (PVP), *N*,*N*-dimethylformamide (DMF) and ethylene glycol (EG).[12] In general, the synthesis parameters are derived empirically and the final nanoparticle morphology is confirmed with the so-called ‘quench-and-look’ approach, where the reaction is stopped at various stages, after which the intermediate reaction products are imaged with techniques such as transmission electron microscopy (TEM). However, early stages of the reactions and intermediate structures cannot be investigated this way. As such, the interplay of different chemical additives, such as surfactants and reducing agents, remain largely unresolved. Clarification of these questions is important to understand how processes such as atom deposition and surface diffusion in dictating the evolution of a seed into nanocrystals of various shapes.

For chemically-synthesized Au@Ag cubic core-shell nanoparticles, Xia and co-workers[13] reported that the Au cubes tend to nucleate and grow homogeneously on six low-index (100) planes of the cubic seeds when a strong reducing agent ascorbic acid (AA) was used. They attributed the observation to fast reducing kinetics by AA which promote the formation of {100} in the presence of bromide ions from the surfactants, cetyltrimethylammonium bromide (CTAB). There are also studies suggested that the overgrowth is promoted by the presence of the Br^- ions.[9-10, 14] Previously reported studies[9, 12-13, 15-16] have suggested the size of the shell is dependent on the ratio of precursor, reducing agent and size of the core. Under conditions of increased precursor and reducing agent, the Ag prefers continue growing on the Ag overgrowth rather than to homonucleate in the solution as heterogeneous nucleation and growth is generally more favorable than homogeneous nucleation as a result of lowered free energy barrier.[17]

Moreover, Xia *et al.*[18] has also proposed the final product of the overgrowth reaction is determined by the ratio between the rates of atom deposition ($V_{\text{deposition}}$) and surface diffusion ($V_{\text{diffusion}}$). The stable shape of the resultant nanostructure will depend on the presence of capping agents to stabilize the enlarged high energy facets, the lack of which will lead to the nanostructure adopting the thermodynamically favoured shape. However, it is still ambiguous how the atoms get deposited onto the surface of a seed and migrated to other sites of the surface, leading to the formation of diversified shape of the shell. Moreover, there is little experimental verification of these mechanisms of overgrowth due to the difficulties in probing the earlier stages of growth as mentioned in the previous paragraph.

In this Chapter, we studied the formation of Au@Ag core-shell nanocubes, which had been shown to possess excellent and tunable plasmonic properties[9-10, 16], using liquid cell transmission electron microscopy. We used a synthesis recipe similar to the cited work to fabricate these nanostructures with the following differences. (1) The Au seeds are subjected to washing procedure in order to minimizing the surfactants concentration before introducing into the liquid cell. (2) The Au seeds are drop-casted on one half of the liquid cell prior to assembly and silver nitrate solution introduced *via* the flow tubing after loading the holder in to the TEM. (3) The experiments are carried out at room temperature. The *in-situ* results are also compared against nanocubes that we synthesized on the laboratory bench (Section 7.2.3 for details). Surprisingly, we found that our initial strategy of using the electron beam as substitute for a reducing agent did not work for the growth of the Au@Ag core-shell nanocubes.

7.2. Results & Discussion

7.2.1. The Reducing Agent: Electron Beam

In-situ electron microscopy with liquid cells is an emerging technique for elucidating the mechanisms of nanostructure formation.[19-21] It is also well-known that the electron beam itself can act as a reducing agent and reduce metal ions into atoms through the action of solvated electrons (from radiolysis of water). This effect has been exploited for dynamical studies of silver[22-23] nanoparticle nucleation directly from solution. Recently, Jungjohann *et al.*[15]

and Wu *et al.*[16] demonstrated the use of in-*situ* liquid cell microscopy to study the solution growth of Au@Pd and Pt@Au core-shell nanoparticles, respectively. In both studies, the electron beam replaces the reducing agent, leading to metal deposition.

Figure 7.1 shows typical structures that were formed when silver nitrate was introduced to Au cubes in the absence of L-ascorbic acid (using electron beam as reducing agent). We did not observe the Au@Ag core-shell nanostructures formation under electron beam irradiation. When Ag clusters attach to the Au cuboids, they attach randomly and develop into ramified structures. They did not merge into a conformal layer but tend to have dendritic growth (red arrows).

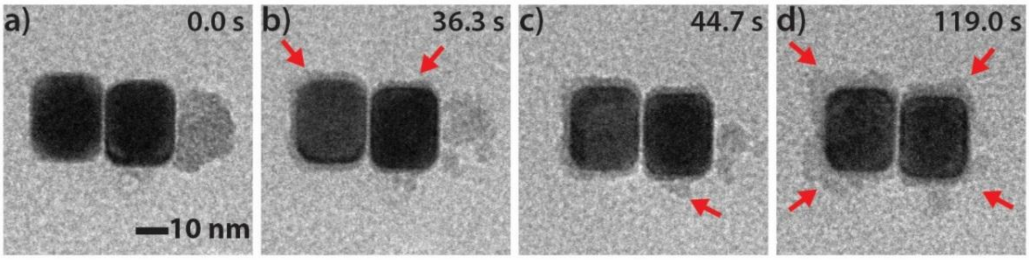

Figure 7.1 (a-d) Time-lapse TEM images showing two gold nanocubes interacting with the silver nitrate aqueous solution in the absence of L-ascorbic acid inside a liquid flow cell.

7.2.2. The Role of Chemical Additives: Ascorbic Acid

In subsequent experiments, we reverted back to conventional recipe by pre-mixing the gold nanocubes with a reducing agent of L-ascorbic acid (AA) before introducing the silver precursor solution into the mixture. Figure 7.2 (a-e) shows time-lapsed TEM images of Au@Ag core-shell nanocubes that were observed *in-situ*. In this case, the shell formation is conformal and homogeneous instead of randomly attachment as seen in figure 7.1. Moreover, these core-shell nanostructures are similar in terms of morphology to those prepared *ex-situ* (Figure 7.2 f). *In-situ* observations and *ex-situ* TEM diffraction result also show that growth of the Ag layer results in the development of {110} facets (Figure 7.2 a), in agreement with core-shell nanoparticles synthesized on the laboratory bench. The measured shell thicknesses are indistinguishable for the Au@Ag nanostructures prepared by *in-situ* (7 ± 3 nm) and *ex-situ* (7 ± 3 nm) methods as shown in the histogram. Due to the similarities, we believe that while the electron beam can reduce silver nitrate and it does not promote the overgrowth reaction.

Furthermore, our results do not agree with overgrowth model promoted by the halide ions as mentioned in the introduction. The Au nanocubes that were used in our experiments have been washed and there should be little residual CTAB left in solution. The lack of available CTAB is also evidenced by the Au nanocubes gradually changing their shapes with time after washing (Figure 7.3). Therefore, initial formation of the Ag layer is due to the presence of AA. Given that there was also no overgrowth when the electron beam was used as a reducing agent, we suggest that ascorbic acid plays a previously unknown role of guiding the overgrowth of silver.

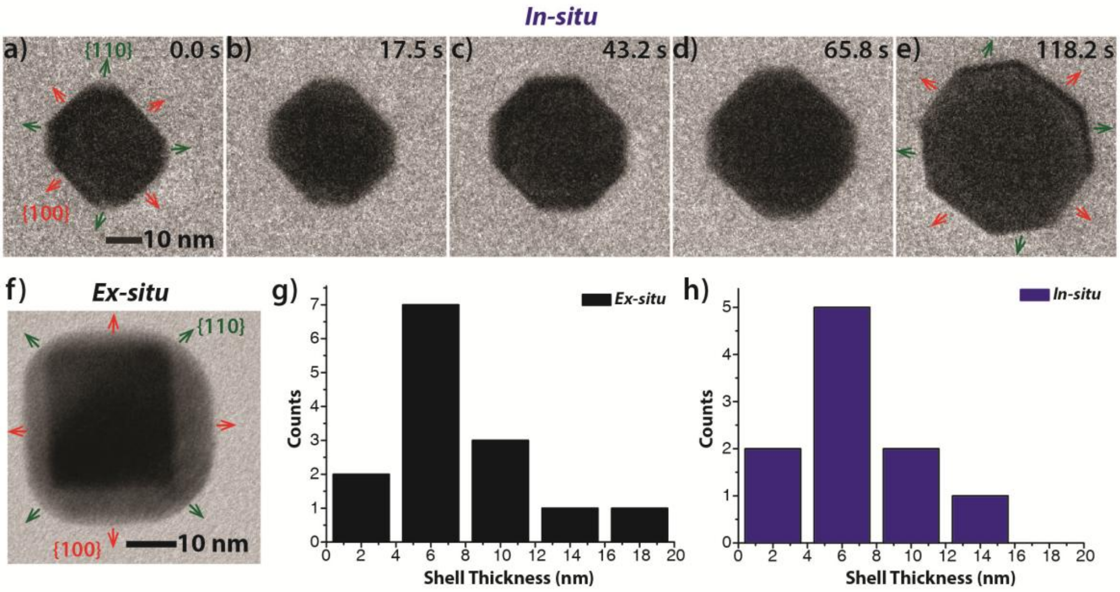

Figure 7.2 (a-e) Time-lapse TEM images showing a gold nanocube interacting with the silver nitrate aqueous solution in the presence of L-ascorbic acid (AA) inside a liquid flow cell. (f) TEM image of *ex-situ* prepared Au@Ag core-shell nanostructures with addition of AA. Histograms of Au@Ag core shell nanoparticles that are prepared by (g) *ex-situ* (h) *in-situ* methods respectively.

Figure 7.3 shows the TEM images of the aged gold nanocubes (aging time: ~ 2 hours) after the washing procedure. The corners of the nanocubes start to turn round, and eventually become quasi-spherical gold nanoparticles.

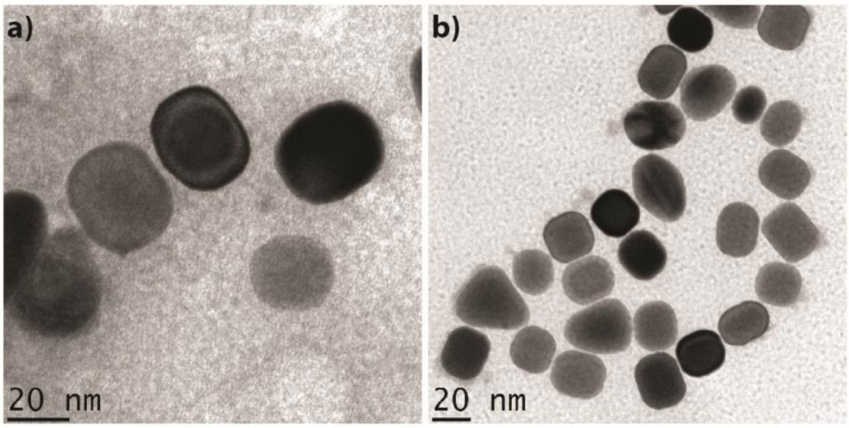

Figure 7.3 TEM images of aged nanocubes at room temperature, ~2 hours after the washing procedure.

7.2.3. *Ex-Situ* Characterization

Figure 7.4 show the TEM images of the *in-situ* prepared Au/Ag nanostructures after reacting with silver nitrate solution without (a) and with (b) ascorbic acid. As mentioned above, we observed the inhomogeneous coating of the silver onto the Au cubes without the presence of the ascorbic acid. In addition, we merely observed ramified structures. With the addition of ascorbic acid, we observe the formation of Au@Ag core-shell nanostructures *via ex-situ* characterization techniques, such as UV-Vis spectroscopy, EDX, 3D STEM Tomography and TEM diffraction.

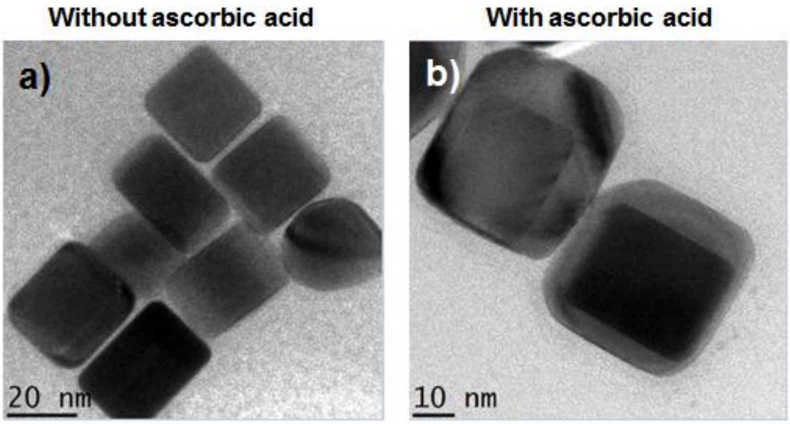

Figure 7.4 TEM images of gold nanocubes after reacting with (a) silver nitrate solution without ascorbic acid (b) silver nitrate solution with ascorbic acid.

7.2.3.1. UV-Vis Spectroscopy

Figure 7.5 shows the low magnification TEM images of the ex-situ prepared gold nanocubes before (a) and after(c) reacting with the silver nitrate aqueous solution. The UV-Vis spectra in Figure 7.5 (b) indicates that this reduction reaction happened within one minute (the spectra was collected right after the addition of silver nitrate solution), the color of the solution changed instantly from purple to red color.

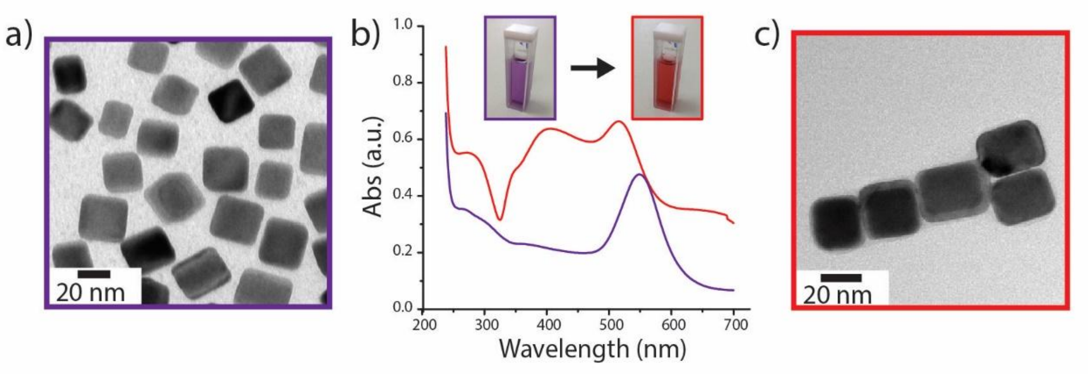

Figure 7.5 Low magnification TEM images of ex-situ prepared gold nanocuboids (a) before and (c) after reacting with silver nitrate aqueous solution (b) UV-vis spectra of the solution before (purple) and after (red) adding the silver nitrate aqueous solution. The insets show the corresponding photographs of the solutions.

7.2.3.2. TEM Imaging Characterization

In addition, we found out that the silver shell transformed from a cubic shape into a truncated cubic/octahedral shape, the assymmetric growth of Ag on Au becomes more and more symmetric (Figure 7.6 a-c) upon increasing the concentration of the reducing agent. The *ex-situ* prepared Au@Ag core-shell nanostructures show that the growth of the Ag layer results in the development of {100} facets changing to {110} facets as the reduction proceeds. It is also worth noting that the thickness of the shells (see Figure 7.2 for histograms) are similar for both *ex-situ* and *in-situ* observation. These explain our *in-situ* results where the Ag layer grows and develops into {110} facets when an additional reduction source – the electron beam – is present.

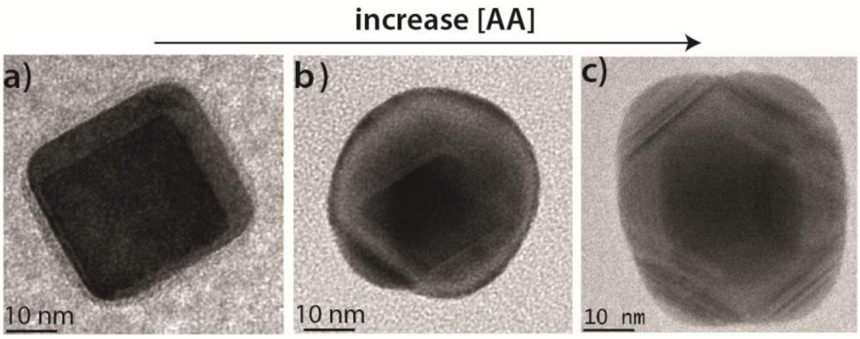

Figure 7.6 TEM images of gold nanocubes after reacting with fixed amount of 20 µl of 10 mM silver nitrate solution and 10 mM of ascorbic acid of (a) 10 µl (b) 50 µl (c) 200 µl.

7.2.3.3. TEM Diffraction

Figure 7.7 (a) and (c) show the TEM images of the individual nanostructure and the corresponding electron diffraction patterns before and after reacting with the silver solution. The electron patterns suggest that the gold nanocubes are single crystals with {100} facets before reacting with the silver nitrate solution. The Au@Ag core-shell nanostructure show a diffraction patterns with {110}and {111} facets. The nanostructure in Figure (f) shows the cubohedron enclosed by a mix of {111} and {110}. It must be noted that the lattice parameters of gold and silver are nearly identical, so we are not able to distiguish between gold and silver diffraction spots directly, but STEM-EDX (Section 7.2.3.4) can make this distinction.

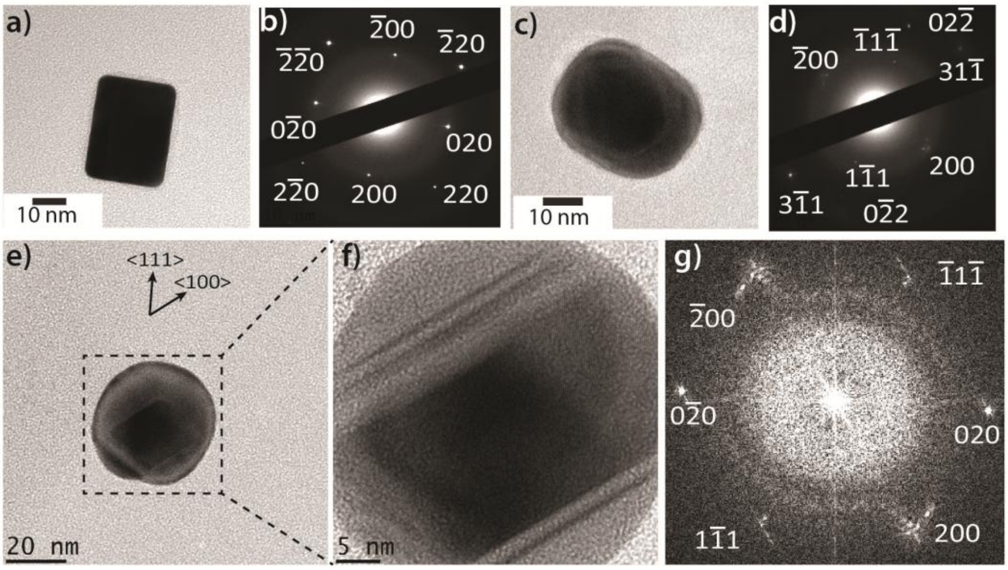

Figure 7.7 TEM images of a gold nanocube (a) before and (c) after reacting with silver nitrate aqueous solution in the presence of AA and their corresponding diffraction patterns (b) and (d) respectively. (e) and (f) showing the high resolution TEM images of a Au@Ag core-shell nanostructure and its corresponding FFT (g).

7.2.3.4. Energy-Dispersive X-Ray Spectroscopy (EDX)

Figure 7.8 shows (a and c) STEM images and the coressponding EDX line scans (b and d) from a single Au@Ag core-shell nanostructure. The line scans suggest that the shell is consisted of silver while the core remains as gold. Moreover, the shell thickess is not uniformly covered over the nanocube. The intensity in the HAADF-STEM images scales with the atomic number of the elements present in the sample: Ag (47) and Au (79).[24]

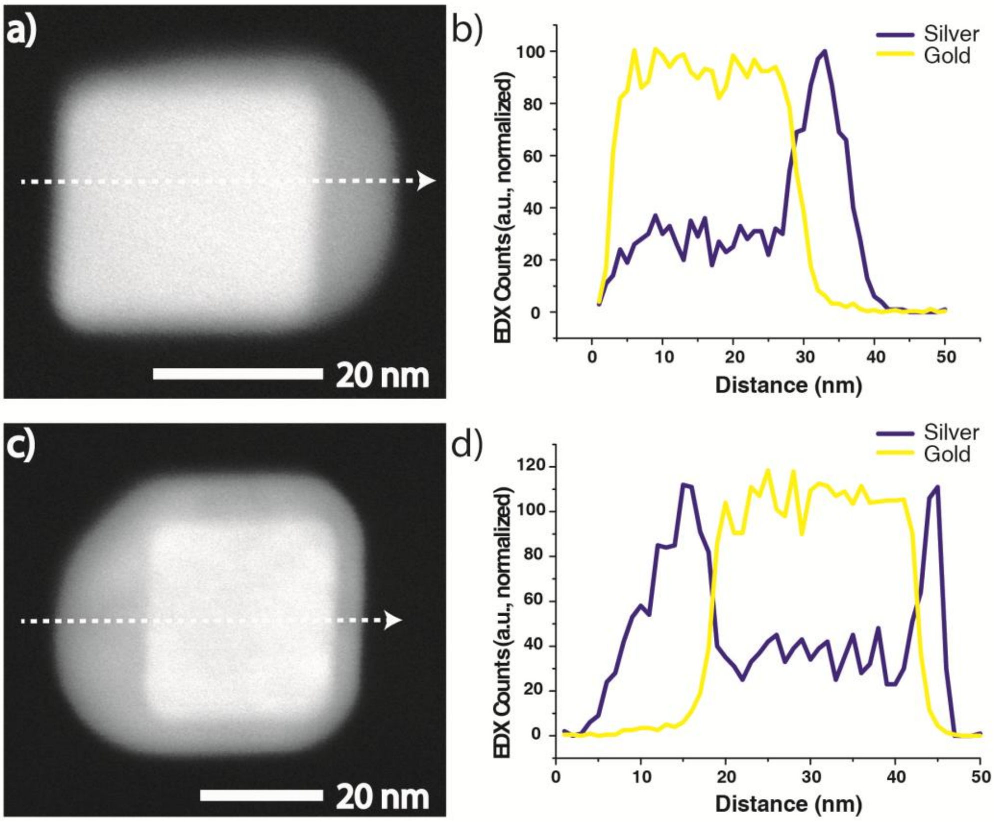

Figure 7.8 (a) and (c) HAADF-STEM images of two Ag/Au core-shell nanostructures while (b) and (d) EDX line-scan profiles of the same structure respectively. The yellow line plots the gold counts; the blue line the silver counts from the location of the white arrow in panel (a) and (c) respectively.

7.2.3.5. 3D HAADF-STEM Tomography

We conducted HAADF-STEM tomography which is able to provide a 3-dimensional view to further characterize the Au@Ag core-shell nanostructures.[25] We tilted the substrate with the etched nanocube from -70° to 75° with respect to the horizontal axis of the nanocube. We brought the series of images to one rotation axis by aligning all images accurately and reconstructed a 3D volume over 57 STEM images eventually. The reconstructed 3D volume showed clearly a truncated cube/octahedron silver shell coated on the gold nanocube. In addition, the HADDF-STEM images in Figure 7.9 (c) reveal that the core of the structure appears to be brighter (higher intensities) which were indicated by red dotted lines. The intensity in the HAADF-STEM images scales with the atomic number of the elements present in the sample: Ag (47) and Au (79).[24] This is consistent with our EDX observation in Figure 7.8 where the silver layer was deposited onto the gold nanocube.

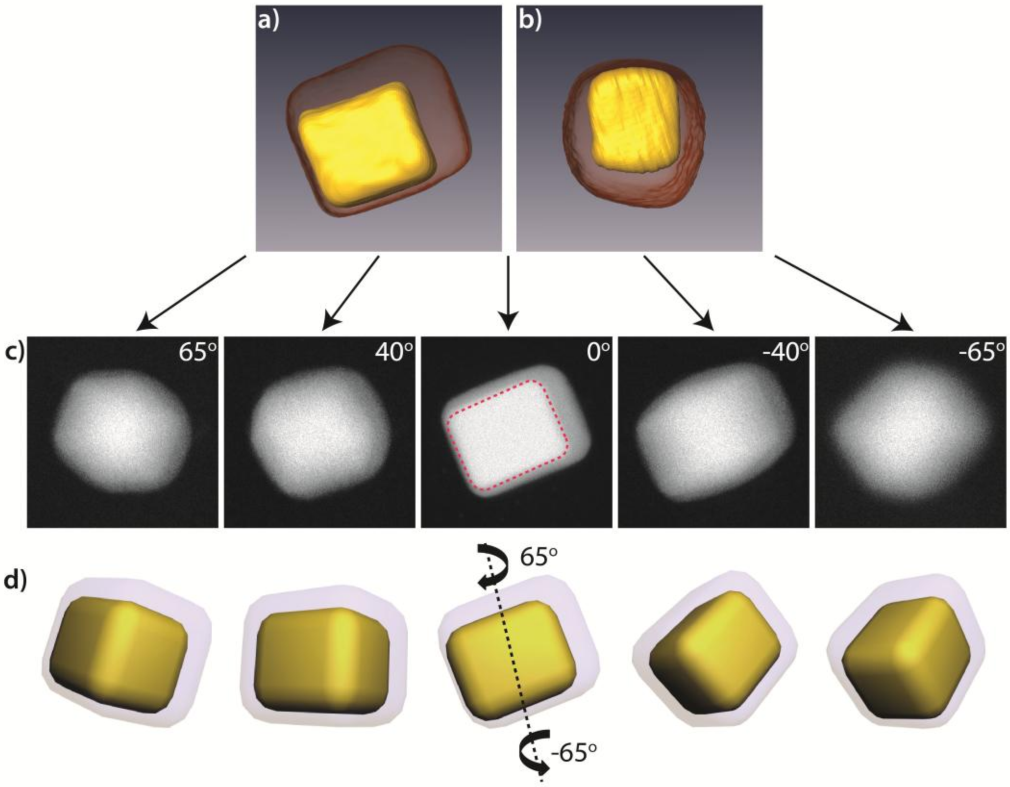

Figure 7.9 Surface-rendered visualization of the Au@Ag core-shell nanostructure morphology reconstructed by HAADF-STEM tomography, viewed along the (a) [100] and (b) [001] axes. (c) HAADF-STEM tomography images of an individual nanostructure where the substrate was tilted from -65° to 65°. (d) Schematic illustration showing the top view of the above structure.

7.2.4. *In-Situ* Observation: Mechanistic Pathways for Core-Shell Nanoparticles Formation

Furthermore, our results show that two mechanistic pathways in which the overgrowth occurs. (1) Pre-nucleated silver nanoparticles approach and absorb onto the gold nanocubes, followed by coalescence to form a layer of silver on the gold nanocube. (2) The gold nanocubes undergo deposition of silver through monomer attachment. Figure 7.10 (a) and (c) show two time series of TEM images from single Au nanocube reacting with the silver nitrate aqueous solution inside a liquid flow cell *via* the two pathways resulting in the Au@Ag core-shell nanoparticle formation. Figures 7.10 (b) and (d) illustrate these two processes schematically.

For the first pathway, we observed the formation of small particles of diameter ~3 nm (encircled in red) at t = 4.7 s. We believe these small silver particles are formed when the silver nitrate solution is brought in contact with the (1) L-ascorbic acid (AA) solution inside the liquid cell or (2) through radiolysis (i.e., reduction of the Ag^+ ions by solvated electrons). The image recorded at t = 17.8 s and the subsequent images show that the small silver nanoparticles attach onto the surface of the gold nanocube and then merge into a continuous layer. In addition, the shell thickness at the edge (E) and corner (D) in Figure 7.10 (e) shows a non-linear growth as a result of the small particles dissolution. The measurement of thickness is done over three real-time movies of three different particles. For the second pathway, there is no small particles formation throughout the whole growth process. We observed a conformal growth (homogeneous coating) of the silver shell as a function of time. Both pathways will eventually lead to the same final product: the Au@Ag core-shell nanostructure.

Similarly limited growth also has been reported in previous studies.[9-10, 12-13, 16] Electron beam depletion of the precursor solution can be one reason causing the termination of further shell growth in the *in-situ* experiments, but we also observe Ag nanoparticles formation outside the field of view due to electron beam reduction. Furthermore, it does not explain why the growth seems to be size-controlled in the *ex-situ* experiments (Figure 7.6 a-c).

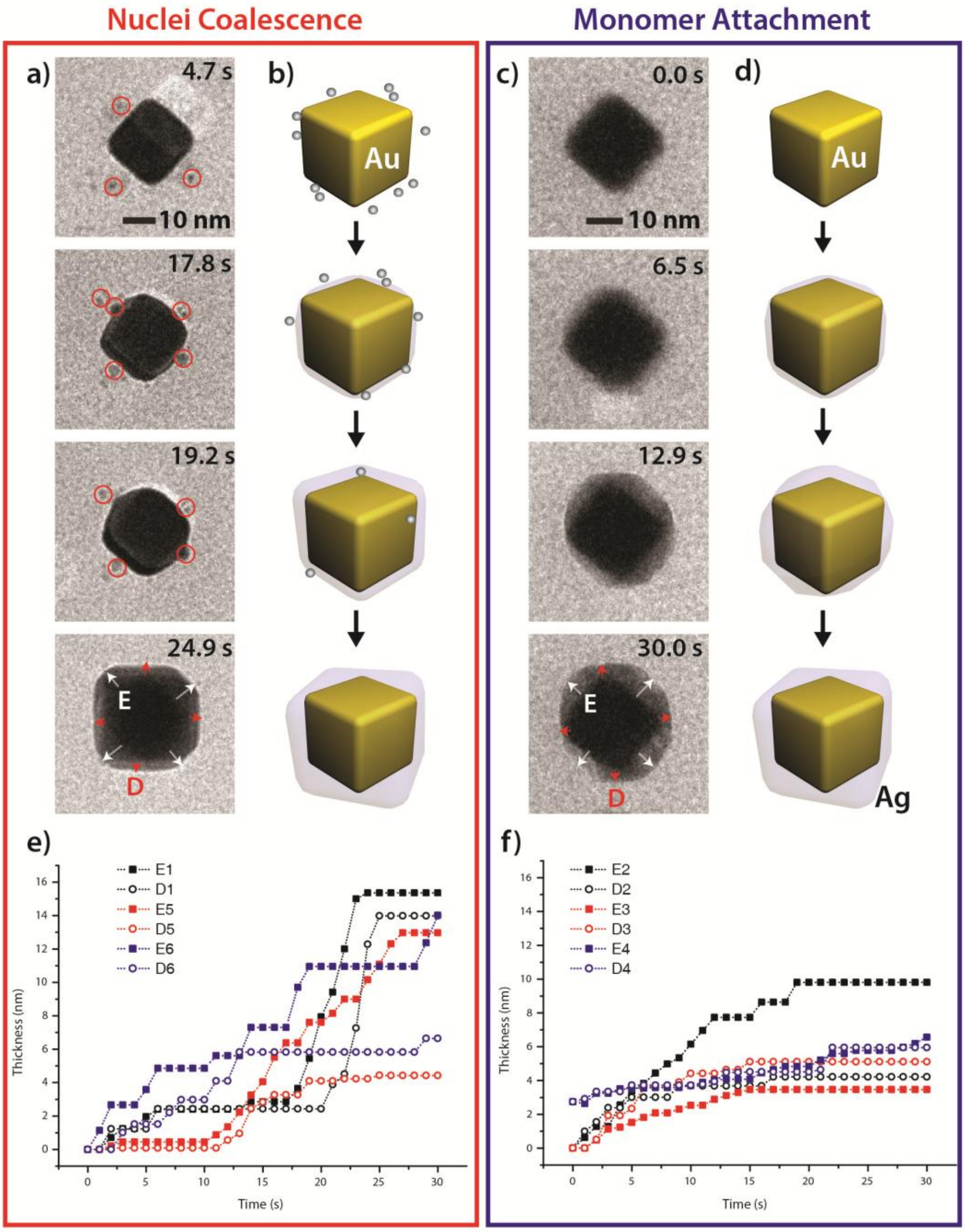

Figure 7.10 Time-lapse TEM images showing a gold nanocube interacting with the silver nitrate aqueous solution inside a liquid flow cell *via* (a) Ostwald ripening process and (c) monomer attachment. The schematic of the reaction between gold nanocubes and silver nitrate aqueous solution for both pathways: (b) and (d). The measured thickness of edge (E, solid squares) and corner (D, hollow circles) of the Au@Ag core-shell particle as a function of time for both pathways: (e) and (f).

In addition, we also observed the shapes of our final product majority are cuboctahedrons (Figure 7.10 a and c) and enlarged cubes with truncated corners (Figure 7.2 a-e) occasionally. This suggests that thermodynamic control is responsible for the exquisite tunability of the overgrowth layers in these nanostructures.[26] In this route, surface diffusion is faster than the atom deposition where the adatoms tend to migrate from the corners to the edges and side faces. If surface diffusion is much faster than the deposition rate (*i.e.*, the ratio is much less than 1), growth is promoted along <100> and <110> directions, leading to the formation of cubohedral shells (Figure 7.11 a). In the other case where the ratio between atom deposition and surface diffusion is less than but close to 1, conformal growth is expected (Figure 7.11 b). We propose that our experiment is an example of the latter for three reasons. (1) As described earlier, the capping agents would have been washed out prior to the silver introduction. (2) Our experiments were conducted at room temperature (in contrast to the synthesis temperatures of 60 °C reported by Xia *et al.*[18] and Tsuji *et al.*[12], making it unlikely that surface diffusion will be fast). (3) The *in-situ* experiments show that the growth starts off in a conformal manner.

Therefore, the development of {110} facets in both *in-situ* and *ex-situ* results (Figure 7.9) leads to the final cuboctahedron shape of the nanostructures and would indicate the growth mechanism is thermodynamically controlled with the absence or low coverage of capping agents. Furthermore, the *in situ* results also indicate that atomic deposition is not the only mechanisms by which the Ag layer grows. The coalescence and integration of pre-existing nuclei into a growing shell implies that the growth can also take place via attachment-based growth.[27-28] Attachment-based refers to a non-classical growth mechanism where crystals grow *via* attachment, re-orientation and coalescence of smaller nanocrystals. The main driving force here is the reduction in surface energy.

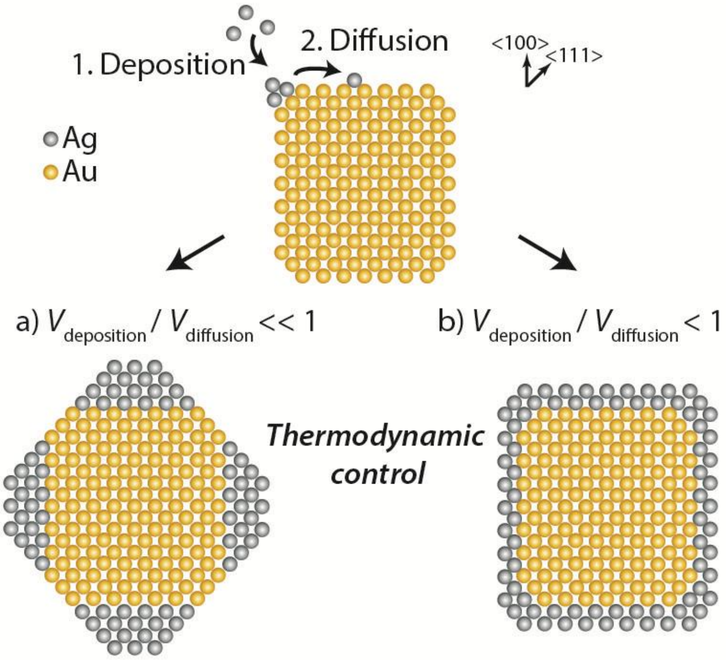

Figure 7.11 Schematic illustrations showing the shape evolution of a cubic seed under thermodynamic control for two kinetic conditions: (a) $V_{\text{deposition}}/ V_{\text{diffusion}} << 1$ (b) $V_{\text{deposition}}/ V_{\text{diffusion}} < 1$. This model is adapted from Xia *et al*.[26]

7.3. Conclusions

We studied the overgrowth process of silver on gold nanocubes with addition of chemical reducing agent ascorbic acid. First, we show that the initial overgrowth is chemically-mediated by ascorbic acid and not CTAB, which contradicts conventional understanding. Second, we observe two different mechanistic pathways. (1) The silver nanoparticles approach and absorb onto the gold nanocubes, while simultaneously a layer of silver was deposited onto the gold nanocube as a result of coalescence. (2) The gold nanocubes undergo epitaxial deposition of silver through monomer attachment. Both mechanistic pathways lead to the same final products. This all round growth could be due to poor coverage of the capping agents. Absence of overgrowth when only the electron beam was used to reduce the Ag precursor and comparison with *ex situ* synthesized nanostructures suggest that the observed reaction may be insensitive to the electron beam. This study shows that not only can we study growth mechanisms with *in-situ* TEM, the technique can also be used to elucidate the role of the chemical additives, which would be useful for material engineering in nanofabrication.

7.4. Experimental Section

7.4.1. General Procedures. For the gold nanocuboids, the chemicals: gold (ɪɪɪ) chloride trihydrate, sodium borohydride, cetyltrimethylammonium bromide, copper sulfate, L-ascorbic acid were all purchased from Sigma-Aldrich and used without further purification. The glass vials used for synthesis were obtained from Fisher Scientific. Solvents for nanoparticles functionalization were freshly distilled prior to use. All stirrer bars were soaked in aqua-regia (mixture of 1:3 volume ratio of nitric acid:hydrochloric acid) for at least 1 hour, washed with deionized water (18.2 Ωcm) and dried in an oven before use. Nanoparticles were washed in Rotina (model 380R) and Profuge (model 14D) centrifuges.

7.4.2. Synthesis of Gold Nanocuboids: Refer to Chapter 5 Section 5.2.1. The experimental details are described in Section 5.4.

7.4.3. Experimental Techniques: We transferred 1.0 ml of the cuboidal gold nanoparticles solution from the glass vial into a 1.5 ml-centrifuge tube. Centrifugation and redispersion in water was performed twice at 10000 rpm for 10 minutes in order to minimise the concentration of CTAB prior to loading to the liquids cells. Note that too many times of washing (centrifuge and redisperse) will cause the deformation of Au cuboids. 10 µl of 10 mM ascorbic acid aqueous solution was added into the as-washed Au cuboids solution.

Approximately 500 nl of the resulting solution was loaded into a liquid TEM cell, which comprised of two ultrathin (~30 nm) electron translucent SiN_x membranes separated by 200 nm. Prior to solution loading, these liquid cells were oxygen plasma treated to make their SiN_x membrane surfaces hydrophilic. We used a Hummingbird Scientific Liquid Flow holder and a JEOL 2010FEG TEM operated at 200 kV for in situ imaging with low electron doses ranging from 50 to 150 $e/(Å^2 \cdot s)$, acquiring images at a rate of 10 frames per second with an ORIUS SC200 CCD camera (Gatan, Inc.). The reaction was followed in real-time by observing cuboids found in 30 micron by 200 micron window of the TEM liquid cell. The high-angle annular dark-field scanning TEM (HAADF-STEM) imaging and chemical analysis were performed with an FEI Titan TEM equipped with a Schottky electron source operated at 200 kV. We obtained the STEM images by using an electron probe with an approximate diameter of 0.3 nm. EDX was performed with a probe ca. 0.5 nm in diameter with 150 ms acquisition time for each spectrum. The Inspect3D software from FEI was used for 3D tomography reconstruction. We recorded the UV/Vis spectra on UV/VIS/NIR spectroscopy (PerkinElmer Lambda 750). We measured the light transmission through a cuvette of 1 cm light-path.

7.5. References

1. Oldenburg, S. J.; Averitt, R. D.; Westcott, S. L.; Halas, N. J., Nanoengineering of optical resonances. *Chemical Physics Letters* **1998,** *288* (2–4), 243-247.
2. Laurent, S.; Forge, D.; Port, M.; Roch, A.; Robic, C.; Vander Elst, L.; Muller, R. N., Magnetic Iron Oxide Nanoparticles: Synthesis, Stabilization, Vectorization, Physicochemical Characterizations, and Biological Applications. *Chemical Reviews* **2008,** *108* (6), 2064-2110.
3. Caruso, F., Nanoengineering of Particle Surfaces. *Advanced Materials* **2001,** *13* (1), 11-22.
4. Daniel, M.-C.; Astruc, D., Gold Nanoparticles: Assembly, Supramolecular Chemistry, Quantum-Size-Related Properties, and Applications toward Biology, Catalysis, and Nanotechnology. *Chemical Reviews* **2004,** *104* (1), 293-346.
5. Kortan, A. R.; Hull, R.; Opila, R. L.; Bawendi, M. G.; Steigerwald, M. L.; Carroll, P. J.; Brus, L. E., Nucleation and growth of cadmium selendie on zinc sulfide quantum crystallite seeds, and vice versa, in inverse micelle media. *Journal of the American Chemical Society* **1990,** *112* (4), 1327-1332.
6. Mews, A.; Eychmueller, A.; Giersig, M.; Schooss, D.; Weller, H., Preparation, characterization, and photophysics of the quantum dot quantum

well system cadmium sulfide/mercury sulfide/cadmium sulfide. *The Journal of Physical Chemistry* **1994,** *98* (3), 934-941.

7. Ma, G. H.; He, J.; Rajiv, K.; Tang, S. H.; Yang, Y.; Nogami, M., Observation of resonant energy transfer in Au:CdS nanocomposite. *Applied Physics Letters* **2004,** *84* (23), 4684-4686.

8. Ghosh Chaudhuri, R.; Paria, S., Core/Shell Nanoparticles: Classes, Properties, Synthesis Mechanisms, Characterization, and Applications. *Chemical Reviews* **2012,** *112* (4), 2373-2433.

9. Ma, Y.; Li, W.; Cho, E. C.; Li, Z.; Yu, T.; Zeng, J.; Xie, Z.; Xia, Y., Au@Ag Core−Shell Nanocubes with Finely Tuned and Well-Controlled Sizes, Shell Thicknesses, and Optical Properties. *ACS Nano* **2010,** *4* (11), 6725-6734.

10. Gong, J.; Zhou, F.; Li, Z.; Tang, Z., Synthesis of Au@Ag Core–Shell Nanocubes Containing Varying Shaped Cores and Their Localized Surface Plasmon Resonances. *Langmuir* **2012,** *28* (24), 8959-8964.

11. Fu, W.; Yang, H.; Chang, L.; Li, M.; Bala, H.; Yu, Q.; Zou, G., Preparation and characteristics of core–shell structure nickel/silica nanoparticles. *Colloids and Surfaces A: Physicochemical and Engineering Aspects* **2005,** *262* (1–3), 71-75.

12. Tsuji, M.; Matsuo, R.; Jiang, P.; Miyamae, N.; Ueyama, D.; Nishio, M.; Hikino, S.; Kumagae, H.; Kamarudin, K. S. N.; Tang, X.-L., Shape-Dependent Evolution of Au@Ag Core−Shell Nanocrystals by PVP-Assisted N,N-Dimethylformamide Reduction. *Crystal Growth & Design* **2008,** *8* (7), 2528-2536.

13. Lim, B.; Kobayashi, H.; Yu, T.; Wang, J.; Kim, M. J.; Li, Z.-Y.; Rycenga, M.; Xia, Y., Synthesis of Pd−Au Bimetallic Nanocrystals via Controlled Overgrowth. *Journal of the American Chemical Society* **2010,** *132* (8), 2506-2507.

14. Cho, E. C.; Camargo, P. H. C.; Xia, Y., Synthesis and Characterization of Noble-Metal Nanostructures Containing Gold Nanorods in the Center. *Advanced Materials* **2010,** *22* (6), 744-748.

15. Jungjohann, K. L.; Bliznakov, S.; Sutter, P. W.; Stach, E. A.; Sutter, E. A., In Situ Liquid Cell Electron Microscopy of the Solution Growth of Au–Pd Core–Shell Nanostructures. *Nano Letters* **2013,** *13* (6), 2964-2970.

16. Wu, J.; Gao, W.; Wen, J.; Miller, D. J.; Lu, P.; Zuo, J.-M.; Yang, H., Growth of Au on Pt Icosahedral Nanoparticles Revealed by Low-Dose In Situ TEM. *Nano Letters* **2015,** *15* (4), 2711-2715.

17. Fan, F.-R.; Liu, D.-Y.; Wu, Y.-F.; Duan, S.; Xie, Z.-X.; Jiang, Z.-Y.; Tian, Z.-Q., Epitaxial Growth of Heterogeneous Metal Nanocrystals: From Gold Nano-octahedra to Palladium and Silver Nanocubes. *Journal of the American Chemical Society* **2008,** *130* (22), 6949-6951.

18. Xia, X.; Xie, S.; Liu, M.; Peng, H.-C.; Lu, N.; Wang, J.; Kim, M. J.; Xia, Y., On the role of surface diffusion in determining the shape or morphology of noble-metal nanocrystals. *Proceedings of the National Academy of Sciences* **2013,** *110* (17), 6669-6673.

19. Mirsaidov, U. M.; Zheng, H.; Bhattacharya, D.; Casana, Y.; Matsudaira, P., Direct observation of stick-slip movements of water nanodroplets induced by an electron beam. *Proceedings of the National Academy of Sciences* **2012,** *109* (19), 7187-7190.

20. Zheng, H.; Smith, R. K.; Jun, Y.-w.; Kisielowski, C.; Dahmen, U.; Alivisatos, A. P., Observation of Single Colloidal Platinum Nanocrystal Growth Trajectories. *Science* **2009,** *324* (5932), 1309-1312.

21. Liao, H.-G.; Niu, K.; Zheng, H., Observation of growth of metal nanoparticles. *Chemical Communications* **2013,** *49* (100), 11720-11727.

22. Woehl, T. J.; Evans, J. E.; Arslan, I.; Ristenpart, W. D.; Browning, N. D., Direct in Situ Determination of the Mechanisms Controlling Nanoparticle Nucleation and Growth. *ACS Nano* **2012,** *6* (10), 8599-8610.

23. Noh, K. W.; Liu, Y.; Sun, L.; Dillon, S. J., Challenges associated with in-situ TEM in environmental systems: The case of silver in aqueous solutions. *Ultramicroscopy* **2012,** *116* (0), 34-38.

24. Pennycook, S. J.; Jesson, D. E., High-resolution incoherent imaging of crystals. *Physical Review Letters* **1990,** *64* (8), 938-941.

25. Goris, B.; Polavarapu, L.; Bals, S.; Van Tendeloo, G.; Liz-Marzán, L. M., Monitoring Galvanic Replacement Through Three-Dimensional Morphological and Chemical Mapping. *Nano Letters* **2014,** *14* (6), 3220-3226.

26. Xia, Y.; Xia, X.; Peng, H.-C., Shape-Controlled Synthesis of Colloidal Metal Nanocrystals: Thermodynamic versus Kinetic Products. *Journal of the American Chemical Society* **2015,** *137* (25), 7947-7966.

27. Penn, R. L.; Soltis, J. A., Characterizing crystal growth by oriented aggregation. *CrystEngComm* **2014,** *16* (8), 1409-1418.

28. Ataee-Esfahani, H.; Skrabalak, S. E., Attachment-based growth: building architecturally defined metal nanocolloids particle by particle. *RSC Advances* **2015,** *5* (59), 47718-47727.

Chapter 8

General Conclusions & Outlook

This thesis describes the controlled immobilization of molecules between two cuboidal metal nanoparticles by self-assembly to control quantum plasmon resonances. Mixed self-assembled monolayers (SAMs) of thiolates and dithiolates molecules were used to control the gap sizes between the metal nanoparticles down to sub-nanometer scales. We studied quantum mechanical tunneling across the metal-molecules-metal junctions by a combination of complimentary characterization techniques, e.g., electron microscopy, electron spectroscopy, and theoretical support was provided *via* quantum-corrected finite-element-model (FEM) simulations. It was demonstrated that the SAMs not only could control the width between two plasmonic resonators but also could act as frequency controllers in the terahertz regime, providing a new control parameter in the fabrication of electrical circuits facilitated by quantum plasmon tunnelling.

Chapter 2 provided a literature overview to show that engineering sub-nanometer gaps in metal nanostructures for plasmonics applications are key to study the quantum mechanical effects at nanoscales. The self-assembly process to fabricate the high aspect ratio gaps between metal nanoparticles was studied in some depth in Chapter 3, by comparing different mixed SAMs of thiolates and dithiolates (aliphatic SAMs: EDT, HDT, ODT; aromatic SAMs: BDT, BPDT, OPV, and NDT) using various characterization techniques (TEM, 3D STEM Tomography, UV-Vis, XPS, and UPS). 3D STEM Tomography showed clearly that the gaps are free of metal filaments. TEM gap size characterization indicated that the experimentally measured gap sizes are in good correlation with the molecular length predicted by the CPK model. The aromatic SAMs showed more linear assemblies in UV-Vis than the aliphatic SAMs due to the stronger pi-pi interaction between rigid benzene rings than the intercalating alkyl chains. XPS results further demonstrated the presence of the SAMs in connecting the metal nanoparticles while UPS results revealed that the SAMs could provide control over the energy barrier heights of the studied system.

Chapter 4 demonstrated the realization of quantum plasmon tunnelling by using metal-molecules-metal junctions as a platform and electron microscopy for characterization. By combining atomic-resolution imaging, single-particle spectroscopy and monolayer molecular control, we demonstrated the direct observation of and control over the quantum plasmon resonances at the length scales in the range 0.4 to 1.3 nm across the metal-molecules-metal junctions. Besides control over the distance, the SAMs also control the tunnel barrier energy height. The measured resonance frequency of the tunnelling charge transfer plasmon varied from 145 ± 10 THz for monolayers of BDT molecules to 244 ± 3 THz for monolayers of EDT molecules. Through-bond tunnelling is the dominant mechanism of charge transport which is only weakly dependent on the gap size as we observed, in contrast to the alternative through-space model, which would have a very strong gap size dependence. The tunnelling was observed for gap sizes (tunnel distances) up to 1.3 nm, for Ag-BDT//BDT-Ag junctions, which potentially indicated that even longer molecules of perhaps 4-5 nm may also be used for plasmon-asssisted electron tunneling.

Physical-organic studies similar to those discussed in Chapter 4 were also performed on closely-spaced gold nanocuboids. However, in this case, the dimer gaps suffered from filament formation. This triggered us to study the degradation mechanism of passivated gold and silver nanoparticles under high energy electron beam. In Chapter 5, a stability study was presented of cuboidal metal nanoparticles under electron beam irradiation, and strategies were discussed for avoiding radiation damage. The thiolated SAMs coated gold nanocuboids suffered from surface diffusion-driven filament formation while the electron beam-induced heating at the metal-ligand interface is dominant for thiolated SAMs-coated silver nanocubes. Replacing the thiolated SAMs with PVP provides stabilization for both gold and silver nanocuboids. PVP could act as a diffusion barrier and is more resistant to damage induced by the electron beam.

The synthesis of high-quality cuboidal metal nanoparticles we used for quantum plasmonics requires deeper understanding of the reaction chemistry and kinetics at the nanoscale. Chapters 6 and 7 described the real-time visualization of chemical reactions of cuboidal metal nanoparticles in solution by using liquid-cell electron microscopy techniques. In Chapter 6, a detailed mechanistic study of galvanic replacement reactions between silver nanocuboids and chloroauric acid was provided. The detailed analysis of silver removal rate and gold deposition indicated that the morphology and composition of the final product are dependent greatly on the subtle changes of the stoichiometric ratio between gold and silver.

Chapter 7 demonstrated the overgrowth process of silver on gold nanocuboids in silver nitrate solution in the presence of the reducing agent ascorbic acid using *in-situ* liquid-cell electron microscopy. The detailed analysis of silver deposition revealed that there are two mechanistic pathways: nuclei coalescence and monomer attachment, both result in the same Au@Ag core-shell nanostructures formation. A comparison of *in-situ* and *ex-situ* synthesized nanostructures tells us that this reaction may be insensitive to the electron beam and is chemically-mediated by the reducing agent. This study showed that the *in-situ* TEM technique not only can be used to study growth mechanisms, but also to elucidate the role of the chemical additives.

The result presented in this thesis show that precise control of the structural and opto-electronic properties between two closely-spaced nanoparticles is essential to switch on the quantum plasmon tunnelling. It was shown that the frequencies of the quantum mechanical plasmon modes can be tuned by simply changing the layers of molecules linking two nanoparticles. This study provided a key advance towards the creation of technologically accessible tunnelling length scales of up to 1.3 nm, which is 3-4 times larger than what has been reported before. On the other hand, *in-situ* liquid cell electron microscopy has evolved as a tool to elucidate the reaction mechanism and kinetics during chemical reactions such as galvanic replacement reactions and core-shell nanoparticles formation at the nanoscale. This study provided a quantitative picture of the growth process that is useful for engineering the composition and morphology of metal nanostructures that could potentially open up more opportunities for application in plasmonics.

The ability of molecules to bring two nanoparticles closely together in a controlled way is going to be a primary feature for combining molecular electronics and plasmonics. From the discipline of molecular electronics, it is known that the transport characteristics are dependent on the intrinsic properties of the molecules. This inspired us to study different molecules inside the junctions between two nanoparticles to explore whether more concepts from the field of molecular electronics can be incorporated into the field of plasmonics. It is worth noting that before this demonstration, it was unknown that molecular electronics is possible at all at optical frequencies. The link between the fields of optics and molecular electronics demonstrated in this work may provide potential for molecular control over quantum plasmonic systems through even longer gap sizes (4-5 nm) that are currently accessible by top-down fabrication techniques. Examples of longer molecules with higher conductance values are: biphenyl dithiols derivatives, naphthalene dithiol derivatives, etc. The reconciliation of molecular electronics with plasmonics at engineerable scales may then open up possible new design routes for plasmonic-electronics that combine the small scale of nano-electronics with the fast operating speed of optics. Following up the new ideas that are developed from these results, we hope ultimately to resolve the challenges that are presented in the course of this work, such as the integration of these devices into real opto-electronic circuits.